CAPITAL UNIVERSITY OF SCIENCE AND TECHNOLOGY, ISLAMABAD

Superconducting Cavity Field Control in Radio Frequency Particle Accelerator

by

Waqas Ahmed Toor

A dissertation submitted in partial fulfillment for the
degree of Doctor of Philosophy

in the

Faculty of Engineering

Department of Electrical & Computer Engineering

2025

Superconducting Cavity Field Control in Radio Frequency Particle Accelerator

By

Waqas Ahmed Toor

(DEE191004)

Dr. Kamran Iqbal, Professor

University of Arkansas at Little Rock, Arkansas, USA

(Foreign Evaluator 1)

Dr. Muhammad Tariq Iqbal, Professor

Memorial University of Newfoundland, Canada

(Foreign Evaluator 2)

Dr. Muhammad Ashraf

(Research Supervisor)

Dr. Noor Muhammad Khan

(Head, Department of Electrical & Computer Engineering)

Dr. Imtiaz Ahmad Taj

(Dean, Faculty of Engineering)

DEPARTMENT OF ELECTRICAL & COMPUTER ENGINEERING

CAPITAL UNIVERSITY OF SCIENCE AND TECHNOLOGY

ISLAMABAD

2025

This dissertation is dedicated to my father Iftikhar Ahmed Toor,my mother, my wife, my brothers and sisters and my kids.

CERTIFICATE OF APPROVAL

This is to certify that the research work presented in the dissertation, entitled "**Superconducting Cavity Field Control in Radio Frequency Particle Accelerator**" was conducted under the supervision of **Dr. Muhammad Ashraf**. No part of this dissertation has been submitted anywhere else for any other degree. This dissertation is submitted to the **Department of Electrical & Computer Engineering, Capital University of Science and Technology** in partial fulfillment of the requirements for the degree of Doctor in Philosophy in the field of **Electrical Engineering.** The open defence of the dissertation was conducted on **January 08, 2025**.

Student Name : Waqas Ahmed Toor (DEE191004)

The Examination Committee unanimously agrees to award PhD degree in the mentioned field.

Examination Committee :

(a)	External Examiner 1:	Dr. Nisar Ahmed Professor GIKI, Topi, Swabi
(b)	External Examiner 2:	Dr. Haroon ur Rashid Professor PIEAS, Islamabad
(c)	Internal Examiner :	Dr. Noor Muhammad Khan Professor CUST, Islamabad

Supervisor Name : Dr. Muhammad Ashraf
Professor
CUST, Islamabad

Name of HoD : Dr. Noor Muhammad Khan
Professor
CUST, Islamabad

Name of Dean : Dr. Imtiaz Ahmad Taj
Professor
CUST, Islamabad

AUTHOR'S DECLARATION

I, **Waqas Ahmed Toor** (Registration No. **DEE191004**), hereby state that my dissertation titled, "**Superconducting Cavity Field Control in Radio Frequency Particle Accelerator**" is my own work and has not been submitted previously by me for taking any degree from Capital University of Science and Technology, Islamabad or anywhere else in the country/ world.

At any time, if my statement is found to be incorrect even after my graduation, the University has the right to withdraw my PhD Degree.

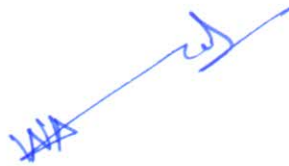**(Waqas Ahmed Toor)**

Dated: 08 January, 2025

Registration No : DEE191004

PLAGIARISM UNDERTAKING

I solemnly declare that research work presented in the dissertation titled **"Superconducting Cavity Field Control in Radio Frequency Particle Accelerator"** is solely my research work with no significant contribution from any other person. Small contribution/ help wherever taken has been duly acknowledged and that complete dissertation has been written by me.

I understand the zero-tolerance policy of the HEC and Capital University of Science and Technology towards plagiarism. Therefore, I as an author of the above titled dissertation declare that no portion of my dissertation has been plagiarized and any material used as reference is properly referred/ cited.

I undertake that if I am found guilty of any formal plagiarism in the above titled dissertation even after award of PhD Degree, the University reserves the right to withdraw/ revoke my PhD degree and that HEC and the University have the right to publish my name on the HEC/ University Website on which names of students are placed who submitted plagiarized dissertation.

(Waqas Ahmed Toor)

Dated: 08 January, 2025   Registration No : DEE191004

List of Publications

It is certified that following publication(s) have been made out of the research work that has been carried out for this dissertation:-

1. **W.A.Toor**, M.Ashraf, "Performance Analysis of Learning-based Disturbance Observer for Pulsed Superconducting Cavity Field Control," *Electronics*, vol. 12, Issue 7, pp. 1556 , 2023.

(Waqas Ahmed Toor)

Registration No: DEE191004

Acknowledgement

In the name of **Allah**, The Most Beneficent, The Most Merciful. First and foremost, I would like to express gratitude to Allah SWT, the Almighty God, for the blessing, kindness, and inspiration in lending me to pursue my doctoral studies.

I am indebted to my teachers whose teachings have brought me to this stage. Certainly, it is a pleasant obligation to thank **Dr. Muhammad Ashraf**, my Research supervisor , for his valuable guidance, strong encouragement, and kind support towards my study and research. I have learned not only from his insight, deep technical knowledge, and practical experience but many things from him.

I would like to thank my wonderful teacher and Head, Department of Electrical and Computer Engineering, **Dr. Noor Muhammad Khan**, for his able guidance, teaching and encouragement to carry out this research.

I would like to thank the Vice Chancellor **Dr. Muhammad Mansoor Ahmed** Dean, Faculty of Engineering **Dr. Imtiaz Ahmad Taj**, **Dr. Fazal-ur-Rehman** and **Graduate Student Office (GSO)** for their able guidance. I would like to thank the respected examiners for their valuable time and suggestions for improvement of this dissertation.

I also acknowledge the intimate support of my parents and brother **Sajjad Toor**, throughout my educational career. Their prayers and moral and financial support always motivated me toward my goal. I also appreciate my spouse and children for their cooperation, love, and support and for providing a stress-free atmosphere during my doctorate tenure. I highly appreciate and acknowledge the support of my wife **Dr. Raafia Irfan**, in carrying out this research and writing this dissertation. I would like to thank all my family members and friends for their prayers.

I want to thank **Engr. Muhammad Zeeshan Fiaz**, for development of AFC for magnetron to power side coupled 6 MeV cavity and sharing his experience in operation and simulation of the accelerator cavity. I would also like to thank **Engr. Nabeel Nisar** for his support in simulation of mechanical modes of nine cell TESLA cavity. I want to thank **Mr. Ehtisham Khan** for CST simulation of side coupled standing wave structure and very fruitful discussions on various aspects of particle accelerator. I would like to thank the whole LINAC project team for valuable discussion on various aspects of RF cavity for particle accelerators and their support in carrying out this research.

(Waqas Ahmed Toor)

Abstract

Particle accelerators propel charged particles to near-light speeds using radio frequency (RF) cavities that generate the necessary electromagnetic fields. Superconducting RF (SRF) cavities offer higher acceleration gradients, reduced wall losses, and lower RF power requirements, making them particularly advantageous. However, they face challenges such as Lorentz force detuning and beam loading, which disrupt synchronization and affect beam stability.

Lorentz force detuning occurs when electromagnetic pressure causes mechanical vibrations in the cavity walls, leading to fluctuations in the resonant frequency. This detuning effect is problematic because it can cause the cavity to fall out of synchronization with the particle beam, reducing the efficiency of the acceleration process. Beam loading, on the other hand, is caused by the interaction of the particle beam with the electromagnetic fields within the cavity. This interaction alters the cavity's impedance and modifies the accelerating field, leading to variations in beam energy and stability. Together, these phenomena introduce significant instabilities in the accelerator system, making precise control of the cavity fields essential.

This dissertation explores disturbance observer-based control and learning-based disturbance observer algorithms to maintain cavity field stability in the presence of cavity detuning and beam loading. In the learning-based disturbance observer, the disturbance estimate is iteratively improved by minimizing the H-infinity norm of the dynamics from the disturbance to its estimate. The research methodology involves several key steps. First, the dissertation develops a comprehensive model of superconducting cavities, incorporating the dynamics of internal fields and their interactions with external disturbances. Using MATLAB, a cavity simulator is designed to facilitate the analysis and testing of various control strategies. The simulator is employed to implement and evaluate disturbance observer-based control and learning-based disturbance observer algorithms, focusing on their ability to compensate for Lorentz force detuning and beam loading. Iterative learning control is also explored, where the control input is refined over repeated trials to improve cavity field stability. Norm-optimal iterative learning control results are presented for a Finite Impulse Response (FIR) cavity model, demonstrating the effectiveness of this approach in maintaining precise control of the cavity fields.

The main findings reveal that the use of learning-based disturbance observer significantly enhances amplitude and phase stability compared to disturbance observer-based control. This dissertation also provides a concise overview of the fundamental components of low-level RF systems and high-power sources for particle accelerators, with a particular emphasis on high-pulsed-power magnetrons.

In the second phase of research we explore the frequency control problem of high pulsed power magnetron, a possible potential RF source for future superconducting accelerators. Due to the unavailability of a superconducting cavity, experiments were conducted to achieve frequency control of high-pulsed-power magnetrons powering a normal-conducting side-coupled cavity. The results of these experiments are detailed and presented within this work, offering practical insights and experimental validation of the theoretical control strategies discussed.

The contributions of this work include the development of a cavity simulator platform, improved control algorithms for SRF cavities, and detailed experimental results on frequency control of high-pulsed-power magnetrons. These advancements provide valuable insights into the optimization of SRF cavity operation in particle accelerators.

Contents

List of Figures

List of Tables

Abbreviations

ADCs	Analog to digital converters
ADRC	Active Disturbance Rejection Control
AFC	Automatic Frequency Control
AGS	Alternating Gradient Synchrotron
AFF	Adaptive Feed Forward
CCDTL	Cell coupled drift tube linac
CERN	European Centre for Nuclear Research
CW	Continuous Wave
CLK	Clock
DOB	Disturbance Observer based
DTL	Drift tube linac
ESS	European spallation source
FEL	Free electron laser
FPGA	Field-Programmable Gate Array
GDR	Generator driven resonator
ILC	Iterative Learning Control
IOT	Inductive output tube
IIR	Infinite impulse response
LINAC	Linear Accelerator
LDOB	Learning Disturbance Observer Based
LLRF	Low Level Radio Frequency
LEP	Large Electron Positron
LHC	Large Hadron Collider
LQG	Linear Quadratic Gausian
LO	Local Oscillator

LFD	Lorentz force detuning
MBIOT	Multi beam inductive output tube
MO	Master Oscillator
MIMO	Multi input multi output
NDT	Non destructive Testing
PLL	Phase locked loop
PID	Proportional Integrator Derivative
PI	Proportional Integrator
PS	Proton Synchroron
RF	Radio Frequency
RMO	Reference master oscillator
RHIC	Relativistic Heavy Ion Collider
RFQ	Radio frequency quadrupole
SPL	Superconducting proton linac
SRF	Superconducting Radio Frequency
SPS	Super Proton Synchrotron
SSPA	Solid state power amplifier
SOLEIL	"Sun" in French
SBPRIL	Side band power re-injection locked
SEL	Self excited loop
TESLA	Terra electron volt superconducting linear accelerator
TM	Transverse magnetic
TRIUMF	Tri-university meson facility
UAVs	Unmanned air vehicles
VCO	Voltage controlled oscillator
VNA	Vector network analyzer

Symbols

V_a Cavity accelerating voltage

ϕ Synchronous phase

I_b Beam current

V_b Beam induced cavity voltage

V_g RF generator induced cavity voltage in absence of beam

$V_{g,r}$ V_g at resonance

w RF signal frequency

w_{o1} Single cell Resonance Frequency

Q_{o1} Single cell Unloaded Quality Factor

Q_{ext1} First cell External Quality Factor

β_1 First cell input Coupling Factor

Q_{L1} First cell Loaded Quality Factor

R_{L1} First cell Loaded Resistance

κ Cell to Cell coupling factor

γ Cell to beam tube coupling factor

w_{oe} Resonance frequency of end cells

w_{om} Resonance frequency of middle cells

$w_{1/2,L}$ Half bandwidth of the cell with input coupler

$w_{1/2,o}$ Half bandwidth of remaining cells

F Lorentz force on charge article

ΔW Kinetic Energy change

B Magnetic Field intensity

q Charge on particle

$G_n(s)$ Nominal plant transfer function

$G(s)$ Plant transfer function

$Q(s)$ Filter transfer function for disturbance observer

τ Constant

v Velocity of charge particle

E_z Electric field along the cavity axis

K_L Lorentz detuning coefficient

Z_0 Characteristic impedance

Q_L Loaded quality factor

P_{cav} The dissipated RF power in the cavity wall

P_{ext} The emitted RF power out of the cavity through the input coupler

R_L Loaded Resistance

r/Q Normalized Shunt Impedance

v_{CI} Cavity voltage I-component

v_{CQ} Cavity voltage Q-component

G_r Transfer function real part

G_i Transfer function imaginary part

f_{LO} Local Oscillator frequency

f_{RF} RF frequency

f_{IF} Intermediate frequency

d Disturbance

$\hat{d}$ Disturbance Estimate

L Learning function

a Recursive coefficient in LDOB

T_s Sampling time

T_d System's time delay

ω_{inj} Injected signal frequency

ω_o Oscillator free running frequency

$w_{1/2,\pi}$ Half bandwidth of π-mode

$w_{1/2,8\pi/9}$ Half bandwidth of $8\pi/9$-mode

Δw_π Cavity detuning in π-mode

$\Delta w_{8\pi/9}$ Cavity detuning in $8\pi/9$-mode

w_m Resonance frequency of mth mechanical mode

Δw_m Time-varying Cavity detuning for m^{th} mechanical mode

Q_m Quality factor of mth mechanical mode

K_m Lorentz detuning constant of mth mechanical mode

Chapter 1

Introduction

High-energy and high-velocity particle accelerators are essential tools for advancing research in nuclear and particle physics. Superconducting cavities, with their low power losses and ability to achieve high accelerating fields, play a critical role in meeting these demands. This thesis focuses on the control of these high accelerating fields to enhance the performance and stability of superconducting particle accelerators. This chapter introduces the thesis, provides the basic motivation for this research work, and highlights its importance. The chapter is divided into four sections. In section 1.1, the background and introduction to particle accelerator are discussed concisely. Further in section 1.2, applications of particle accelerators are briefly presented. In section 1.3, motivation to do this research, and finally, the organization of the thesis is described in section 1.4.

1.1   Background

A particle accelerator is a machine that uses electromagnetic fields to propel charged particles to very high speeds and energies and to contain them in well-defined beams [1][2]. Historically the charge particle acceleration started with high voltage DC electric field, called electrostatic accelerators, one such accelerator was built by Cockcraft and Walton in 1929. This accelerator produced 400KeV and was used to split Lithium atoms and received the Nobel prize in 1951. In 1924 Ising put forth the idea of utilizing

TABLE 1.1: History of Particle Accelerators

Year	Accelerator	Contribution
1928	Resonance Accelerator by Wideröe	First radiofrequency particle accelerator [1]
1929	Cockcroft-Walton accelerator	Electrostatic acceleration of particles leading to the split of Lithium atom.[2]
1932	Van de Graaff accelerator	Electrostatic acceleration of particles higher than the system voltage [3]
1937	Cyclotron	Continuous acceleration of particles[4]
1952	Synchrotron	High-energy circular acceleration of particles [5]
1954	Linear accelerator (LINAC)	Linear acceleration of particles for radio thearpy [6]
1959	Bevatron	Discovery of antiproton[7]
1960	Alternating Gradient Synchrotron (AGS)	Discovery of the muon neutrino [8]
1968	Proton synchrotron (PS)	Discovery of the charm quark [9]
1971	Super Proton Synchrotron (SPS)	Discovery of the W and Z bosons[10]
1983	Large Electron-Positron (LEP)	Precise measurement of the W boson [11]
1991	Tevatron	Discovery of the top quark [12]
2008	Large Hadron Collider (LHC)	Discovery of the Higgs boson [13]

time-varying fields across drift tubes, a technique referred to as "resonant acceleration." This approach enables the attainment of energies surpassing those achievable with the maximum voltage alone. Using a 1 MHz, 25 kV oscillator, in 1928 Wideröe provided experimental evidence for Ising's principle, effectively generating 50 keV potassium ions, This was the first radio frequency particle accelerator. With time due to development in high-frequency technology, the particle accelerator technology shifted to radio frequency particle accelerators. A particle accelerator is a machine that uses electromagnetic fields to propel charged particles to very high speeds and energies and to contain them in well-defined beams. [1][2]. Historically the charge particle acceleration started with high voltage DC, but with development in RF technology it is shifted to RF accelerators.
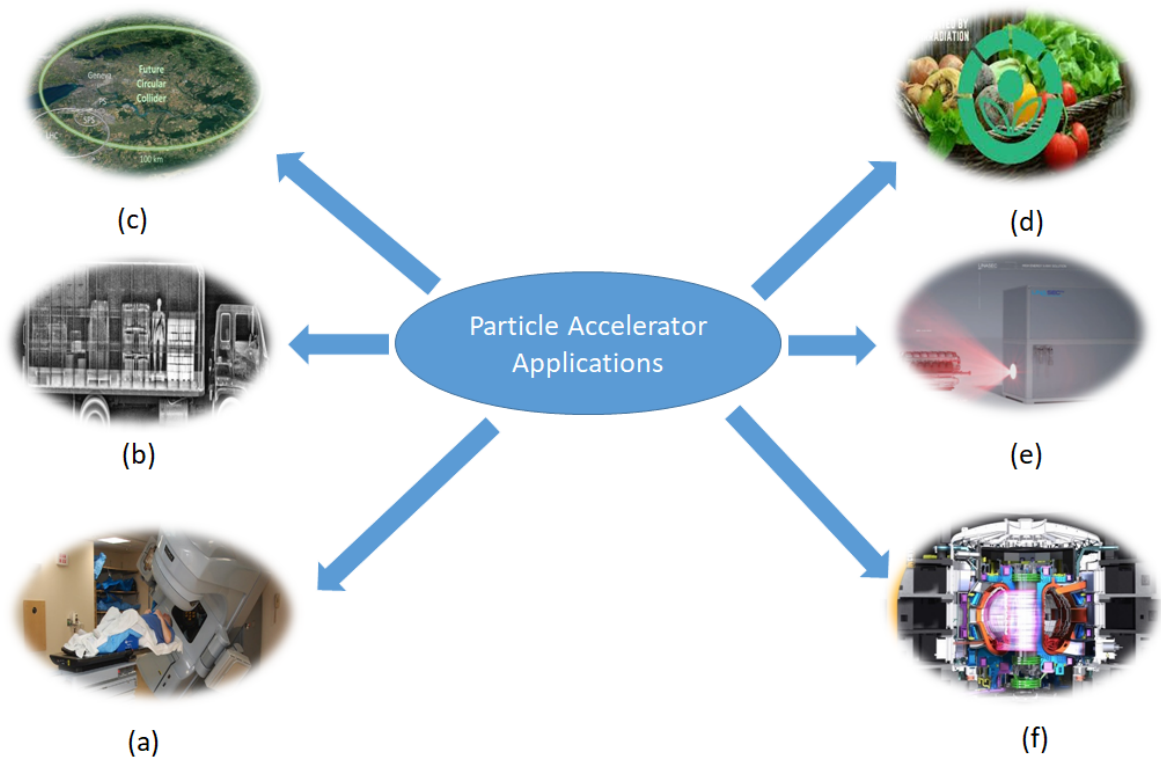
FIGURE 1.1: Partricle Accelerator Applications (a) Medicine, Radiotherapy (b) Security, Cargo scanning (c) Science, LHC CERN (d) Agriculture, Food Irradiation (e) Industry, NDT (f) Energy, TOKAMAK

1.2 Applications of Particle Accelerators

Particle accelerators find diverse applications across various sectors such as medicine, industry, scientific research, exploration, security, and energy, among others depicted in Figure 1.1

Medical Applications: Particle accelerators play a vital role in medical diagnostics and treatments. For cancer treatment using electron, proton, and photon therapy medical LINACs are used. For imaging and diagnosis radiography, and the production of radioisotopes accelerators are also utilized [14].

Industrial Applications: Particle accelerators are utilized in various industrial processes such as materials analysis, semiconductor manufacturing, sterilization of medical equipment, and food preservation through irradiation [14].

Scientific Exploration: These accelerators facilitate fundamental research in fields like high-energy physics, nuclear physics, and particle astrophysics, allowing scientists to investigate fundamental particles, forces, and the origins of the universe [15].

Security: Particle accelerators contribute to security measures through non-destructive testing for identifying material defects [16], screening cargo for contraband and explosives, and scanning luggage at airports for security purposes [17].

Energy Research: Particle Accelerators play a significant role in energy research by replicating extreme conditions relevant to fusion energy production, plasma heating by charge particle beams, studying materials for nuclear reactors [18], and developing advanced nuclear fuels.

Space Exploration: These accelerators aid in space exploration by simulating the effects of cosmic radiation on spacecraft materials, testing propulsion systems [16], and analyzing extraterrestrial samples.

1.3   Motivation

Research in low-level RF (LLRF) control in superconducting particle accelerators holds significant importance for several reasons. First and foremost, LLRF control is essential for maintaining the precision, stability, and efficiency of superconducting particle accelerators. Research in this area aims to optimize LLRF systems to improve the overall performance of accelerators. This can result in higher beam quality, increased energy efficiency, and more reliable operation.

Superconducting accelerators are at the forefront of particle physics research. They are used to explore fundamental particles, forces, and the fundamental nature of the universe. LLRF control research contributes to enabling these accelerators to reach higher energies and intensities, which are crucial for conducting groundbreaking experiments and making discoveries. In an era of growing concerns about energy consumption and environmental sustainability, LLRF control research plays a vital role in making superconducting accelerators more energy-efficient. By fine-tuning the RF control systems, researchers can reduce energy consumption, which is not only cost-effective but also environmentally responsible. LLRF control techniques developed for particle accelerators can contribute to many applications. For example, they can be used in medical accelerators for cancer treatment, industrial material testing, and advanced imaging techniques. Research in this area can lead to practical, real-world solutions with broad societal impacts. Superconducting accelerators are technically challenging to design

and operate. LLRF control research addresses some of these challenges, such as managing high-powered RF fields, minimizing cavity microphonics, and optimizing feedback control systems. Solving these technical issues is essential for the reliable operation of accelerators. LLRF control research is not limited to particle accelerators. It can also benefit the development of other scientific instruments, such as synchrotrons, free-electron lasers, and neutron sources. Improvements in LLRF control can lead to more precise and versatile scientific instruments.

1.4   Organization of Dissertation

In this chapter, an introduction to particle accelerators, their various types, applications, the significance of the field control problem, and the motivation for conducting this research work are presented.

Chapter 2 provides a detailed literature review of cavity field control algorithms and frequency control of magnetrons.

In Chapter 3, the modeling and simulation of single-cell and multicell cavities are addressed. The mathematical model of the single-cell cavity obtained through its equivalent circuit is simulated in MATLAB, and the single-cell cavity is also simulated in CST Microwave Studio. Additionally, the equivalent circuit model of the multicell cavity and its cavity structure is simulated in CST Microwave Studio, emphasizing the effect of passband modes on the accelerating field inside the cavity. In this chapter different components of low-level RF systems are also presented, which are essential for understanding and implementing RF field control in particle accelerators. A brief overview of various RF power sources for particle accelerator cavities is also presented.

Chapter 4 introduces disturbance observer-based control and learning-based disturbance observer approaches for addressing the superconducting cavity field control problem. Simulation results demonstrating cavity field stability in the presence of detuning and beam loading are also provided.

Chapter 5 offers a concise overview of various iterative learning control (ILC) algorithms and presents simulation results of norm-optimal ILC for achieving cavity field stability.

In Chapter 6, high pulsed power magnetron frequency control for accelerator operation is explored . Due to the unavailability of a superconducting cavity, experiments were

conducted to achieve frequency control of high-pulsed-power magnetrons powering a normal-conducting side-coupled cavity. Magnetron frequency control is achieved and frequency twining is avoided, despite an unusually small mode spacing between the accelerating and the immediate neighboring modes of the accelerating cavity.

Finally, Chapter 7 encompasses the summary and conclusion of the dissertation, along with delineating future research directions.

Chapter 2

Literature Review

This chapter provides a literature review of various control algorithms and techniques for addressing the cavity field control problem. It examines the sources of perturbation, including Lorentz force detuning and beam loading. We have considered these two disturbances as they are the most dominant sources of perturbation in superconducting cavity and both are repetitive in nature, linked with the cavity transfer function. Furthermore if we consider other disturbances like microhonics, pulse modulator noise and vacuum pumps noise etc., we would require modeling of the auxiliary systems in particle accelerator facility, which are beyond the scope of this thesis. In the second phase the review of literature for magnetron frequency control for particle accelerators is resented. This chapter highlights the shortcomings and research gaps for further research.

2.1 Cavity Field Control Algorithms

During the last two decades due to rapid development in digital signal processing, many researchers proposed digital control algorithms for field control problems in superconducting accelerator cavities. Due to the enormous computational power of DSP, it became feasible to implement sophisticated control and digital filter algorithms [19]. However, on the other hand, its drawback is added time delay in data conversions and computations associated with digital systems [20]. Superconducting cavities are narrow bandwidth cavities and the main sources of field error in superconducting cavities are

Lorentz force (Radiation pressure induced by the high RF field) detuning, Microphonics (mechanical vibrations), and beam loading [21]. In superconducting RF cavities disturbance can be classified into two categories, predictable (repetitive) and unpredictable disturbances [22]. Lorentz force detuning and beam loading are repetitive disturbances that are repeated from pulse to pulse while microphonics are unpredictable disturbances, generally not synchronized with RF system [21, 23]. Factors that make the field control problem challenging for different accelerator types were presented by Troeng et al.[24]. In this paper, MATLAB simulation results were presented using first order low pass filter cavity model, low-frequency disturbance with unit step transfer function, and PI controller. the cavity model used is as under

$$G(s) = \frac{\omega_{1/2}}{s + \omega_{1/2} - j\Delta\omega}. \tag{2.1}$$

Where $\omega_{1/2}$ is the cavity half bandwidth and $\Delta\omega$ is cavity detuning. The simulation results showed that low-bandwidth cavities were sensitive to measurement noise and high-bandwidth cavities were sensitive to load disturbance, which is why it is harder to achieve field errors of 0.2% for higher bandwidth cavities than to achieve 0.01% field errors for superconducting cavities, having a narrow bandwidth. Review of different cavity field control algorithms are described and their summary is given in Table 2.1.

2.1.1 Disturbance Observer Based Control

The implementation of disturbance observer-based (DOB) control for the pulsed superconducting linear accelerator and general overview of the low-level RF control were presented by Feng et al [25]. In this work Cavity RF signal of 1.3 GHz was down-converted to 10 MHz intermediate frequency (IF) and then sampled at 80 MHz by 16 bits ADC. The I/Q components of the IF signal were extracted and then filtered by a 250 KHz fourth-order IIR filter to remove cavity parasitic modes. IQ values were compared with set point tables of I/Q values and I/Q errors were calculated and regulated using a Proportional Integrator (PI) feedback controller. The regulated I/Q signals were added with a static feed-forward table and disturbance observer-based (DOB) controller output and fed to the I/Q modulator to modulate the master oscillator RF signal. In the cavity, operated at a higher accelerating voltage of 10.5 MV instead of 7.5 MV drift

in Lorentz force detuning (LFD) was coupled not only with RF phase but also with RF amplitude and these drifts were transferred to beam energy. The cavity voltage amplitude was less sensitive to detuning drift compared to the cavity voltage phase as long as the cavity was operated at resonance. The offset frequency between measured and actual limited the pulse-to-pulse stability as the PI-feedback control is not sufficient to reject the detuning drifts. Another limitation was the long pulse beam loading. In principle, beam loading can be compensated by high feedback gain but this approach increases the risk of unstable system and noise levels in high frequency components. RF trips occur because of high feedback gain, therefore higher feedback gains were avoided.

The structure of the DOB control is illustrated in Figure 2.1. Signals u, d and $\hat{d}$ repre-
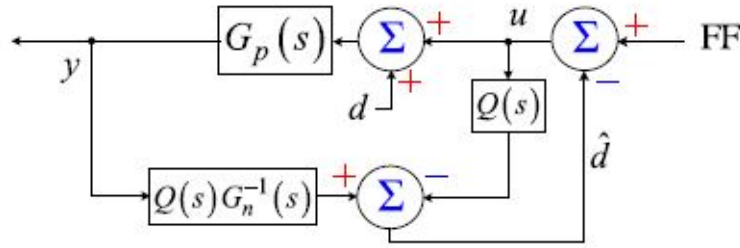
FIGURE 2.1: Basic Structure of DOB Control [25]

sent plant input, disturbance, and disturbance estimate, respectively, and 'FF' is input from the feedforward table. Models Gp and Gn represent the transfer function of the real plant (combination of the cavity, RF source, preamplifier, IQ detector, etc.) and nominal system models, respectively. Generally nominal plant model can be obtained by modern system identification tools but if the cavity half bandwidth is much smaller than other components then the dominant pole is introduced by the cavity itself. In ideal conditions when cavity detuning is well compensated by tuners and phase calibration-errors are negligible the nominal plant transfer function G_n is given by

$$G_n(s) = \frac{K.2\pi f_{0.5}}{s + 2\pi f_{0.5}}. \tag{2.2}$$

where the parameter K and $f_{0.5}$ is plant gain and cavity half bandwidth respectively. The filter $Q(s)$ was used to make the G^{-1} realizable. In this paper the second-order filter was used, whose transfer function depends on the variable τ, which is related to filter bandwidth.

$$Q(s) = \frac{1}{(\tau s + 1)^2}. \tag{2.3}$$

In another paper, Dongbing Li et al [26] used disturbance observer-based control for suppression of low-frequency microphonics. The nominal plant model used was a first-order low pass filter assuming resonance operation of the cavity, so the only parameter used in the plant model transfer function was cavity half bandwidth and the Plant model was not estimated in run time. The filter Q was used to make the inverse of the plant model transfer function realizable. Three types of filters with the same bandwidth were studied first order, second order, and third order. The third-order filter gave the best results at the cost of more computations. So the second effective filter in suppressing noise was selected as a compromise between noise suppression and computational complexity. A higher bandwidth filter showed better results in suppressing noise at low frequencies but might induce instabilities. Results clearly showed that PI+DOB control suppress the microphonics noise and desired amplitude and phase stability of 0.008% (rms) in amplitude and 0.005 degree (rms) in phase was achieved.

2.1.2   Iterative Learning Control

RF control optimization and Automation for linear accelerator was presented by Zheqiao Geng [27]. In this paper practical aspects of LLRF were considered and several algorithms and procedures were described such as calibration of DAC offset to reduce RF leakage from vector modulator, calibrating the RF signal group delay, and flattening the intra-pulse phase distribution with adaptive feed forward. For RF pulse flattening, the ILC algorithm and its limitations were presented. ILC is effective with the RF system having a fast response to the input. It can be used for flattening small ripples in the pulse but not for large step variations, that's why it was activated after the filling time of the cavity in the middle portion of the pulse. The continuous operation of the ILC algorithm was not suggested as the error will accumulate from pulse to pulse at the rise of each pulse.

2.1.3   Hybride DOB and ILC Control

Although DOB control can compensate for both predictable (repetitive) and unpredictable disturbances, its performance is limited by the bandwidth of filter Q used in

the DOB approach [25]. Iterative learning control(ILC) can compensate for predictable (repetitive) disturbances and it is not bandwidth-limited. To utilize the advantages of both DOB control and ILC control Feng et al [28] demonstrated a combination of both algorithms in a cavity simulator-based test bench, to compensate for predictable or repetitive disturbances (LFD and beam loading, etc) and unpredictable disturbances (microphonics, etc.). In the ILC approach, error information gathered from the last cycle is estimated and used to improve the current cycle. Many advanced ILC algorithms are in practice for performance improvement, fast convergence rate, and robustness. In this paper [28] plant-inversion-based algorithm was selected due to its fast convergence rate. Results showed that with Proportional (P) control only, a very clear effect of beam loading was observed (approx. -0.25%) in amplitude and a tilt in the phase waveform. This is well compensated by the P+DOB control but the beam loading effect still existed in the amplitude at the heads and tails of the beam. This was because the very steep edge of the beam induced very high frequency components and the Q-filter in DOB control had 3 KHz bandwidth. This Beam loading effect was well compensated by P+ILC control but a small tilt still existed in phase, which may be due to microphonics or 10% beam fluctuation in the simulator model. In the case of P+DOB+ILC control both the beam loading effect and phase tilt were perfectly compensated. A zero-phase FIR filter was used with ILC control which improved the performance of ILC control.

2.1.4   Active Disturbance Rejection Control

In another paper by Zheqiao Geng [29] disturbance observer-based technique was simulated for both disturbance rejection and cavity modeling. Beam loading, Lorenz force detuning, microphonics, and uncertainty in measurements were considered disturbances, so the Active disturbance rejection control (ADRC) was used as robust control. The model of the cavity used is given by

$$\frac{dV_a}{dt} + (\omega_{1/2} - j\Delta\omega)V_a = 2\omega_{1/2}(V_g + V_b). \tag{2.4}$$

where, V_a is the phasor representation of cavity voltage, V_g and V_b are effective driving voltage phasors for RF power and beam loading. In this paper disturbance observer was used to estimate the cavity parameters in runtime, which were used for the optimization
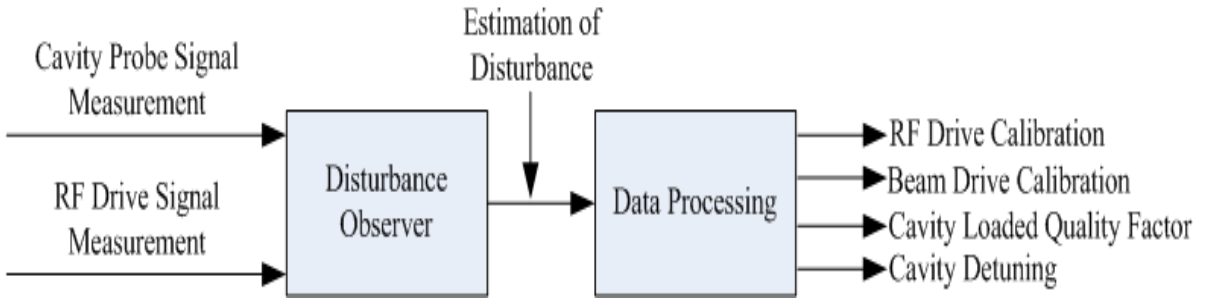
FIGURE 2.2: Cavity model Identification with disturbance observer [29].

of the control process, the process of cavity model identification is given in Figure 2.2 To make the ADRC effective, the poles of the observer were placed at ten times the poles of close loop cavity control system. ADRC gave promising results as an alternative to the existing PI control. Simulation results showed that ADRC resulted in better suppression of voltage errors compared to proportional feedback control in both amplitude and phase during the flat top of pulse, also the ADRC provided faster rise time compared to proportional feedback control. For beam loading compensation feed forward control was considered. Since initially for the first pulse, the beam cavity parameters were not estimated, the feed-forward signal was calculated by the desired beam current, and for the rest of the pulses, the feed-forward signal was refined by the estimated beam voltage from the disturbance observer, ILC can be an option for feed-forward signal calculation. Since uncertainties in detuning measurement cause errors or fluctuations in beam identification, so detuning of the cavity without a beam was used to decouple contribution to disturbance by detuning and beam loading after the beam is switched on. For better beam phase measurement results of 100 pulses were averaged.

2.1.5 Linear Quadratic Gaussian Control

Bielawski et al. described the developments in CERN LINAC-4 LLRF [30]. In the feedback controller previously, a simple PI controller was used for controlling variation due to beam-induced voltage. A more robust solution, linear quadratic Gaussian (LQG) was applied for faster and more precise regulation. Kalman predictor using the model of observed process reliably estimated the next states of the system so that faster feedback was achieved. The control card had the model of a cavity (a low pass filter) and cables (delay line). Cavity output state was available and intermediate states were estimated

in the estimator for faster feedback. Since the LINAC4 machine had different types of cavities so cavity model needed to be tuned to match the type of cavity in the cavity control loop card. For transient beam loading compensation Adaptive feed forward was used because even with the improved LQG +Kalman feedback, it was not possible to eliminate transient beam loading observed in the first 10μsec. Since transients repeat at every pulse, so feedforward solution can be used [31–33]. Simulation results showed that with the combination of feedback and adaptive feedforward, the transient beam loading effects were much reduced [30].

2.1.6 Sliding Mode Control

In another paper R. Leewe et al [34] presented resonance frequency tuning using reflected power by sliding mode extremum seeking control. Since the RF cable's phase noise is dependent on temperature, so in an environment where temperature is not controlled resonance frequency tuning by phase of the cavity is time and labor extensive. Reflected power can be measured at the cavity and the DC signal can be sent to the control room for computation without errors, so resonance tuning through reflected power has an advantage in the scenarios, where temperature is not controlled like in TRIUMF's. For sliding mode extremum seeking algorithm simulation, two variables were analyzed as input to the controller, reflected power and reflected voltage. Results showed that the reflected rms voltage input variable yielded faster convergence and smaller oscillation amplitude around the optimum operating point as compared to reflected power as input to the controller.

2.1.7 Adaptive Feed Forward Control

In another paper, by C.Y.Xu et al.[35], feed-forward control of CiADS proton accelerator was simulated for beam loading compensation. The purpose of this study was to find the threshold limit of beam parameter variation, which could be compensated by feed-forward control for desired stability specifications. The parameters studied were beam current ripple frequency for different beam current amplitudes and beam arrival time mismatch with feed-forward control activation. Deviation margins were found for these

parameters for amplitude stability of 0.1% rms and phase stability of 0.1 degrees.

Adaptive feedforward cancellation (AFC) provides a method for canceling internal and external sinusoidal disturbances with known frequencies. Kandil et al [23] demonstrated the use of piezo-electric actuators and adaptive feedforward control to damp sinusoidal disturbances due to microphonics in Superconducting RF cavities. AFC estimated the magnitude and phase of the sinusoidal disturbances inputs and generated a control signal to cancel their effect. Zhenyang Lin et al [36] proposed a high-voltage feedforward technique for correcting the RF phase noise due to high-voltage pulse variation. During the RF signal amplification by Klystron, the phase difference between the low-power input signal and the high-power output signal is mainly due to the high-voltage pulse amplitude variation. A proportional coefficient between RF phase variation and high voltage feedforward term was found by measurement and then a suitable high voltage feedforward signal was applied to correct the RF phase in a low-level RF system. For this purpose, an accurate measurement of high voltage signal was required. Results show that the RF phase jitter was much improved when the high voltage feedforward system was on as compared to its off state and the high voltage feedforward system can effectively reduce the noise caused by modulator pulse voltage variation. The theoretical control accuracy of this technique was dependent on the accuracy of voltage measurement of the high-voltage pulse. Since the RF phase depends on several factors like cooling water temperature, circuit noise, and power supply noise, therefore the phase stability was improved by optimizing the whole LLRF system.

2.2   Magnetron Frequency Control

In the second phase, review of magnetron frequency control techniques is presented in this section and is summarized in Table 2.2. RF power source frequency stability is very crucial for stable operation of particle accelerator.

Tahir et al.[38] developed methods for precise frequency and phase control of a 1.2 kW CW cooker magnetron. Using a digital frequency synthesizer IC in a negative feedback loop, the study achieved stable frequency locking to a 10 MHz reference. The investigation included characterizing magnetron operation under various conditions and implementing DSP-based feedback control to improve phase jitter performance. A.C.

TABLE 2.1: Literature Review Summary

Authors	Years	Topology							Sources				Type	
		PI	DOB	ILC	ADRC	LQG	AFF	others	Microphonics	LFD	Beamloading	Power Supply	Simulation	Implementation
Simrock [37]	2003							✓	✓					✓
Kandil [23]	2005						✓		✓					✓
Qiu [22]	2015	✓	✓						✓		✓	✓	✓	✓
Geng [29]	2017	✓			✓				✓	✓	✓		✓	
Z.Lin [36]	2018						✓					✓		✓
Leewe [34]	2018							✓					✓	
Troeng [24]	2019	✓											✓	
Bielawski [30]	2019	✓				✓	✓	✓					✓	
C.Y.Xu [35]	2019						✓				✓		✓	
Qiu [25]	2021	✓	✓							✓	✓		✓	
Qiu [28]	2021	✓	✓	✓					✓	✓	✓		✓	
D.Li [26]	2021	✓	✓						✓				✓	

Dexter [39] reviewed the use of injection locking for magnetron to power superconducting proton linear accelerators. The study examined phase locking of low-power cooker magnetron through external injection signals and controlling the magnetron current, assessing the feasibility of magnetron as RF sources for long-pulse superconducting accelerators.

In [40], Kazakevich et al. showcase how a pulsed magnetron's power and phase can be regulated using injection locking. They achieve this by using the output from a continuous wave traveling wave tube amplifier, which is driven by a solid-state signal source. The paper also offers a comprehensive mathematical explanation of how the injection signal regulates power.

Zhang et al. [41] conducted a thorough study on how anode voltage ripple affects the

injection locking of a magnetron, particularly focusing on the frequency pushing effect. Their theoretical analysis and experimental results revealed that increased power supply ripple reduces the magnetron's locking bandwidth. This research is pivotal for achieving stable injection locking, emphasizing the importance of balancing power supply ripple and the frequency pushing effect to ensure high-quality output.

Kazakevich et al. [42] developed a straightforward analytical model to fine-tune the parameters of an RF resonant injected signal used to drive magnetrons. Their experiments confirmed the model's accuracy, showcasing its potential for quickly controlling the power of magnetrons in high-current superconducting accelerators.

In another paper Kazakevich et al. [43] introduced a groundbreaking technique for operating magnetrons in pulsed mode without needing pulse modulators by powering them below the self-excitation threshold voltage. This innovative method allows for stable and controllable operation with high efficiency.

In [44] Kazakevich et al. dedicated their research to enhancing the stability of beam current and magnetron frequency within a microtron injector aimed at a Far-Infrared Free Electron Laser (FEL). Their efforts yielded notable advancements in stabilizing the output lasing power, showcasing the potential of stabilized magnetron-driven microtrons for advanced FEL applications.

Pengvanich et al. [45] developed a phase-locking model from circuit theory to explain various regimes observed in magnetron injection-locking experiments. Their model recovered many of the phase-locking frequency characteristics observed in experiments, providing insights into the behavior of injection-locked magnetrons.

Ye et al. [46] presented a side band power re-injection locked (SBPRIL) magnetron. Their theoretical analysis and experimental results showed significant improvements in spectrum peak and phase noise performance, validating the effectiveness of the SBPRIL approach.

Yue Song et al. [47] analyzed the effects of a mismatched circulator on the injection-locked magnetron's phase differential equation and locked bandwidth. The study provided numerical calculations showing the impact of circulator reflection coefficients, aiding in the design of more robust injection-locked systems.

In another paper by Mitani et al. [48], the research outlines the creation of a phase-controlled magnetron for expanded applications. Using injection locking and phase-locked loop circuits, the developed magnetron achieves kHz-class pulse operation with

precise frequency and phase control, showcasing significant improvements in pulse-driven applications.

In their works [49, 50], Choi et al. detail experiments aimed at achieving frequency locking and reducing noise in a 2.455 GHz magnetron through a feedback loop. By incorporating a high-Q cavity within the loop, they successfully achieve substantial noise reduction and precise frequency control. These studies highlight the effectiveness of self-injection locking in ensuring stable magnetron operations, underscoring its practical relevance in RF applications.

In another paper by Bilokh et al.[51], the study focuses on enhancing magnetron output power through a feedback loop that injects a portion of the output signal back into the magnetron. This self-injection locking mechanism improves power output and reduces phase noise, making the system more efficient. the portion of the output is fed back to the magnetron using an additional circulator and a cavity filter tuned to the desired microwave frequency. In this work study of the circulator leakage leakage is not considered, furthermore low power magnetron is used in experimentation. In utilizing this technique for High pulsed power magnetron designing of cavity filter and its tuning would be challenging due to high surface fields and arcing on movable parts.

2.3 Gap Analysis

Lorentz force detuning and beam loading are significant challenges in the operation of superconducting cavities. These effects can destabilize the accelerator, leading to performance degradation. Traditional methods for dealing with these issues involve feed-forward and feedback control systems that are often complex and less adaptive to changing conditions. Many researchers have proposed combining Disturbance Observer-Based (DOB) control and Iterative Learning Control (ILC) with traditional PI control to address Lorentz force detuning and beam loading compensation. However, the main limitation of these algorithms is that, despite the repetitive nature of disturbances, their estimation and compensation are hindered by imperfections in the plant model. To enhance compensation for beam loading and detuning, the estimation process must be improved.

Zheng et al. proposed a learning-based disturbance observer and experimentally tested

Table 2.2: Literature Review Summary (2nd Phase)

Authors	Years	Topology				Magnetron				Type	
		Ext. Injection	Self Injection	pushing	others	CW	Pulsed	Low Power (KW)	High Power (MW)	Theory\Simulation	Experiment
Pengvanich et al. [45]	2005	✓				✓		✓		✓	✓
Choi et al.[49]	2007		✓			✓		✓			✓
Mitani et al. [48]	2007	✓		✓		✓		✓			✓
Choi et al. [50]	2008	✓	✓			✓		✓			✓
Tahir et al. [38]	2008	✓		✓		✓		✓		✓	✓
bliokh et al.[51]	2011		✓			✓				✓	
Kazakevich et al. [44]	2011		✓				✓		✓		✓
Dexter et al. [39]	2011	✓	✓	✓			✓	✓		✓	✓
Yue et al. [47]	2014	✓								✓	
Kazakevich et al. [52]	2014	✓				✓		✓		✓	✓
Kazakevich et al.[40]	2016		✓				✓	✓			✓
Ye et al. [46]	2016	✓				✓		✓		✓	✓
Kazakevich et al. [42]	2018	✓				✓		✓		✓	✓
Kazakevich et al. [43]	2020	✓					✓	✓			✓
Zhang et al [41]	2022	✓		✓		✓		✓		✓	✓

the algorithm on UAVs in their work [53]. In this technique, the disturbance estimate is iteratively improved by minimizing the H-infinity norm of the dynamics from the disturbance to its estimate. To the best of our knowledge, such a learning-based disturbance observer controller has not been explored for compensation of Lorentz force detuning and beam loading in superconducting particle accelerators. The design of such a controller for the aforementioned problem, along with any necessary modifications and performance analysis compared to existing techniques, represents a research gap that this thesis aims to address.

In the second phase of research, we explored the frequency control of high pulsed power

magnetron, a potential possible RF power source for superconducting accelerators. Magnetron injection locking is a technique in research to stabilize the magnetron's frequency to power superconducting cavity, which generally requires an external stable high-power source. Implementing this method involves additional hardware, which significantly increases costs, especially for megawatt power magnetron. Addressing this issue, this thesis explores alternative solutions to mitigate the impact of mode jumping without relying on costly external frequency locking mechanisms. By focusing on the underlying causes and potential improvements in high pulsed power magnetron operation, the research aims to fill this critical gap in the field. We used a normal conducting cavity as load due to unavailability of superconducting cavity and the cryogenic system. The cavity used had unusually small mode spacing between accelerating $\pi/2$ and neighboring mode. Superconducting cavities operated in π-mode which has smaller mode spacing as compared to $\pi/2$-mode. In normal conducting cavities, fabrication imperfections can lead to a very narrow mode spacing between the accelerating mode and its nearest neighboring mode. This narrow spacing can make stable operation challenging when the cavity is powered by a high-pulsed power magnetron, as the system becomes susceptible to mode jumping. Mode jumping occurs when the magnetron unintentionally locks onto a neighboring mode instead of the desired accelerating mode, leading to instability in operation.

2.4   Problem Statement

"Improve superconducting cavity field amplitude and phase stability, in the presence of Lorentz force detuning and beam loading by better estimation and compensation of disturbances".
Lorentz force detuning and beam loading compromise cavity field amplitude and phase stability, leading to degraded beam quality and accelerator performance. Better estimation and compensation of these disturbances will significantly improve the amplitude and phase stability. In the existing literature, the application of learning-based disturbance observer control technique for superconducting cavity field control has not been explored. This research gap highlights the need for a novel approach to enhance

cavity field stability by effectively mitigating repetitive disturbances and improving control precision. The main methodology we adapted to address this problem would be Designing a learning based disturbance observer controller for superconducting cavity field amplitude and phase stability that iteratively improve the estimation of repetitive disturbances like cavity detuning and beam loading.

2.5 Research Objectives

In particle accelerators, cavity voltage stabilization is fundamental to ensuring consistent energy transfer to particles, maintaining high-quality, low-emittance beams, achieving effective synchronization across accelerator systems, ensuring reliable operation under perturbations, and meeting the stringent requirements of demanding applications such as Free Electron Lasers (FELs), medical therapy, and precision experiments.
The following research objectives are proposed to address critical challenges in cavity field stabilization and will be explored during the course of this study:

1. Design a learning based disturbance observer controller for superconducting cavity field amplitude and phase stability that iteratively improves the estimation of repetitive disturbances like cavity detuning and beam loading. The disturbance observer-based control (DOBC) has been studied extensively in the available literature for this problem, the application of learning-based disturbance observers for addressing these challenges remains largely unexplored, presenting a promising avenue for further investigation.To achieve this objective, the following control strategies will be simulated and evaluated:

   - Mitigate effects of disturbances on the system using Disturbance Observer-Based Control.

   - Prediction and compensation of disturbances with Learning-Based Disturbance Observers.

   - Apply iterative methods to improve control performance over repetitive operations using Iterative Learning Control.

2. Develop a cavity simulator incorporating main sources of field perturbations in superconducting cavities, namely cavity detuning and beamloading. A simulator that models the effects of cavity detuning and beam loading is an invaluable tool for testing and refining control algorithms without the need for costly physical setups. Developing such a simulator not only aids the current research but also provides a platform for academic and industrial researchers to explore and validate new control strategies in a cost-effective manner. Furthermore cavity RF simulations give more insight to cavity model simulation for cavity field control.

3. Frequency control of high-pulsed-power magnetrons, a promising RF power source for particle accelerators, presents unique challenges. While low-power magnetron injection locking has been extensively studied in the literature, there is a notable gap in research concerning the stable frequency operation of high-pulsed-power magnetrons. Specifically, the interaction between high-power magnetrons and narrow mode-spacing cavities remains under explored, highlighting the need for further investigation in this area.

2.6 Summary

This chapter offers an extensive literature survey concerning cavity simulators and control algorithms designed to address cavity detuning and beam loading. The second phase of literature survey is about frequency control of magnetron for accelerator application including self injection locking, external injection locking and frequency pushing. Through this review, a few shortcomings in the existing literature are identified, thereby emphasizing research gaps that this study endeavors to fill. Furthermore, some of these gaps are identified as potential avenues for future research.

Chapter 3

Accelerator System Modeling and Simulation

3.1   Introduction

A detailed model of the system being controlled is essential for understanding its dynamics, behavior, and response to inputs and disturbances. This knowledge forms the basis for designing an effective controller. Modeling helps identify key parameters and characteristics of the system that influence the design and tuning of the controller. In this chapter, we explain basics of charge article accelerator and their types. We thoroughly explained the mathematical modeling of the RF cavity for the field control loop, presented in Figure 3.1. The three sections, RF accelerating cavity, Low-level RF system (LLRF), and high-power RF system are discussed in this chapter. We conduct simulations in CST Microwave Studio to analyze the internal field dynamics of both single-cell RF cavities and multicell RF cavities. Additionally, we describe and simulate their circuit models for transfer functions using MATLAB. The impact of cavity detuning on the accelerating electric field is elucidated through the step response of the cavity model. In the case of multicell cavities, we simulate an electromechanical model to analyze the effects of mechanical modes on cavity detuning. Natural mechanical modes are simulated in ANSYS. High power RF sources and low level RF blocks are also briefly explained in this this chapter.
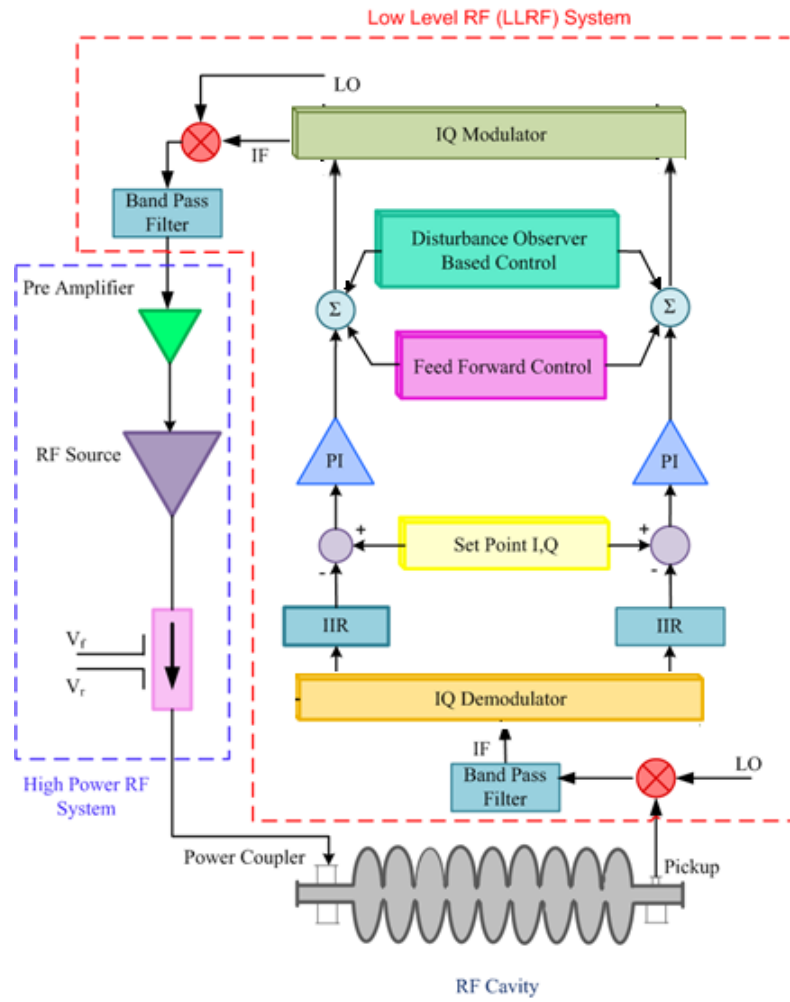
FIGURE 3.1: A generalized block diagram of the Field control loop in LLRF

3.2 Principle of Charged Particle Acceleration

Particle accelerators utilize electric fields to increase the speed and energy of a particle beam, with magnetic fields guiding and concentrating these particles. The particle source supplies the particles like protons or electrons that need acceleration. The particle beam travels in the vacuum confined within a metal beam pipe. Electromagnets guide and focus the particle beam during its journey through the vacuum tube. The oscillating electric field inside metal enclosures accelerates these charged particles. These metal enclosures are called RF cavities. RF cavity is a key component of modern particle accelerators, which transfer energy to charge particle beams. The resonance frequency of these RF cavities varies from 100 MHz to a few GHz depending on applications. Normal conducting cavities are made of copper and superconducting cavities are usually made of niobium. Superconducting cavities have the advantage of much lower wall

losses as compared to normal conducting cavities another significant advantage is that superconducting cavities have larger aperture than copper cavities resulting in reduced beam-cavity interaction, higher beam current and higher beam quality [1]. The basic principle of charge particle acceleration can be described by the Lorentz force acting on charge q moving with velocity v in the presence of electric field 'E' and magnetic field 'B'.

$$F = q(E + v \times B). \tag{3.1}$$

The amount of work done by the force 'F' in moving charge 'q' through distance 'l', is converted to the kinetic energy gain 'ΔW' of charge particle given by

$$\Delta W = \int F.dl = q \int E.dl + q \int (v \times B).dl. \tag{3.2}$$

since the distance can be represented by $dl = vdt$ therefore kinetic energy change 'ΔW' is given by

$$\Delta W = \int F.dl = q \int E.dl + q \int (v \times B).vdt = q \int E.dl. \tag{3.3}$$

Equation 3.3, shows that the magnetic field is not responsible for charged particle acceleration, we must rely on electric fields for particle acceleration. To accelerate particles we need to confine the electromagnetic waves to a specific region and generate an electric field along the direction of particle motion. This is achieved by designing a Radiofrequency cavity for accelerating mode. A simple standing wave cavity can be constructed by adding end walls to a cylindrical waveguide. In a standing wave cavity, the incident wave with electric field amplitude $'E'_o$ and frequency $'\omega'$ traveling in the '+z' direction will reflect from the cavity end wall and will travel in the '-z' direction. The resulting electric field 'E_z' is given by

$$E_z = E_o[\cos(kz - \omega t) + \cos(kz + \omega t)],$$

$$E_z = E_o[\cos kz \cos \omega t + \sin kz \sin \omega t + \cos kz \cos \omega t - \sin kz \sin \omega t],$$

$$E_z = 2E_o \cos kz \cos \omega t,$$

$$E_z = F(z) \cos \omega t. \tag{3.4}$$

In Equation 3.4, the resulting electric field's time and spatial dependence are separated. This is called a standing wave since the field profile depends on position, not on time.

3.3 Types of Particle Accelerators

Particle accelerators can be classified based on several factors: the nature of the RF cavity (traveling wave or a standing wave), the material of the cavity (normal conducting or superconducting), the type of charged particle being accelerated (such as electrons or protons) and the intended application (collider or free electron laser). This classification scheme provides a comprehensive framework for understanding the diversity of particle accelerator designs and functionalities. A brief overview of these classifications is provided here.

3.3.1 Travelling and Standing Wave Accelerator

In a traveling wave cavity, two RF power couplers are installed: one for RF power entrance and the other for its exit towards the matched load. The RF power enters a cell near the gun or charged particle entrance, traverses through all cells, and eventually exits the cavity towards the matched load as shown in Figure 3.2(a).

In contrast, in a standing wave cavity shown in Figure 3.2(b), the RF power enters the cavity, travels through all cells, and then reflects to the power coupler, forming a standing wave inside the cavity. In traveling wave cavities, precise phase advancement between each cell is crucial for achieving the desired energy gain of particle beams. On the other hand, in standing wave cavities, the suppression of unwanted modes poses a significant challenge.

Traveling wave cavities typically have larger dimensions due to on-axis coupling. In contrast, in standing wave cavities, the coupling cells can be moved off-axis, creating a side-coupled cavity design, which results in a shorter length compared to traveling wave cavities. To take advantage of both types of accelerators hybrid schemes of both traveling and standing wave accelerators are also utilized [54]. In few commercial cargo scanner LINACs bunching section is standing wave while traveling wave cavities used in accelerating section.
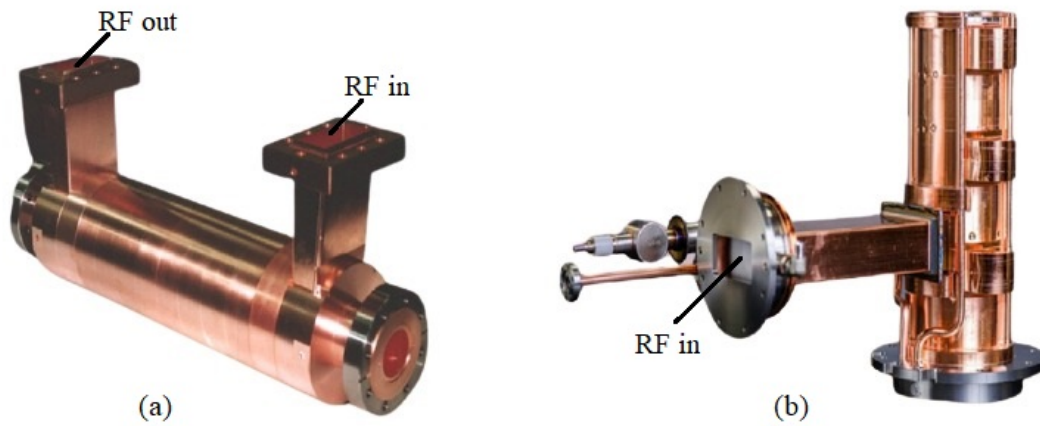
FIGURE 3.2: (a) S-band Travelling wave cavity [55] (b) S-band side coupled standing wave cavity [56]

3.3.2 Normal and Superconducting Accelerator

The choice of material for the accelerator cavity can either be copper (normal conducting) or niobium (superconducting), each with its own set of advantages and drawbacks. Normal conducting cavities are well-suited for pulsed operations but not continuous wave operations due to higher wall losses. Additionally, they require higher peak power RF amplifiers compared to superconducting accelerators. On the other hand, superconducting cavities necessitate a cryogenic system for operation, and tuning issues are more complex than with normal conducting cavities. In Figure 3.3(a) five-cell Neubium superconducting elliptical cavity for proton acceleration is shown alongside in Figure 3.3(b) a drift tube linac cavity for the same purpose is presented [57, 58]. To reduce the strain on the cryogenic system, the walls of superconducting cavities are considerably thinner compared to those of normal conducting cavities. Consequently, in superconducting cavities, Lorentz force detuning emerges as a significant source of field perturbation. Additionally, compensating for microphonics is desirable to enhance field regulation within the cavity. In normal conducting cavity the lorentz force detuning does not cause significant frequency detuning due to thick walls.

3.3.3 Electron and Proton Accelerator

Electrons are significantly lighter particles, compared to protons or ions, causing them to reach relativistic speeds at much lower electric potentials. Consequently, the design
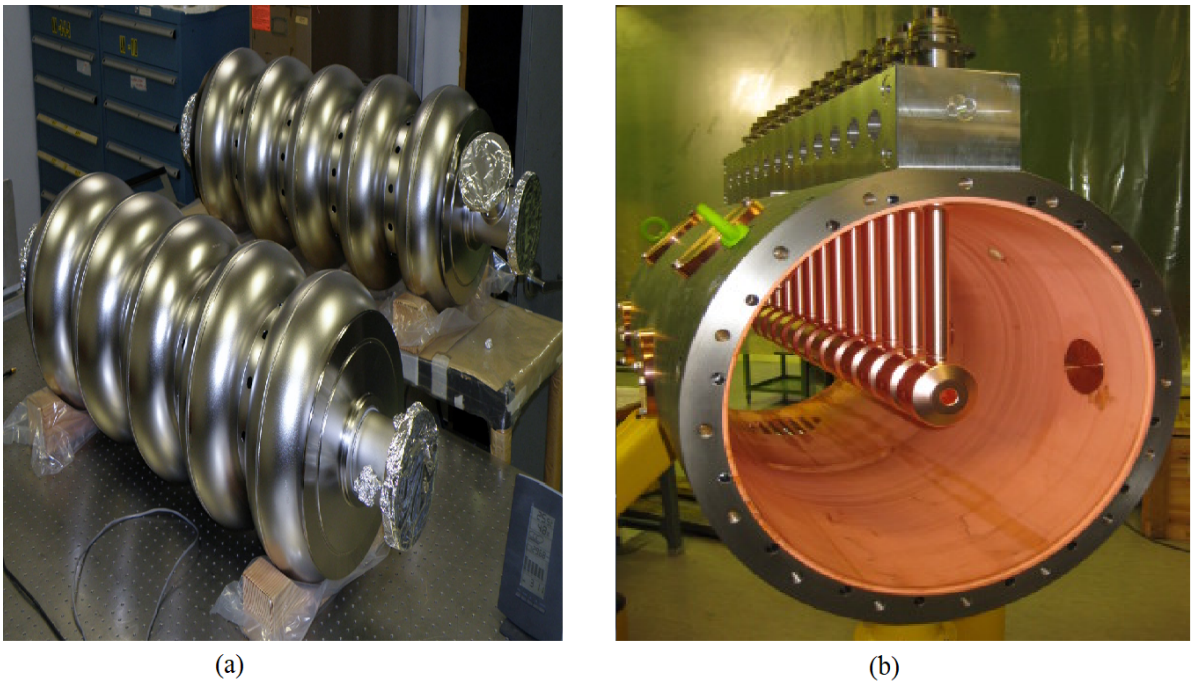
FIGURE 3.3: (a) Five cells Superconducting Proton Accelerator Cavity [59] (b) Normal Conducting Drift Tube Proton Accelerator Cavity [60]

considerations for electron accelerator cavities differ significantly from those for proton accelerators. Proton accelerators employ various types of cavities, such as LINAC-4 cavities Radio frequency quadrupole (RFQ), Drift tube linac (DTL), Cell coupled drift tube linac (CCDTL), and Superconducting proton linac (SPL) are specifically tailored for high-energy proton beams [58].

3.3.4 Collider and Free Electron Laser

Collider and FEL are classifications of particle accelerators according to application. A collider typically refers to a particle accelerator facility where particles are accelerated to very high energy and made to collide with each other. These collisions allow scientists to study the fundamental properties of matter and the universe. Some famous colliders include the Large Hadron Collider (LHC) at CERN in Switzerland and the Relativistic Heavy Ion Collider (RHIC) at Brookhaven National Laboratory in the United States. Whereas FEL is a type of laser that uses a beam of electrons traveling freely through a magnetic structure to generate coherent electromagnetic radiation. The high-energy electrons are produced by particle accelerator cavities. Field control requirements of FEL are much higher than proton linac or colliders [24].

3.4   Cavity Field Control Challenges

Low-level RF control in a particle accelerator presents a significant challenge due to its extensive reach across various disciplines. This encompasses RF cavity electrodynamics, mechanical modes, beam dynamics, as well as the operation of electron guns and pulse modulators. Virtually every system within a particle accelerator is interconnected with low-level RF control. To put it differently, experts in low-level RF require a comprehensive understanding of nearly every facet of particle accelerator systems.

Requirements and challenges of Cavity field control may vary based on the type of accelerator ' Linear or circular', the type of RF cavity 'normal or superconducting', the charged particle to be accelerated 'electron or hydron or heavy ions' and the application of accelerator collider or free electron laser, etc.

3.4.1   Sources of Field Perturbations

The stable operation of a superconducting accelerator requires the identification and control of sources of perturbation in the RF field inside the cavity. There are many sources of field perturbation; two of them, considered in this research work are described here.

3.4.1.1   Lorentz Force Detuning

A change in cavity resonance frequency due to deformation by electromagnetic pressure is called Lorentz force detuning. In a pulsed superconducting accelerator on every pulse rising and falling edge due to electromagnetic pressure the cavity shape is deformed and the resonance frequency is changed, electromagnetic pressure on the half cell of the elliptical cavity is shown in Figure 3.4, near the axis the Lorentz pressure is inward while at the equator the pressure is outward [60, 61]. Due to Lorentz force detuning cavity voltage and phase being changed during the pulse, reflected power is increased and the repetition rate of RF pulses is also limited. Lorentz force detuning is dependent on the accelerating field gradient and it is predictable from pulse to pulse [62]. Lorentz radiation pressure on the cavity wall is given by
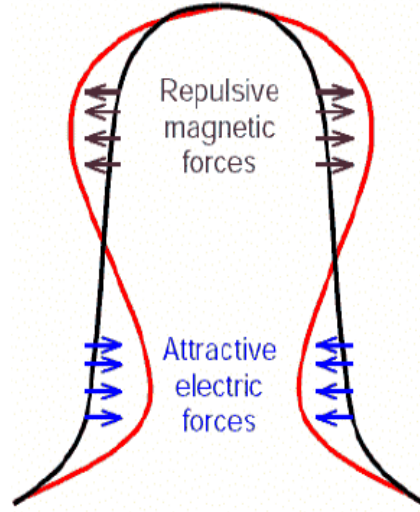
FIGURE 3.4: Electromagnetic pressure on half cell of Elliptical cavity [60].

$$P = \frac{1}{4}[\mu_o H^2 - \epsilon_o E^2]. \tag{3.5}$$

where, μ_o and ϵ_o are permeability and permitivity of free space [61]. Due to deformation in cavity cell shape frequency shift $\triangle$f can be described as

$$\triangle f = -K_L E_{ace}^2. \tag{3.6}$$

where, K_L is LFD coefficient and E_{ace} is acceleration gradient [61]. The change in amplitude and phase of the accelerating voltage due to cavity detuning is elaborated in Figure 3.5 [63]. More input power will be required to maintain the desired cavity voltage and the phase will be adjusted from the drive amplifier of the klystron.
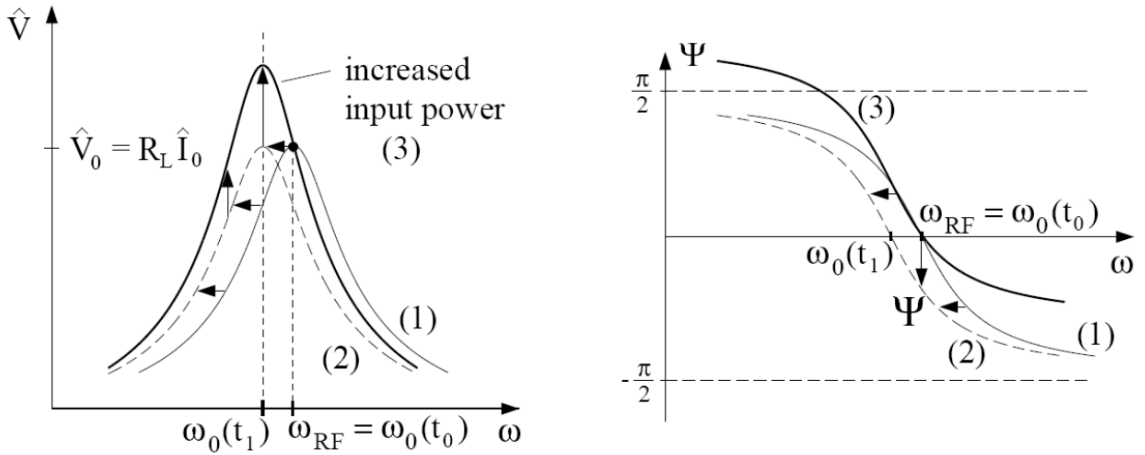
FIGURE 3.5: The cavity voltage amplitude and phase variation due to the cavity detuning [64].

For Lorentz force detuning estimation, cavity voltage V_c from the pickup coil at the end of the cavity and forward voltage V_f signals are used. The frequency detuning $\Delta\omega$ can be estimated by

$$\Delta\omega = \frac{d\phi}{dt} - \frac{\omega_{0.5}(|2V_f|)Sin(\theta - \phi)}{|V_c|}. \tag{3.7}$$

where, ϕ and θ represents the phases of V_c and V_f repectively and $\omega_{0.5}$ is cavity half bandwidth [25]. But in cavity simulators, the detuning is estimated by a different mechanism, dependent on the cavity structure's mechanical resonance frequencies and accelerating voltage magnitude.

3.4.1.2 Beam Loading

The effects induced by the passage of a beam through an RF cavity are generally called beam loading. Due to beam loading multiple phenomena are induced including beam current fluctuations, pulsed beam transient, Multipacting and field emission, Excitation of higher order and other passband modes and wake fields [21]. To determine the effect of beam loading in the superconducting accelerator, it must be included in the equivalent circuit model. Beam loading and Lorentz force detuning are dominant sources of error in pulsed superconducting accelerators and are repetitive field perturbations, which can be reduced by feed forward control. In Figure 3.6, the Phasor diagram for the representation of cavity and beam voltages is shown. The phasor terms shown are:

V_a = cavity accelerating voltage.

ϕ = synchronous phase.

I_b = beam current.

V_b = beam induced cavity voltage.

V_g = generator induced cavity voltage in the absence of beam.

$V_{g,r}$ = generator induced cavity voltage at resonance in absence of beam.

$$V_a = V_g + V_b \tag{3.8}$$

Here it is evident that actual cavity accelerating voltage is much changed due to detuning and beam loading. According to the fundamental beam loading theorem, half of the beam-induced voltage is faced by the beam itself [65].
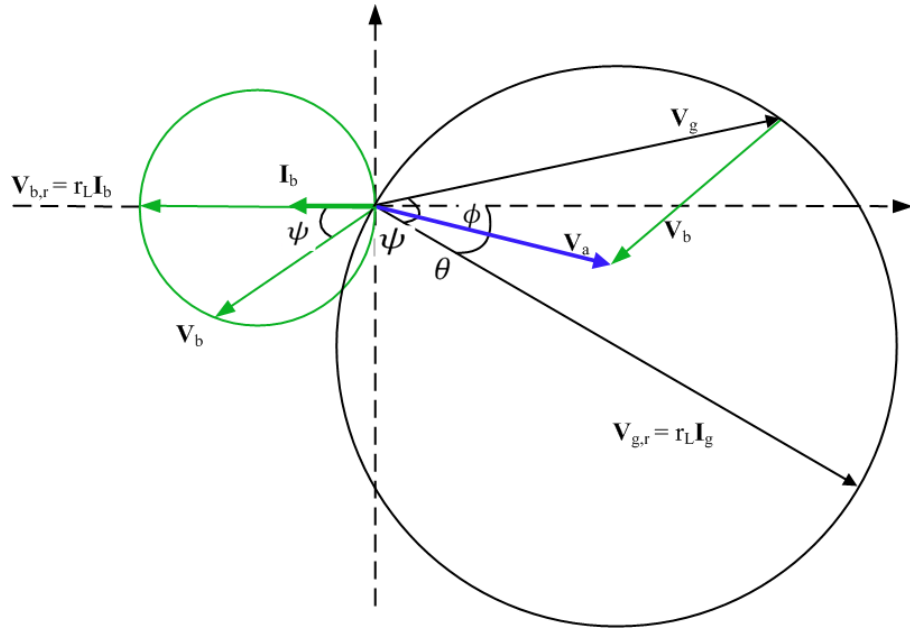
FIGURE 3.6: Phasor Diagram of Cavity and Beam Voltages in the presence of cavity detuning

3.5 Cavity Field Control Loop Architectures

Different methods have been developed to control the RF systems of particle accelerators according to Schilchers work [66]. The main types consist of the Generator Driven Resonator (GDR), Self Excited Loop (SEL), and Phase Locked Loop (PLL) [60]. These architectures are briefly explained in this section.

3.5.1 Generator Driven Resonator(GDR) Loop

In a GDR control loop, the RF field's amplitude and phase synchronize with an RF reference signal produced by a master oscillator (MO), as depicted in Figure 3.7. Consequently, the operational frequency of the RF system aligns with the frequency of the MO. Given its ability to generate stable RF fields with specific frequency, amplitude, and phase, the GDR control method is favored during beam operation in the RF system. To initiate a GDR control loop, the feedback initially remains inactive, and a feed forward signal propels the cavity to establish an RF field close to the desired operating point of the RF station. Subsequently, feedback control is engaged to achieve the desired RF field for beam acceleration.

Given that the MO dictates the RF frequency, aligning the cavity resonance frequency
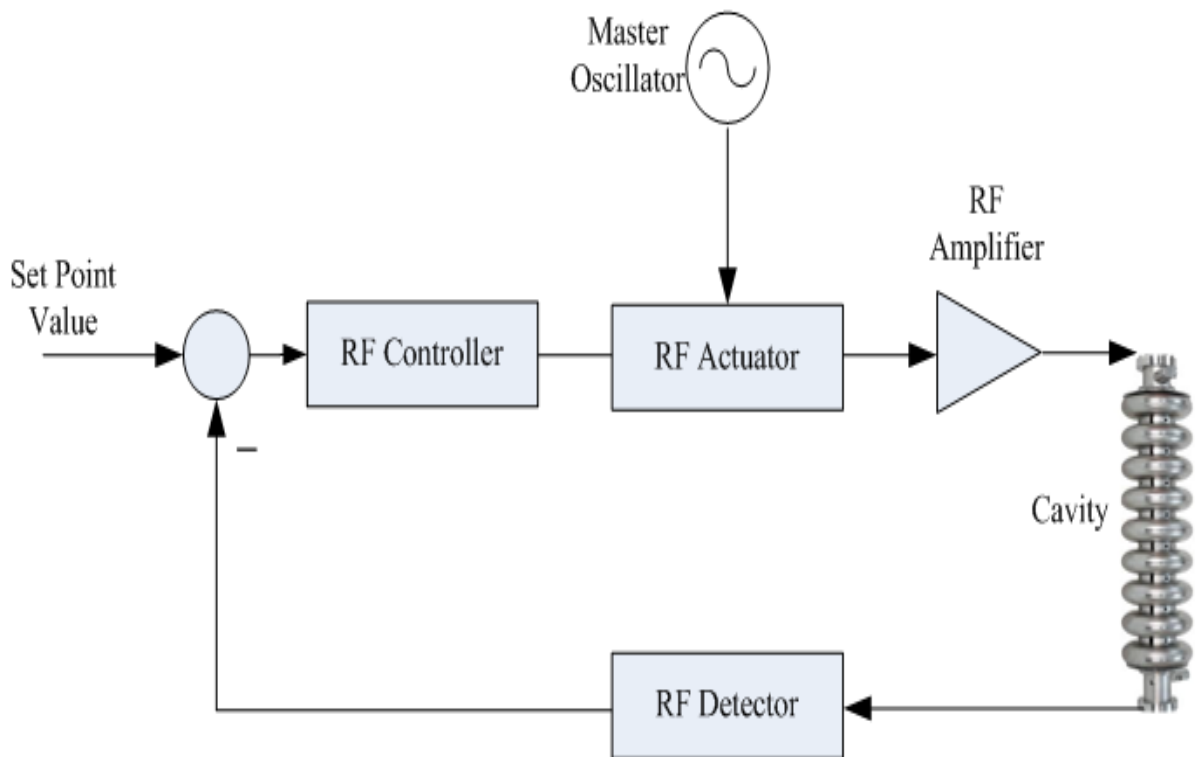
FIGURE 3.7: (a) Feedback Control block diagram for Generator Driven Resonator(GDR) Loop

with the MO frequency is crucial. However, starting up a narrow-band cavity with an unknown initial resonance frequency may pose challenges. If the cavity's detuning from the MO frequency is significant, the RF drive power will be entirely reflected, inhibiting the buildup of RF fields within the cavity. Therefore, a procedure is necessary to initially tune the narrow-band cavity when initiating a GDR control loop.

3.5.2 Phase Locked Loop (PLL)

The phase lock loop (PLL), shown in Figure 3.8, provides an alternative method to the self-excited loop. Both systems can supply RF power to the cavity by keeping the RF frequency in synchronization with the cavity's resonance frequency. In the PLL setup, the relative phase between the cavity's input and output is regulated by adjusting the output frequency of a voltage-controlled oscillator (VCO). Using a loop phase shifter, the frequency of the VCO is fine-tuned to resonate the cavity. A PLL controller ensures that the output of the phase detector matches a specific target. In cavity test stands, PLLs are often used to test or condition superconducting cavities with very narrow bandwidths [68]. The goal is to couple enough RF power to the cavity for high-power

RF testing or conditioning. Since the cavity is often detuned or the tuner isn't ready to adjust it, the PLL steps in to tweak the RF operating frequency, ensuring it follows the cavity's resonance frequency. This ensures smooth and effective testing or conditioning processes.
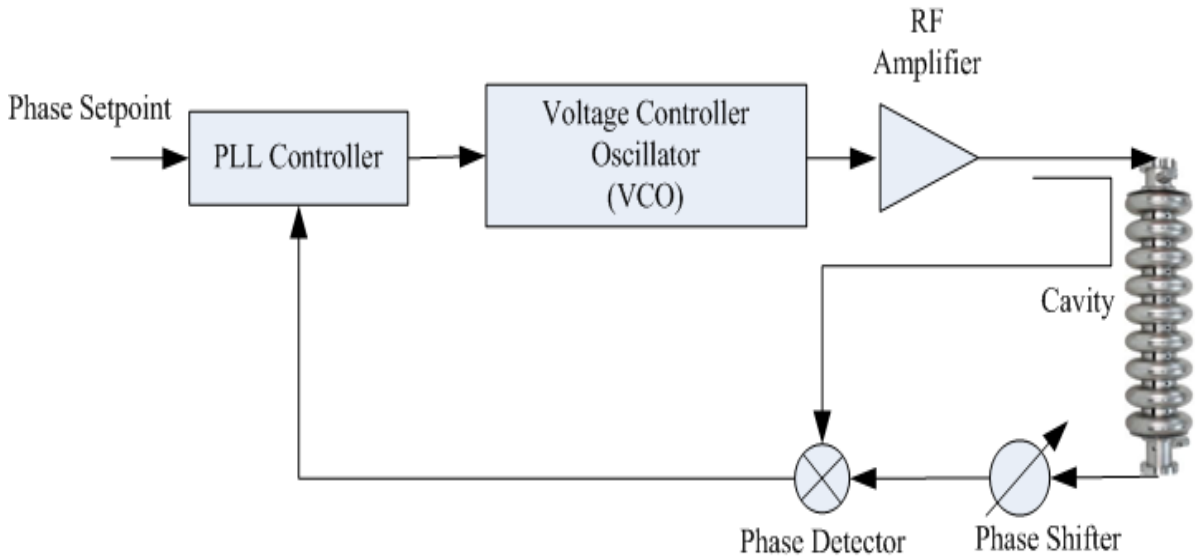
FIGURE 3.8: (a) Feedback Control block diagram for Phase Lock Loop (PLL)

3.5.3 Self-Excited Loop

In self-excited loop (SEL) configuration, there's no need for a master oscillator. Instead, the cavity probe signal directly stimulates the high-power RF amplifier [67]. A typical SEL setup is presented in Figure 3.9.

The SEL operates like a positive feedback loop. If the loop's phase lines up with multiples of 2π and the loop gain exceeds one at a specific frequency, the SEL triggers an exponential increase in cavity voltage. This allows the SEL's operational frequency to be adjusted using the phase shifter. To ensure that the RF amplifier doesn't produce excessive power, a limiter is necessary.

3.6 RF Cavity Model

RF cavity is a metallic structure that encloses the electromagnetic field in such a pattern that supports the acceleration of charged particles introduced in the cavity. The
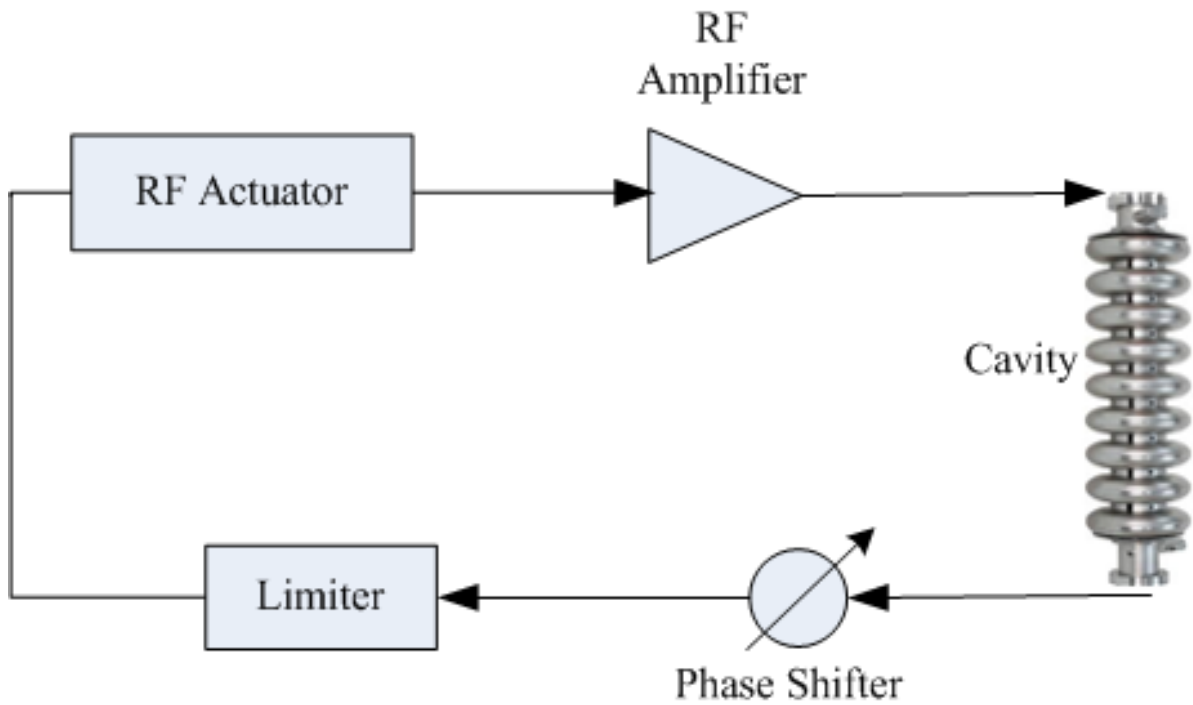
FIGURE 3.9: (a) Feedback Control block diagram for Self Excited Loop (SEL)

patterns of the electric and magnetic fields inside the cavity are classified as modes. Superconducting cavities can be a single cell or multiple cells, depending upon the accelerator design and applications.

In a single-cell cavity, TM_{010} mode exhibits the electric field in a longitudinal direction along the axis of the cavity, and the magnetic field loops in a transverse plane to the axis of the cavity.

In a multi-cell cavity, there are various passband modes, out of which, π-mode is used for beam acceleration. π-mode is a passband mode, in which the electric field in each consecutive cell is 180 degrees apart and longitudinal in direction.

3.6.1   Single Cell Cavity Model

In a single-cell radio frequency cavity transverse magnetic mode TM_{010} is used for particle acceleration. In TM_{010} mode, the magnetic field is in a transverses plane to the direction of propagation of wave, and the electric field is along the propagation direction in this case axial direction in an elliptical cell cavity. A single-cell elliptical cavity is simulated in CST microwave studio and TM010 mode electric and magnetic fields are shown in Figure 3.10. The axial electrical field is responsible for charged

particle acceleration. The parallel RLC circuit cavity model of a single cell coupled to
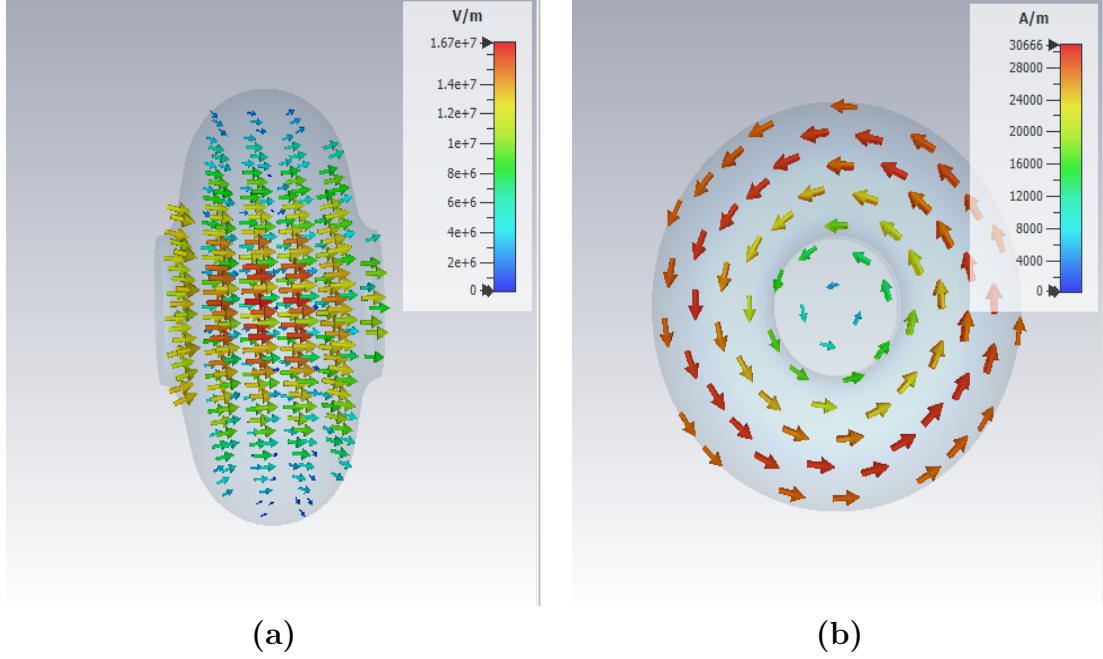
FIGURE 3.10: RF Fields Simulation of Single Cell Elliptical Cavity in CST Microwave Studio (a) Electric Field along the axis(b) Magnetic Field in Transverse Plane

an RF power source via an input coupler is the basis for analyzing multicell cavities and their properties [66]. The RF source and beam are modeled as current sources with phasor representations i_{rf} and i_b respectively. The input coupler is modeled as a transformer with a ratio $1 : n$ and Z_0 is the characteristic impedance of the transmission line. The equivalent circuit by transferring the RF source to the cavity side is shown in Figure 3.11. The phasor $\mathbf{i}_{rf}$ is the drive current by RF power source, $\mathbf{i}_b$ represents the beam current. The phasor $\mathbf{v}_c$ is the resulting cavity voltage the phasor $\mathbf{i}_c$ is overall drive current given by

$$\mathbf{i}_c = \mathbf{i}_{rf} + \mathbf{i}_b. \tag{3.9}$$

A Radiofrequency accelerator cavity is usually characterized by its loaded quality factor (Q_L), cavity resonance frequency and normalized shunt impedance (r/Q). The mathematical relations between RLC circuit parameters and typical cavity parameters are given in Table 3.1. where,

$W = $ The stored electromagnetic energy in the cavity.

$P_{cav} = $ The dissipated RF power in the cavity wall.

$P_{ext} = $ The emitted RF power out of the cavity through the input coupler.
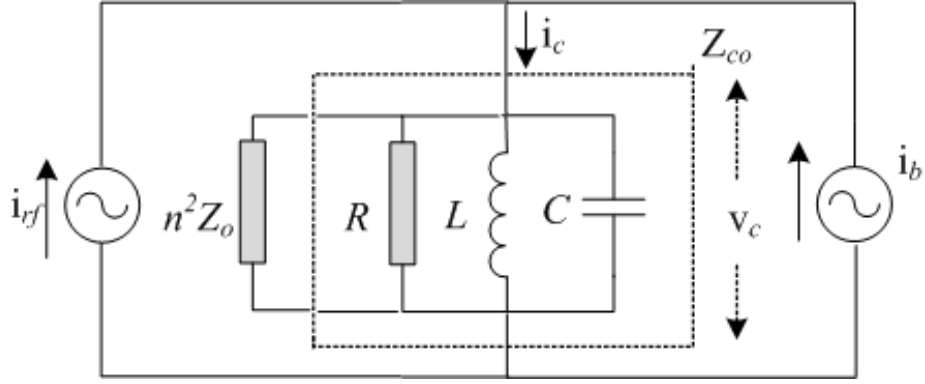
FIGURE 3.11: Accelerator cavity circuit model with beam current, input coupler, and RF source

Since the RLC circuit model has complex impedances, this model can be analyzed by using phasor Laplace transform [60]. The complex impedances of inductor and capacitor in the RLC model and their transformation from s to $\hat{s}$ domain are presented in Table 3.2. where the carrier frequency is equal to the input radio frequency. The phasor transfer function of the cavity $G_c(\hat{s})$ can be written as

$$
\begin{aligned}
\mathbf{G}_c(\hat{s}) &= \frac{\mathbf{V}_c(\hat{s})}{\mathbf{I}_c(\hat{s})} \\
&= \frac{(\hat{s} + jw_c)/C}{(\hat{s} + jw_c)^2 + (\hat{s} + jw_c)/(R_L C) + 1/(LC)}.
\end{aligned}
\tag{3.10}
$$

Where, $\mathbf{I}_c(\hat{s})$ and $\mathbf{V}_c(\hat{s})$ are phasor Laplace Transform of the $\mathbf{i}_c(input)$ and the $\mathbf{v}_c(output)$. Using the relations in Table 3.1, the transfer function with cavity parameters can be represented as

$$
\mathbf{G}_c(\hat{s}) = \frac{2w_{1/2}R_L(\hat{s} + jw_c)}{(\hat{s} + jw_c)^2 + 2w_{1/2}(\hat{s} + jw_c)^2 + w_o^2}.
\tag{3.11}
$$

The two poles of $\mathbf{G}_c(\hat{s})$ are:

$$
\hat{s}_{p1,2} = -w_{1/2} \pm j\sqrt{w_o^2 - w_{1/2}^2} - jw_c.
\tag{3.12}
$$

Since the cavity resonance frequency is typically much higher than the cavity half bandwidth ($w_{1/2} \ll w_o$), the poles can be approximated to

$$
\hat{s}_{p1} \approx -w_{1/2} + j(w_o - w_c).
\tag{3.13}
$$

TABLE 3.1: Cavity Circuit Model Parameters Relations with Typical Cavity Parameters [60].

Cavity Parameter	Symbol	Relation with circuit parameter
Resonance Frequency	w_o	$w_o = 1/\sqrt{LC}$
Unloaded Quality Factor	Q_o	$Q_o = \frac{w_o W}{P_{cav}} = w_o RC = \frac{R}{Lw_o}$
External Quality Factor	Q_{ext}	$Q_o = \frac{w_o W}{P_{ext}} = w_o n^2 Z_o C$
Coupling Factor	β	$\beta = \frac{P_{ext}}{P_{cav}} = \frac{Q_o}{Q_{ext}} = \frac{R}{n^2 Z_o}$
Loaded Quality Factor	Q_L	$Q_L = \frac{Q_o}{1+\beta}$
Normalized Shunt Impedance	r/Q	$R = \frac{1}{2}(r/Q)Q_o$
Loaded Resistance	R_L	$R_L = \frac{R}{1+\beta} = \frac{1}{2}(r/Q)Q_L$
Half Bandwidth	$w_{1/2}$	$w1/2 = \frac{w_o}{2Q_L}$

TABLE 3.2: s and $\hat{s}$ Domain Representation of Impedance in Cavity Circuit Model.

Element	Symbol	Impedance in s Domain	Impedance in $\hat{s}$ Domain
Resistance	R	R	R
Capacitance	C	$1/sC$	$1/(\hat{s} + jw_c)C$
Inductance	L	sL	$(\hat{s} + jw_c)C$

$$\hat{s}_{p2} \approx -w_{1/2} - j(w_o + w_c). \tag{3.14}$$

$$\triangle w = w_o - w_c. \tag{3.15}$$

and assume $\triangle w << w_o$, so that Equation (3.11) can be simplified as

$$\mathbf{G}_c(\hat{s}) = \frac{w_{1/2}R_L}{\hat{s} + w_{1/2} - j \triangle w}. \tag{3.16}$$

In the $\hat{s}$-domain with the assumptions stated before, the second-order cavity model is reduced to a first-order model. Due to a single complex pole, the frequency response is asymmetric at positive and negative frequencies. In time domain the cavity input and output phasors relation can be derived and given as:

$$\dot{\mathbf{v}}_c + (w_{1/2} - j \triangle w)\mathbf{v}_c = w_{1/2}\mathbf{R}_L\mathbf{i}_c. \tag{3.17}$$
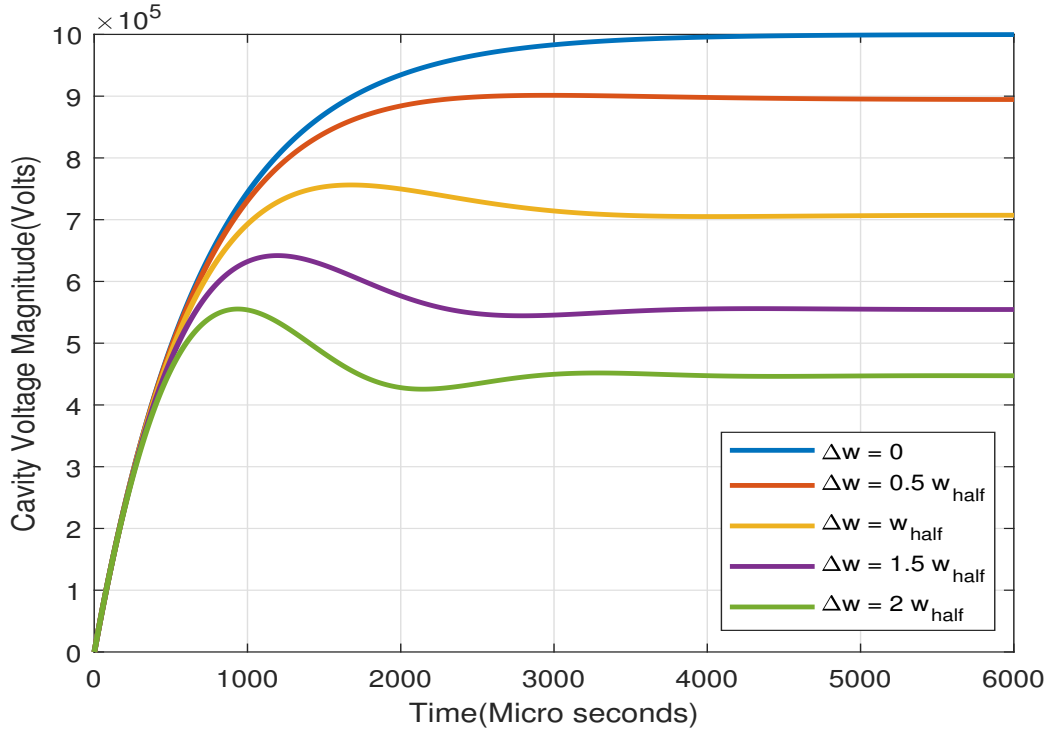
FIGURE 3.12: Cavity voltage magnitude to a step input for single cell cavity model

The step response of the system modeled in Equation 3.17 for different cavity detuning values are simulated in MATLAB and the amplitude and phase responses are plotted in Figure 3.12 and Figure 3.13 respectively. The significant effect of cavity detuning on cavity voltage magnitude and phase are apparent in the results. By representing input and output in I and Q components the above model can be represented as a MIMO model in which the real and imaginary parts are coupled to each other. The Coupling of these components are shown by the step response of the system for different cavity detuning values in Figure 3.14. The MIMO system state-space equation given as:

$$
\begin{bmatrix} \dot{v}_{CI} \\ \dot{v}_{CQ} \end{bmatrix} = \begin{bmatrix} -w_{1/2} & -\triangle w \\ \triangle w & -w_{1/2} \end{bmatrix} \begin{bmatrix} v_{CI} \\ v_{CQ} \end{bmatrix} + w_{1/2} R_L \begin{bmatrix} i_{CI} \\ i_{CQ} \end{bmatrix}.
$$
(3.18)

Where $\mathbf{v}_C = v_{CI} + jv_{CQ}$ and $\mathbf{i}_C = i_{CI} + ji_{CQ}$. The state-space equation matches well with the modern control theory. It is suitable for implementing discrete algorithms derived from the cavity model. The above state space model can be represented in following form,u_I and u_Q as real and imaginary control inputs to the cavity plant transfer function.

$$\begin{bmatrix} \dot{v}_{CI} \\ \dot{v}_{CQ} \end{bmatrix} = \begin{bmatrix} -w_{1/2} & -\triangle w \\ \triangle w & -w_{1/2} \end{bmatrix} \begin{bmatrix} v_{CI} \\ v_{CQ} \end{bmatrix} \\ + \begin{bmatrix} w_{1/2} & 0 \\ 0 & w_{1/2} \end{bmatrix} \begin{bmatrix} u_I \\ u_Q \end{bmatrix}. \tag{3.19}$$

The cavity electrical model transfer function is given in Equation (3.20), which is further
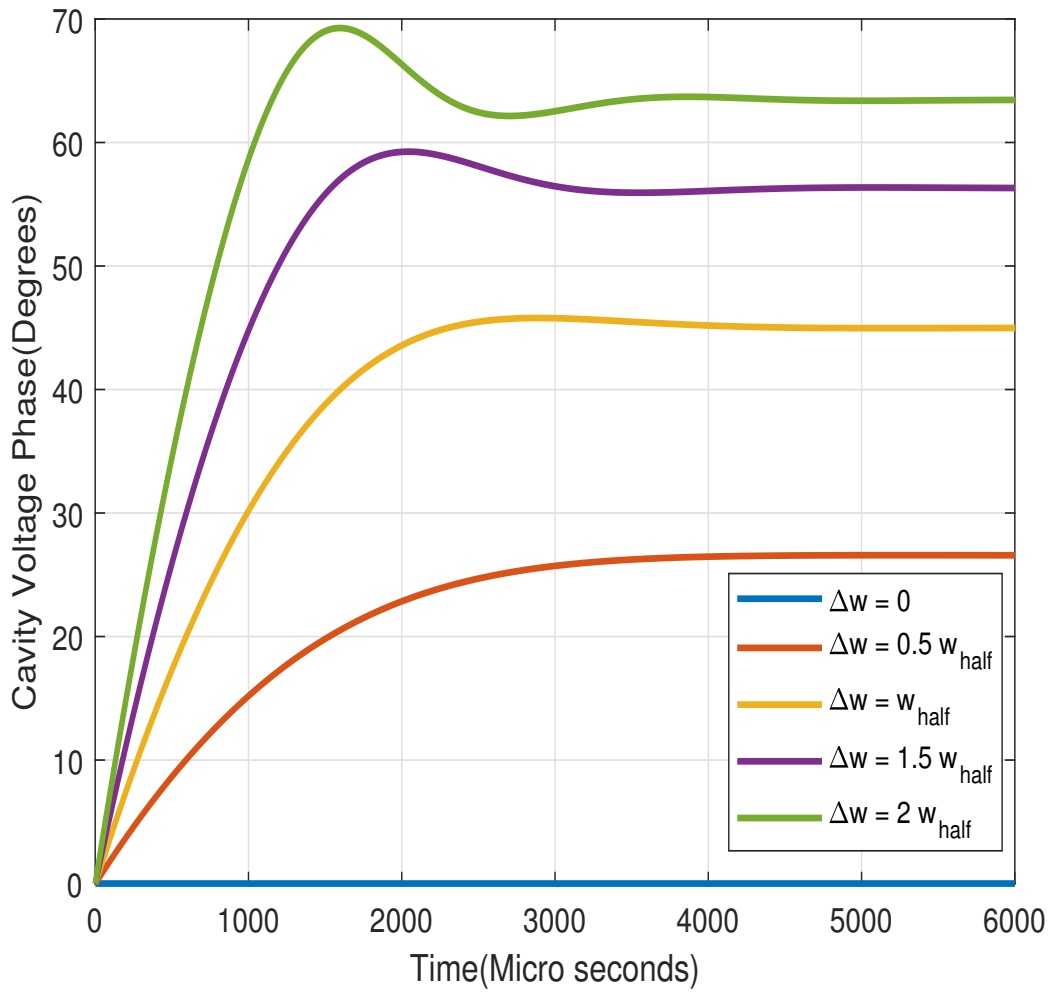
FIGURE 3.13: Cavity voltage Phase to a step input for single cell cavity model

split into two transfer functions to separate the real and imaginary parts because Matlab Simulink doesn't handle complex coefficient transfer function. The transfer function is multiplied and divided by the complex conjugate of its poles as given under:

$$\mathbf{G}_c(\hat{s}) = \frac{w_{1/2}R_L(\hat{s}+w_{1/2})}{\hat{s}^2+2w_{1/2}\hat{s}+w_{1/2}^2+\triangle w^2}. \tag{3.20}$$

The above equation can be written as

$$\mathbf{G}_c(\hat{s}) = \mathbf{G}_r(\hat{s}) + j\mathbf{G}_i(\hat{s}). \tag{3.21}$$

Where,

$$\mathbf{G}_r(\hat{s}) = \frac{w_{1/2}R_L(\hat{s} + w_{1/2})}{\hat{s} + 2w_{1/2}\hat{s} + w_{1/2}^2 + \triangle w^2}. \tag{3.22}$$

$$\mathbf{G}_i(\hat{s}) = \frac{w_{1/2} \triangle w R_L}{\hat{s} + 2w_{1/2}\hat{s} + w_{1/2}^2 + \triangle w^2}. \tag{3.23}$$

In the above equations $\mathbf{G}_r(\hat{s})$ and $\mathbf{G}_i(\hat{s})$ will give the real and imaginary part of ac-
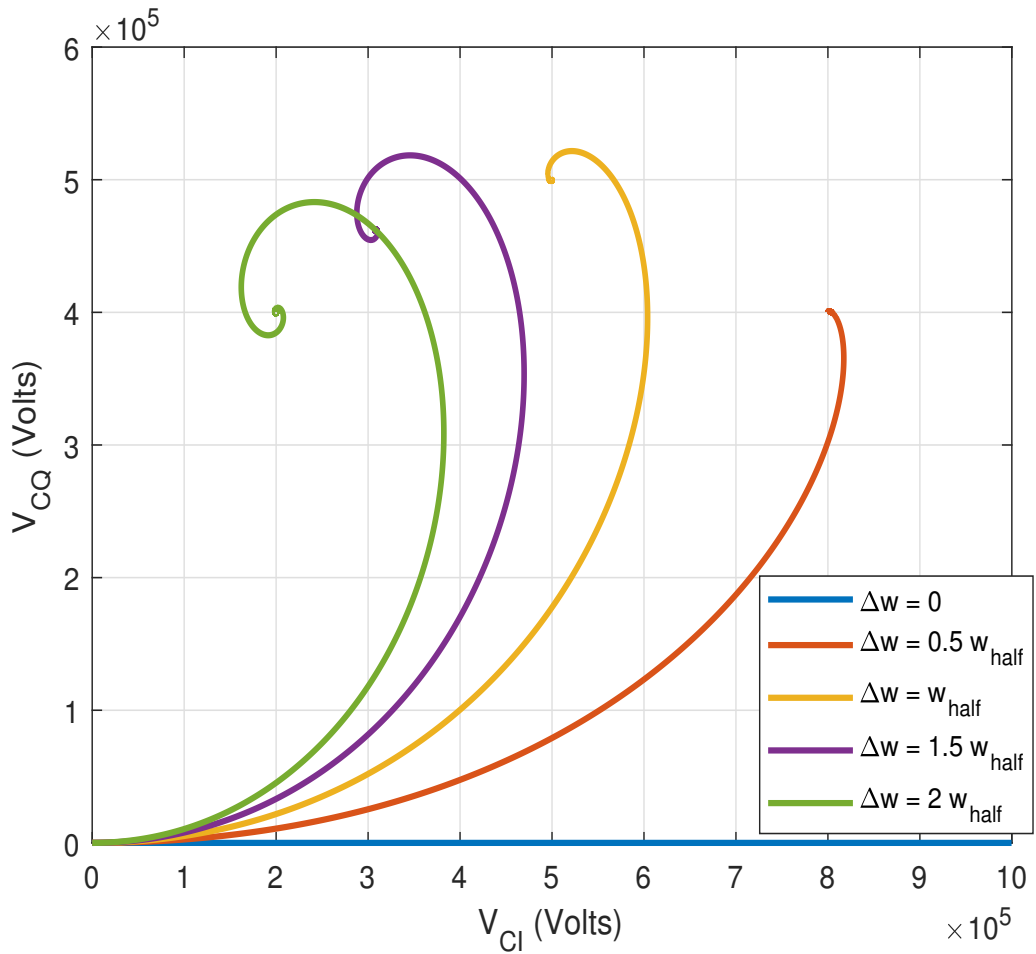
FIGURE 3.14: Cavity voltage I and Q components for a step input for single cell cavity model

celerating voltage that is I and Q values. In the transfer functions given in Equation 3.22 and Equation 3.23, $w_{1/2}$ and R_L are assumed constant and the cavity detuning $\triangle w$ is variable due to Lorentz force and microphonics. It is worth mentioning that if the cavity detuning $\triangle w$ is zero then I and Q loops in Figure 3.15 will be decoupled.
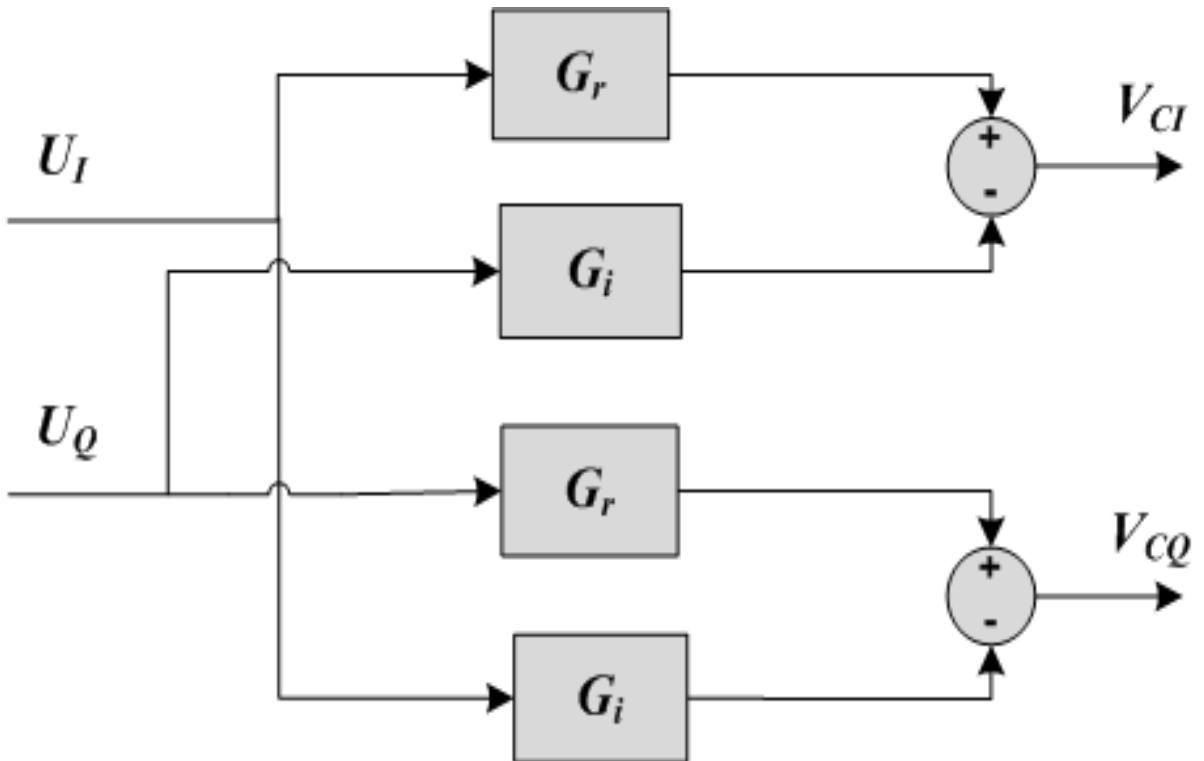
FIGURE 3.15: Cavity's Voltage I and Q components and their coupled transfer functions
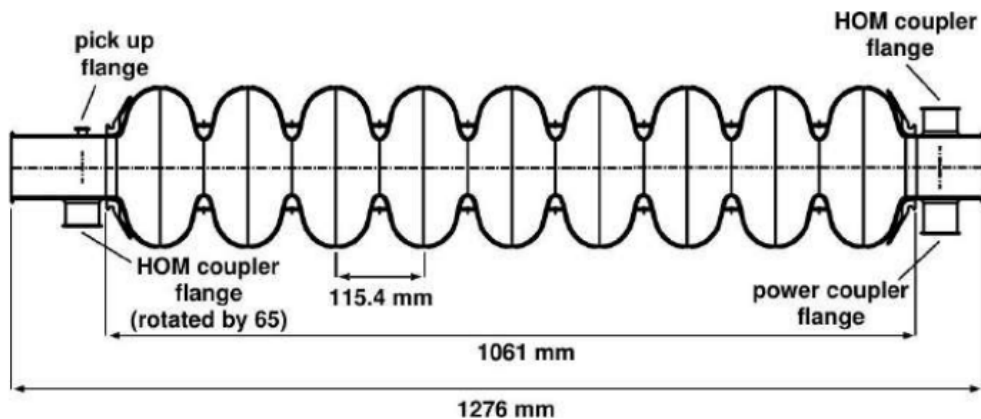
FIGURE 3.16: Side view of 9-cells TESLA Cavity [60].

3.6.2 Multicell Cavity Model

A multicell cavity is formed by interconnecting numerous single-cell cavities, with power coupled to them through a single power coupler located at the beam pipe connection of the first cell. In contrast to a single-cell cavity, the multicell design enhances efficiency, as the charged particle beam traverses each cell, progressively gaining energy. However, challenges arise with multicell cavities, such as the presence of pass band modes that are unsuitable for acceleration and the existence of higher-order modes that can impact

FIGURE 3.17: Electric field magnitude along the cavity axis in the multicell cavity for $\pi/9$ mode.

beam quality. Addressing these issues is crucial for optimizing the performance of multicell cavity-based acceleration systems.

In a multicell cavity, fundamental passband modes are classified based on the phase difference between the accelerating fields in adjacent cells. For example, in the π-mode, the accelerating fields in adjacent cells have a 180° phase difference, while in the $\pi/2$ mode, the phase difference would be 90°.In Figure 3.16, the famous 1.3GHz elliptical nine-cell TESLA cavity[69–72] is depicted, dimensions mentioned in the figure are of famous nine cells 1300MHz TESLA cavity. We have simulated this cavity in the CST microwave studio for internal field dynamics. The eigenmode simulation results of the first nine pass band modes are presented in this section. In Figure 3.17 the Electric field profile in all cells of the cavity and Electric field magnitude along the axis in $\pi/9 - mode$ are plotted. The $\pi/9 - mode$ indicates that the electric field in each successive cell is $\pi/9 - radians$ apart.

Simmilarly the results for $2\pi/9 - mode$ in Figure 3.18, $3\pi/9 - mode$ in Figure 3.19, $4\pi/9 - mode$ in Figure 3.20, $5\pi/9 - mode$ in Figure 3.21, $6\pi/9 - mode$ in Figure 3.22, $7\pi/9 - mode$ in Figure 3.23, $8\pi/9 - mode$ in Figure 3.24 and $\pi - mode$ in Figure 3.25
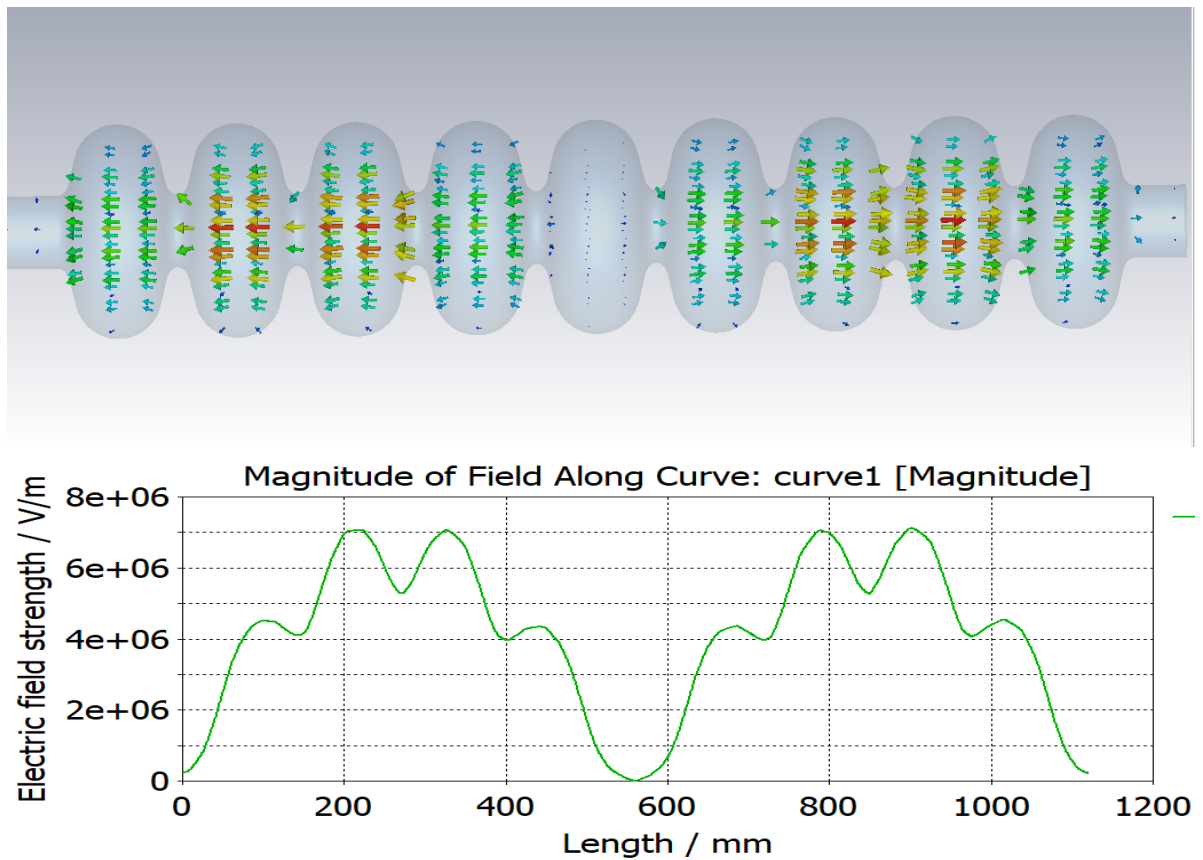
FIGURE 3.18: Electric field magnitude along the cavity axis in the multicell cavity for $2\pi/9$ mode.

are presented. we have simulated the structure with identical cell dimensions for middle and end cells, furthermore, the end cells are connected to beam pipes so the field amplitude in each cell is not flat or similar. In practice, the end cell dimensions are slightly different from the middle cells for flat field amplitudes.

The π-mode is the desired, for particle acceleration in this nine-cell cavity. For the control algorithm test, the cavity simulators developed usually consider the transfer function of two neighboring modes $\pi - mode$ and $8\pi/9 - mode$ [73].

Just as a single cell cavity is represented by a parallel RLC circuit driven by a current source, the multicell cavity is represented by multiple serial RLC circuits interconnected with one another and driven by a voltage source, as depicted in the Figure 3.26. These individual cell circuit models are interconnected through capacitors $'C'_k$, representing cell-to-cell coupling, and the end cells are connected to a beam pipe represented by capacitance $'C'_b$. The cavity parameters and the circuit parameters are related via the Table 3.1. Due to the serial RLC model, these relations are different from the single-cell parallel RLC circuit model. By Applying Kirchoff's law to each current loop the circuit
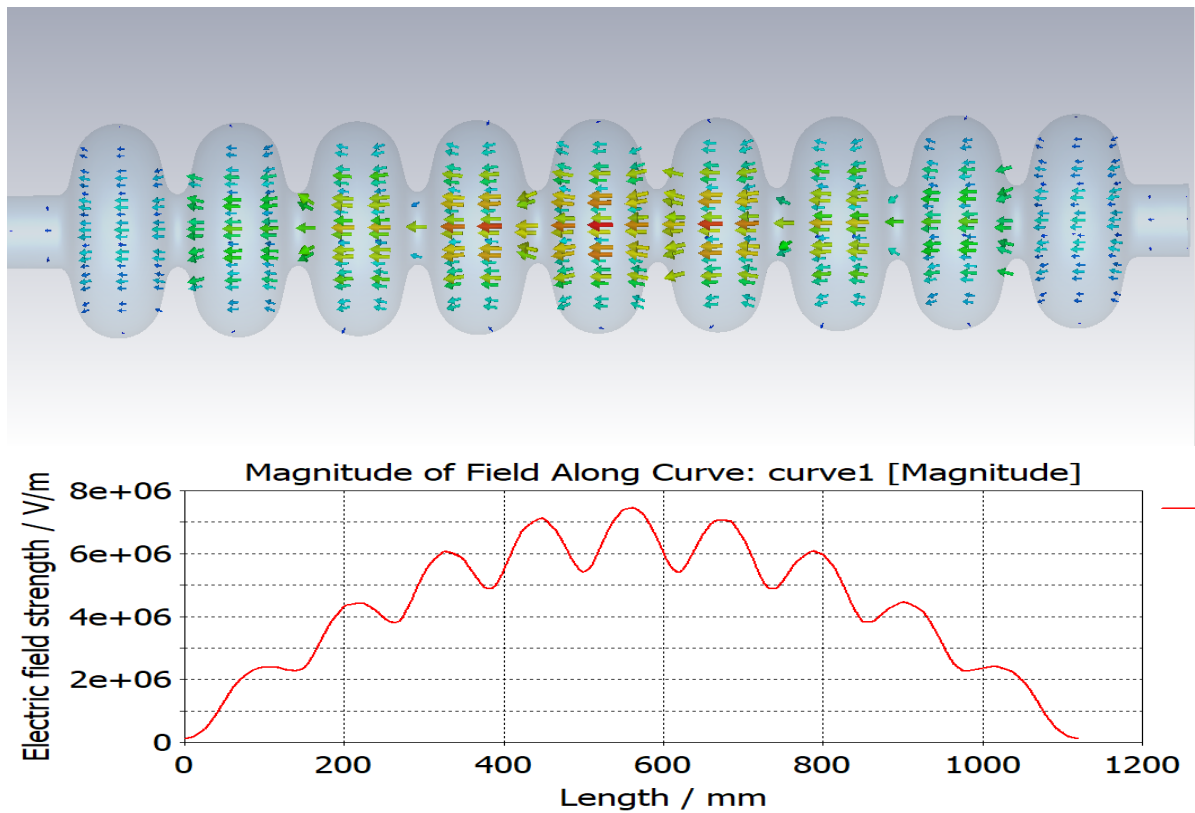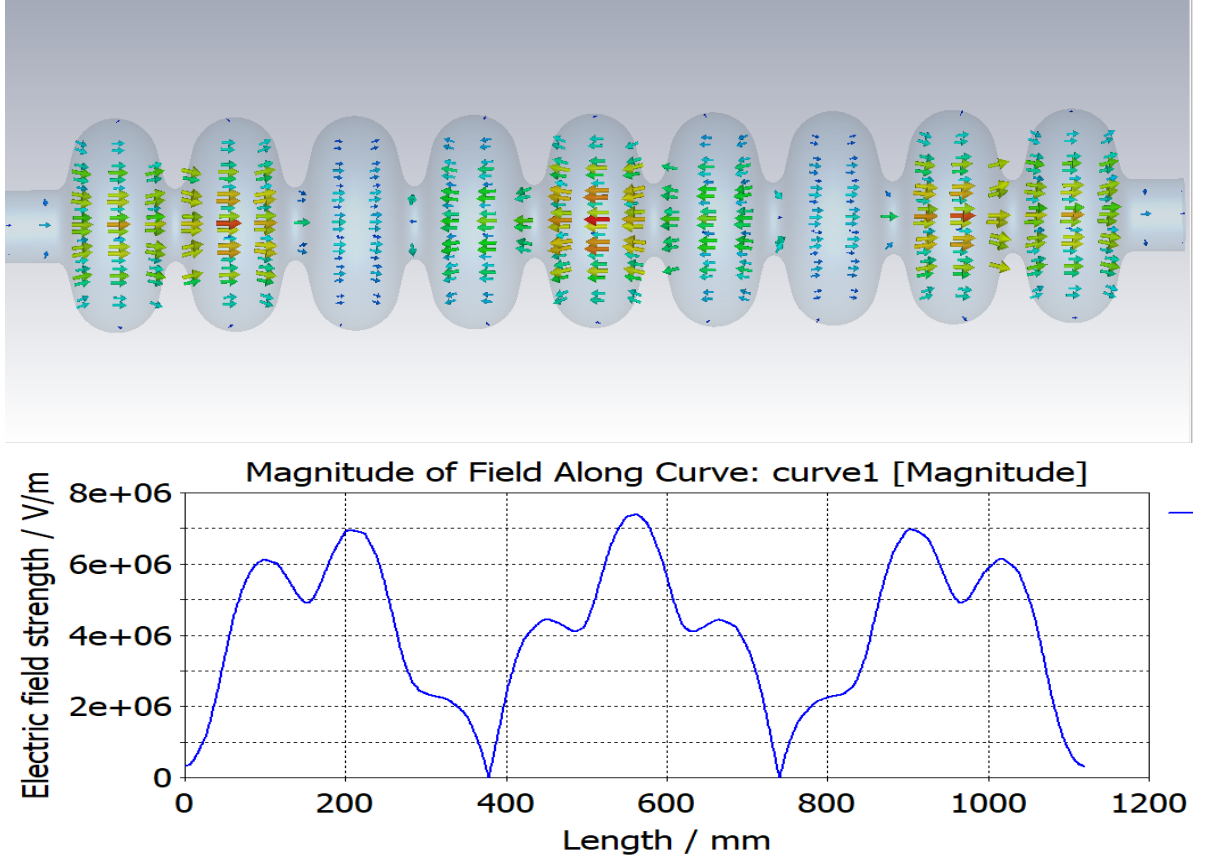
FIGURE 3.19: Electric field magnitude along the cavity axis in the multicell cavity for $3\pi/9$ mode.

equation in the s domain are

$$
\begin{aligned}
&((\beta_1 + 1)R_1 + sL_1 + \frac{1}{sC_1})I_1 + \frac{1}{sC_k}(I_1 - I_2) + \frac{1}{sc_b}I_1 = V_g, \\
&\frac{1}{sC_k}(I_n - I_{n-1}) + (R_1 + sL_1 + \frac{1}{sC_1})I_n + \frac{1}{sC_k}(I_n - I_{n+1}) = 0, \\
&\frac{1}{sC_k}(I_N - I_{N-1}) + (R_1 + sL_1 + \frac{1}{sC_1})I_N + \frac{1}{sC_b}I_N = 0.
\end{aligned} \tag{3.24}
$$

Applying relations in the table we get

$$
\begin{aligned}
&(s^2 + 2w_{1/2,L}s + w_{oe}^2)I_1 - \frac{\kappa w_{o1}^2}{2}I_2 = 2sw_{1/2,L}V_g/R_{L1}, \\
&(s^2 + 2w_{1/2,o}s + w_{om}^2)I_n - \frac{\kappa w_{o1}^2}{2}I_{n-1} - \frac{\kappa w_{o1}^2}{2}I_{n+1} = 0, 1 < n < N, \\
&(s^2 + 2w_{1/2,0}s + w_{oe}^2)I_N - \frac{\kappa w_{o1}^2}{2}I_{N-1} = 0.
\end{aligned} \tag{3.25}
$$

Figure 3.17 to Figure 3.25 illustrates the field profile of the fundamental passband modes with accelerating fields along the length of the cavity in a nine-cell configuration. From Equation 3.25 it can be concluded that the multicell cavity has multiple resonance
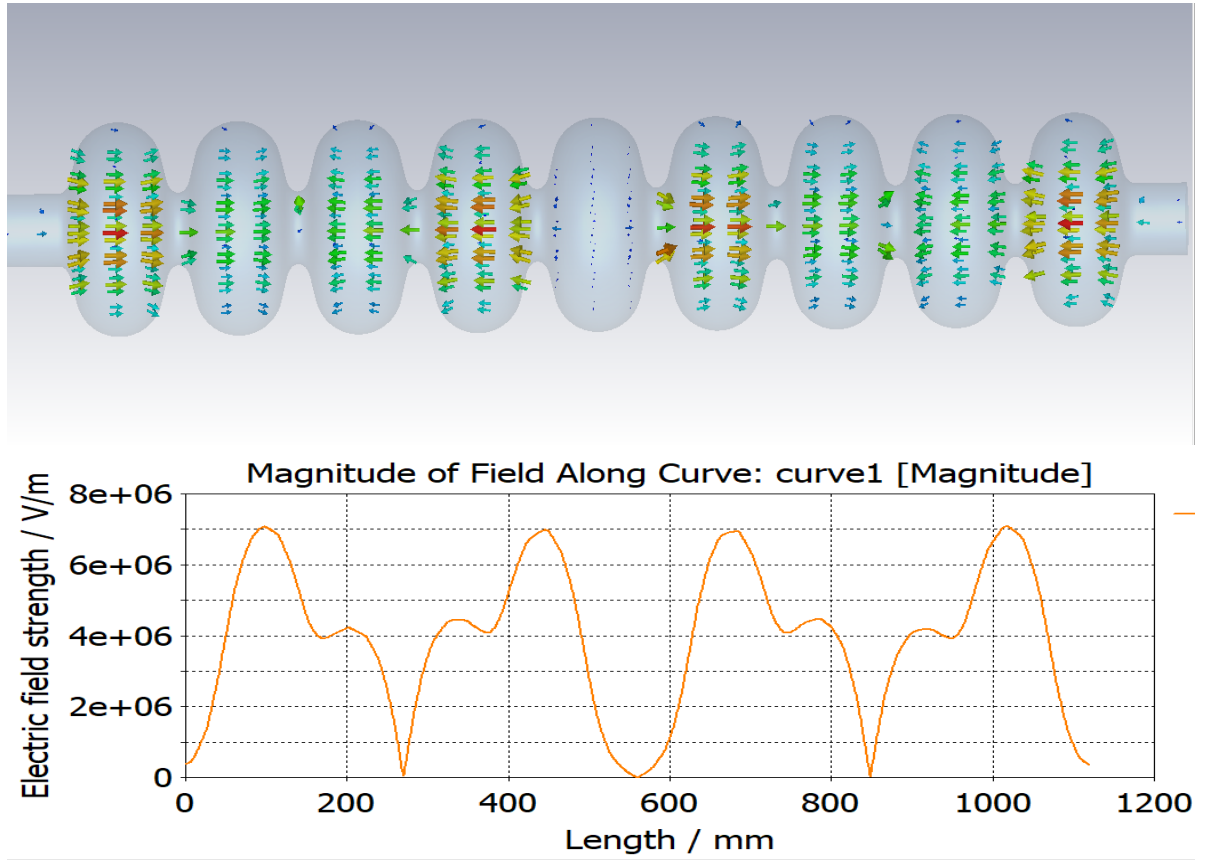
FIGURE 3.20: Electric field magnitude along the cavity axis in the multicell cavity for $4\pi/9$ mode.

frequencies around w_{oe} and w_{om}. In cavity design usually cell-to-cell coupling and cell-to-beam tube coupling are kept very small i-e $\kappa << 1$ and $\gamma << 1$. With these assumptions $w_{o1} \approx w_{oe} \approx w_{om}$. Since superconducting cavities have very small bandwidth and very high quality factor so $Q_{o1} >> 1$ and $Q_{ext} >> 1$, which correspond to $w_{1/2,L} << w_{o1}$ and $w_{1/2,0} << w_{o1}$. In Equation 3.25 by substituting $\hat{s} = s + jw_c$, roots of the polynomial $(s^2 + 2w_{1/2,L}s + w_{oe}^2)$ are around two frequencies $(w_c + w_{oe} \approx 2w_c)$ and $(w_c - w_{oe} = \Delta w_e)$. Simmilarly roots of $(s^2 + 2w_{1/2,o}s + w_{om}^2)$ are around $(w_c + w_{om} \approx 2w_c)$ and $(w_c - w_{om} = \Delta w_m)$. Since we are interested in the envelope of input and output, we neglect the higher frequencies around $2w_c$ and the simplified phasor equations in $\hat{s}$ domain for multicell cavity would be

$$(\hat{s} + w_{1/2,L} - j\Delta w_e)I_1 + j\frac{\kappa w_{o1}^2}{4w_c}I_2 = w_{1/2,L}V_g/R_L,$$

$$(\hat{s} + w_{1/2,o} - j\Delta w_m)I_n + j\frac{\kappa w_{o1}^2}{4w_c}(I_{n-1} + I_{n+1}) = 0, 1 < n < N, \qquad (3.26)$$

$$(\hat{s} + w_{1/2,o} - j\Delta w_e)I_N + j\frac{\kappa w_{o1}^2}{4w_c}I_{N-1} = 0.$$
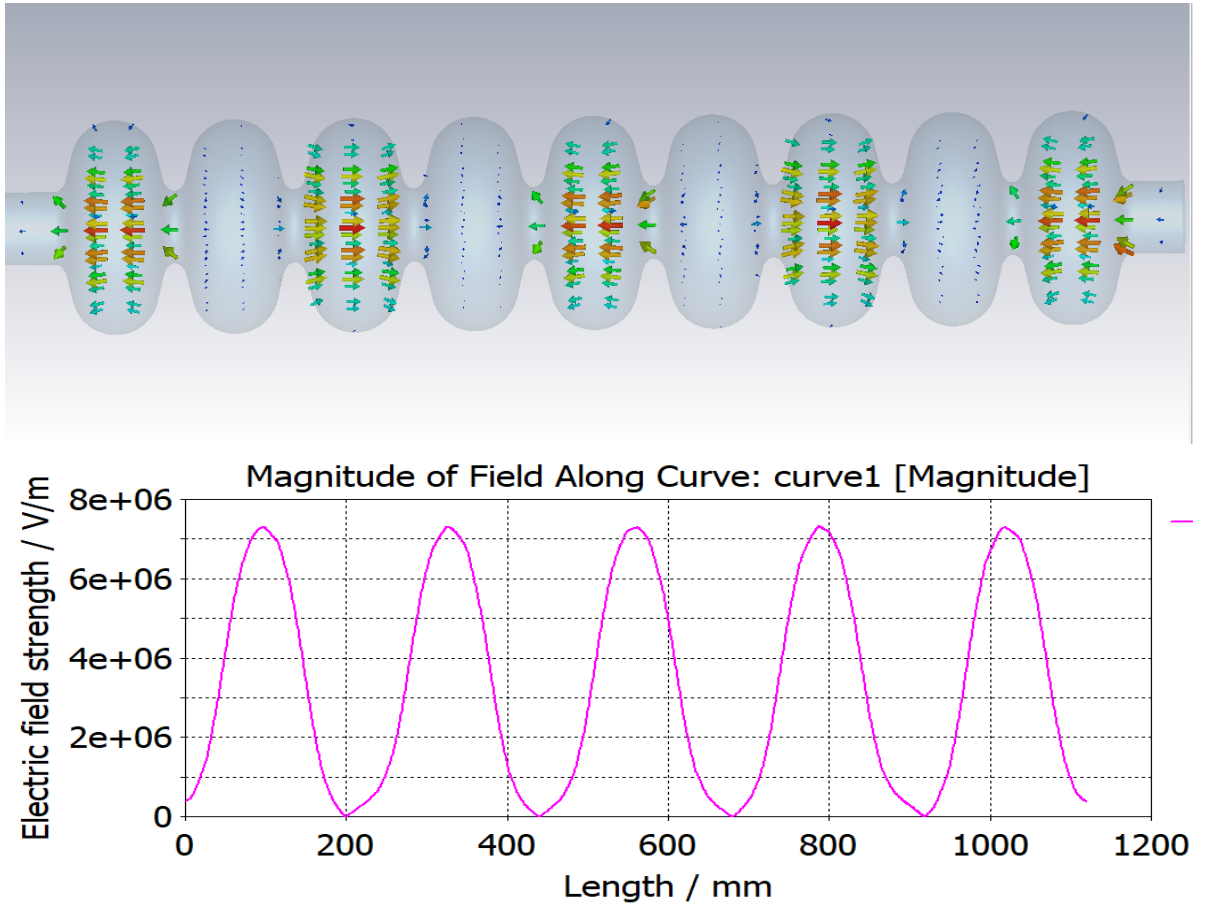
FIGURE 3.21: Electric field magnitude along the cavity axis in the multicell cavity for $5\pi/9$ mode.

where, Δw_e is the cavity detuning of end cells and Δw_m is the cavity detuning for middle cells. Using $k = -j\frac{\kappa w_{o1}^2}{4w_c}$, $a = -w_{1/2,L} + j\Delta w_e$, $b = -w_{1/2,o} + j\Delta w_m$ and $c = -w_{1/2,o} + j\Delta w_e$ in state space the Equation 3.26 can be written as

$$\dot{\mathbf{x}} = \boldsymbol{A}\mathbf{x} + \boldsymbol{B}\mathbf{u}. \tag{3.27}$$

where, $\boldsymbol{A} = \begin{bmatrix} a & k & & & & & \\ k & b & k & & & & \\ & \ddots & \ddots & \ddots & & & \\ & & k & b & k & & \\ & & & \ddots & \ddots & \ddots & \\ & & & & k & b & k \\ & & & & & k & c \end{bmatrix}$,

$B = \frac{w_{1/2,L}}{R_L}$,
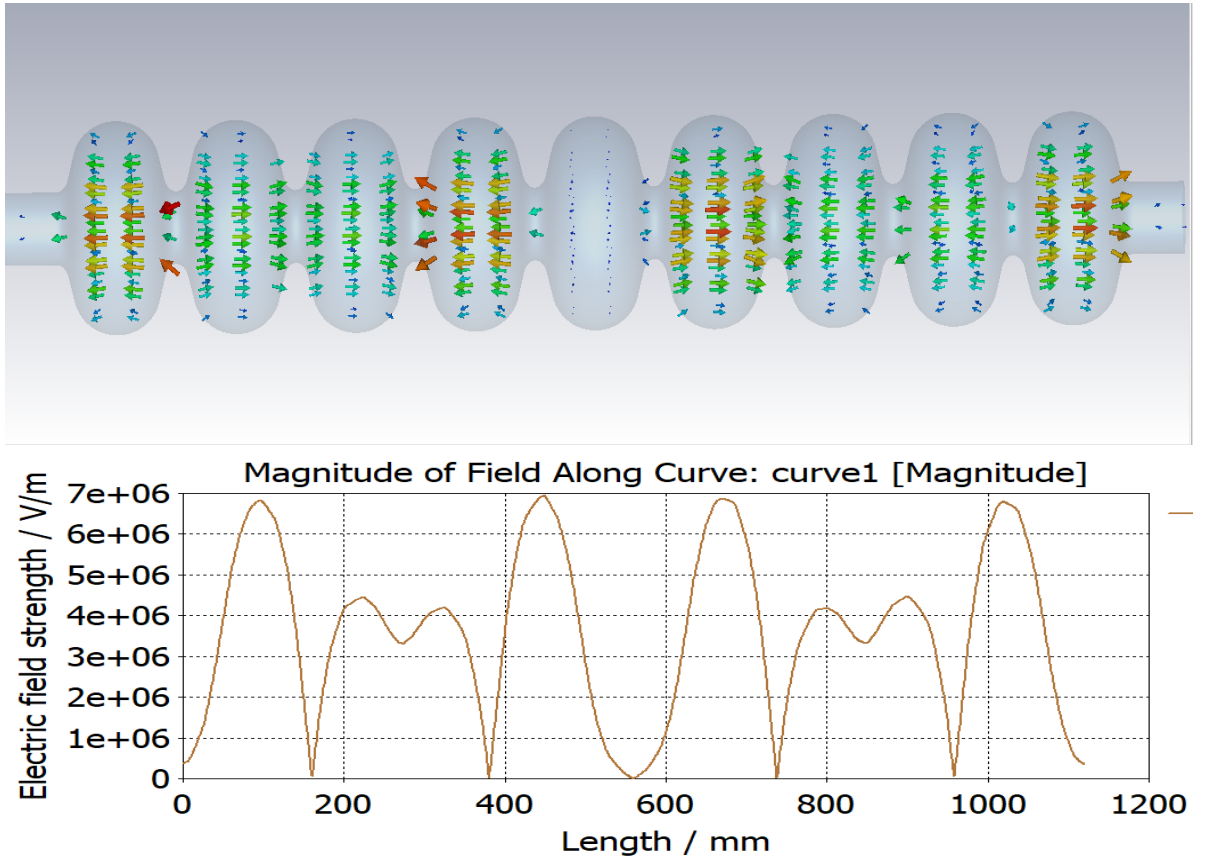
FIGURE 3.22: Electric field magnitude along the cavity axis in the multicell cavity for $6\pi/9$ mode.

$$\mathbf{x} = \begin{bmatrix} i_1 & i_2 & \ldots & i_n & \ldots & i_{N-1} & i_N \end{bmatrix}^T,$$

$$\mathbf{u} = \begin{bmatrix} v_g & 0 & \ldots & 0 & \ldots & 0 & 0 \end{bmatrix},$$

To find out the frequency response the transfer function of the cavity can be derived from the state space equation given by

$$\mathbf{G}(\hat{s}) = (\hat{s}\mathbf{I} - \mathbf{A})^{-1}\mathbf{B}. \tag{3.28}$$

The frequency response of the cavity can be computed for a particular cavity if we know the matrix A and B. As an example consider a nine cell TESLA cavity with $Q_{o1} = 10^{10}$, $w_{o1} = 2\pi \times 1275\text{MHz}$, $\kappa = 1.98\%$, $\beta_1 = 3 \times 10^4$ and $w_c = w_{o1}$. With these parameters the eigenvalues of system matrix 'A' can be computed. Each eigenvalue represents a distinct passband mode. The real part of the value would represent the half bandwidth of a particular passband mode and the imaginary part corresponds to the frequency
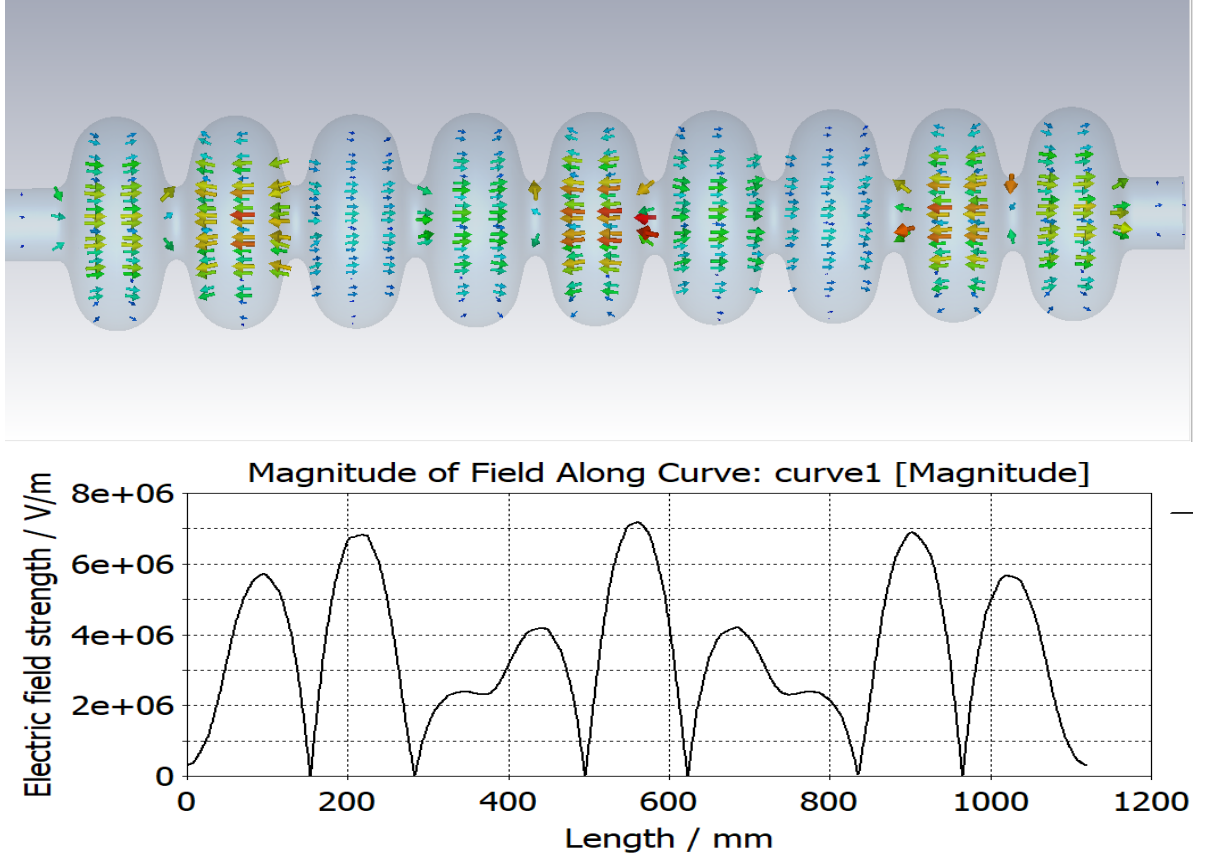
FIGURE 3.23: Electric field magnitude along the cavity axis in the multicell cavity for $7\pi/9$ mode.

offset from the carrier frequency.

The cavity transfer function from the state space equation would be

$$G = \frac{1.411e65}{\hat{s}^9 + a_1\hat{s}^8 - a_2\hat{s}^7 - a_3\hat{s}^6 + a_4\hat{s}^5 + a_5\hat{s}^4 - a_6\hat{s}^3 - a_7\hat{s}^2 + a_8\hat{s} + a_9}, \tag{3.29}$$

where,

$a_1 = 2.404e04 - 7.847e08j$,

$a_2 = 2.6e17 + 1.604e13j$,

$a_3 = 4.404e21 - 4.727e25j$,

$a_4 = 5.125e33 + 6.41e29j$,

$a_5 = 5.307e37 - 3.37e41j$,

$a_6 = 1.306e49 + 2.487e45j$,

$a_7 = 6.156e52 - 2.749e56j$,

$a_8 = 2.625e63 + 6.78e59j$,

$a_9 = 2.117e66 - 7.193e69j$.
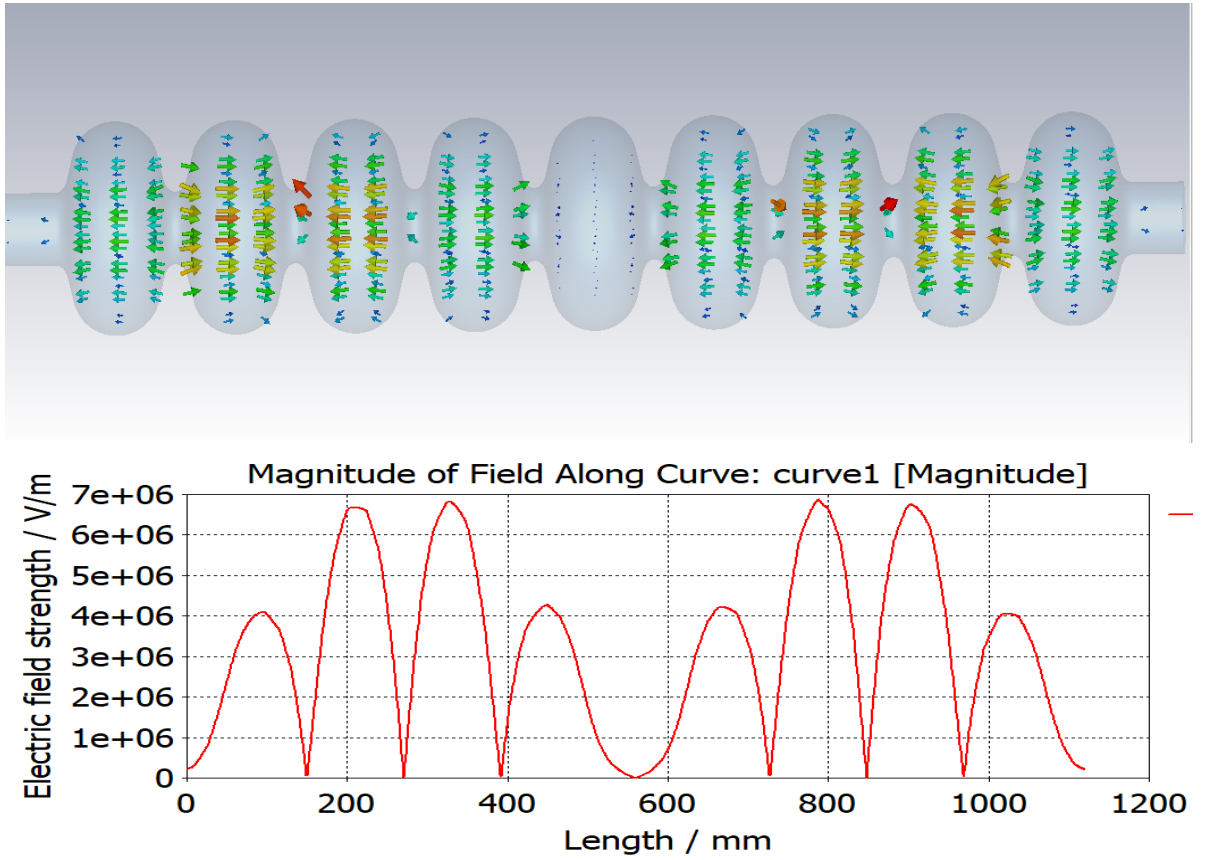
FIGURE 3.24: Electric field magnitude along the cavity axis in the multicell cavity for $8\pi/9$ mode.

In Figure 3.27 magnitude plot, each sharp peak represents a pass-band mode and each pass-band resonant mode contribute 180 degrees in the phase plot. From these results it's evident that a multi-cell cavity's phasor transfer function exhibits numerous poles, each associated with a distinct passband mode. The normalized frequency response with the lowest frequency mode having zero offset frequency is $\pi/9$-mode and the passband mode with the highest frequency is π-mode having 25MHz offset frequency. The phasor transfer function for a multi-cell cavity, encompassing all passband modes, can be expressed by extending the phasor transfer function of a single-cell cavity, as described in Equation 3.30

$$G(\hat{s}) = \sum_{i=1}^{i=N} \frac{G_i w_{1/2,i}}{\hat{s} + w_{1/2,i} - j\Delta w_i}. \tag{3.30}$$

Here the gain 'G_i' defines the relative amplitude and direction of the field in each passband mode, $w_{1/2,i}$ and Δw_i define the half bandwidth and frequency offset from the center frequency for each passband mode i-e detuning for each mode.
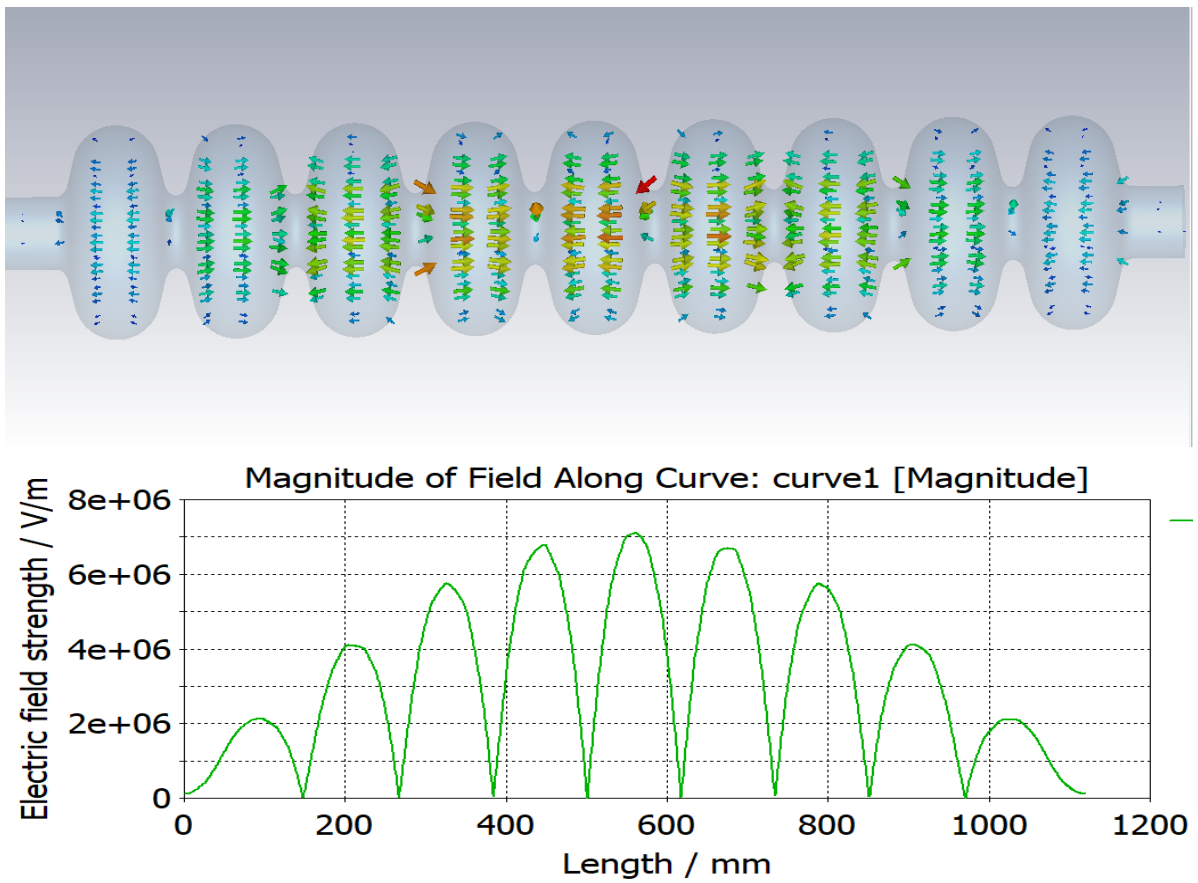
FIGURE 3.25: Electric field magnitude along the cavity axis in the multicell cavity for π mode.
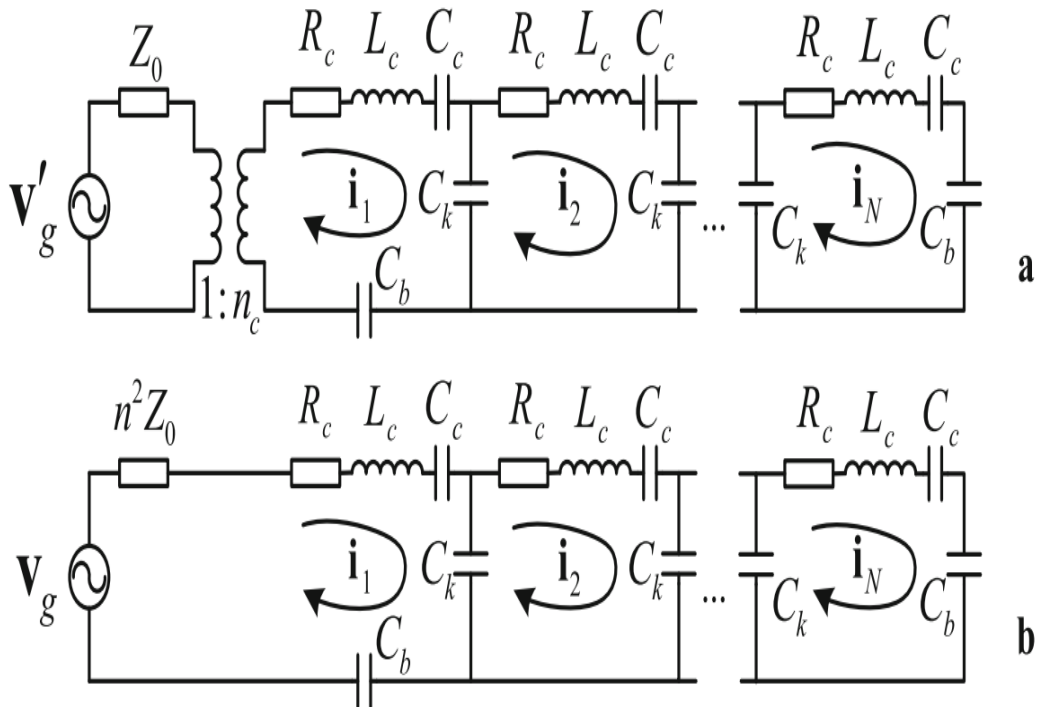
FIGURE 3.26: RLC Circuit model of a multicell cavity [60].

TABLE 3.3: Multicell Cavity Circuit Model Parameters Relations with Typical Cavity Parameters.

Cavity Parameter	Symbol	Relation with circuit parameter
Single cell Resonance Frequency	w_{o1}	$w_{o1} = 1/\sqrt{L_1 C_1}$
Single cell Unloaded Quality Factor	Q_{o1}	$Q_{o1} = \frac{w_{o1} W_1}{P_1} = \frac{w_{o1} L_1}{R_1} = \frac{1}{w_{o1} R_1 C_1}$
First cell External Quality Factor	Q_{ext1}	$Q_{ext1} = \frac{w_{o1} W_1}{P_{ext}} = \frac{w_{o1} L_1}{n_1^2 Z_o}$
First cell input Coupling Factor	β_1	$\beta_1 = \frac{P_{ext}}{P_1} = \frac{Q_{o1}}{Q_{ext1}} = \frac{n_1^2 Z_o}{R_1}$
First cell Loaded Quality Factor	Q_{L1}	$Q_{L1} = \frac{Q_{o1}}{1+\beta_1}$
First cell Loaded Resistance	R_{L1}	$R_{L1} = n_1^2 Z_o + R_1 = (1 + \beta_1)R_1$
Cell to Cell coupling factor	κ	$\kappa = \frac{2C_1}{C_k}$
Cell to beam tube coupling factor	γ	$\gamma = \frac{C_1}{C_b}$
Resonance frequency of end cells	w_{oe}	$w_{oe} = w_{oe}\sqrt{(1 + \kappa/2 + \gamma)}$
Resonance frequency of middle cells	w_{om}	$w_{om} = \sqrt{1 + \kappa}$
Half bandwidth of the cell with input coupler	$w_{1/2,L}$	$w_{1/2,L} = \frac{w_{o1}}{2Q_{L1}}$
Half bandwidth of remaining cells	$w_{1/2,o}$	$w_{1/2,o} = \frac{w_{o1}}{2Q_{o1}}$
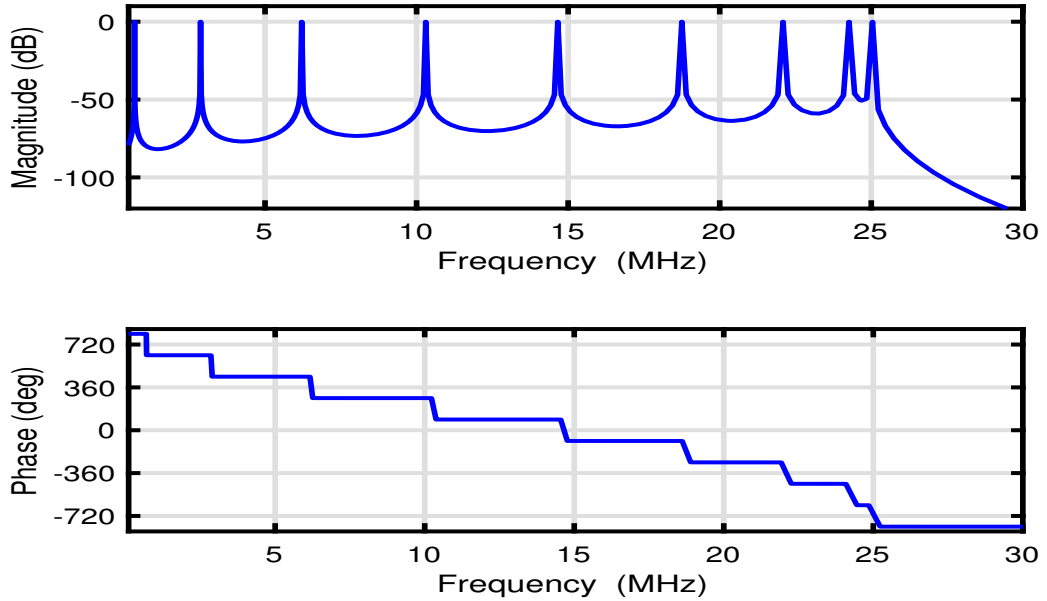
FIGURE 3.27: Frequency response of 9 cells TESLA cavity, the lowest frequency $\pi/9$-mode normalized to zero.

TABLE 3.4: Eigen values and corresponding passband modes.

Mode	Eigen Value	Mode Frquency	Mode Half Band- width
		(MHz)	(KHz)
π	$-2604.971 + 157.328j$	1300.039	2.605
$8\pi/9$	$-5120.831 + 152.469j$	1299.266	5.121
$7\pi/9$	$-4739.462 + 138.784e6j$	1297.088	4.739
$6\pi/9$	$-4038.409 + 117.818e6j$	1293.751	4.038
$5\pi/9$	$-3163.477 + 92.101e6j$	1289.658	3.163
$4\pi/9$	$-2228.733 + 64.733e6j$	1285.302	2.229
$3\pi/9$	$-1349.208 + 39.016e6j$	1281.209	1.349
$2\pi/9$	$-631.826 + 18.051e6j$	1277.872	0.632
$\pi/9$	$-163.473 + 4.3675e6j$	1275.695	0.163
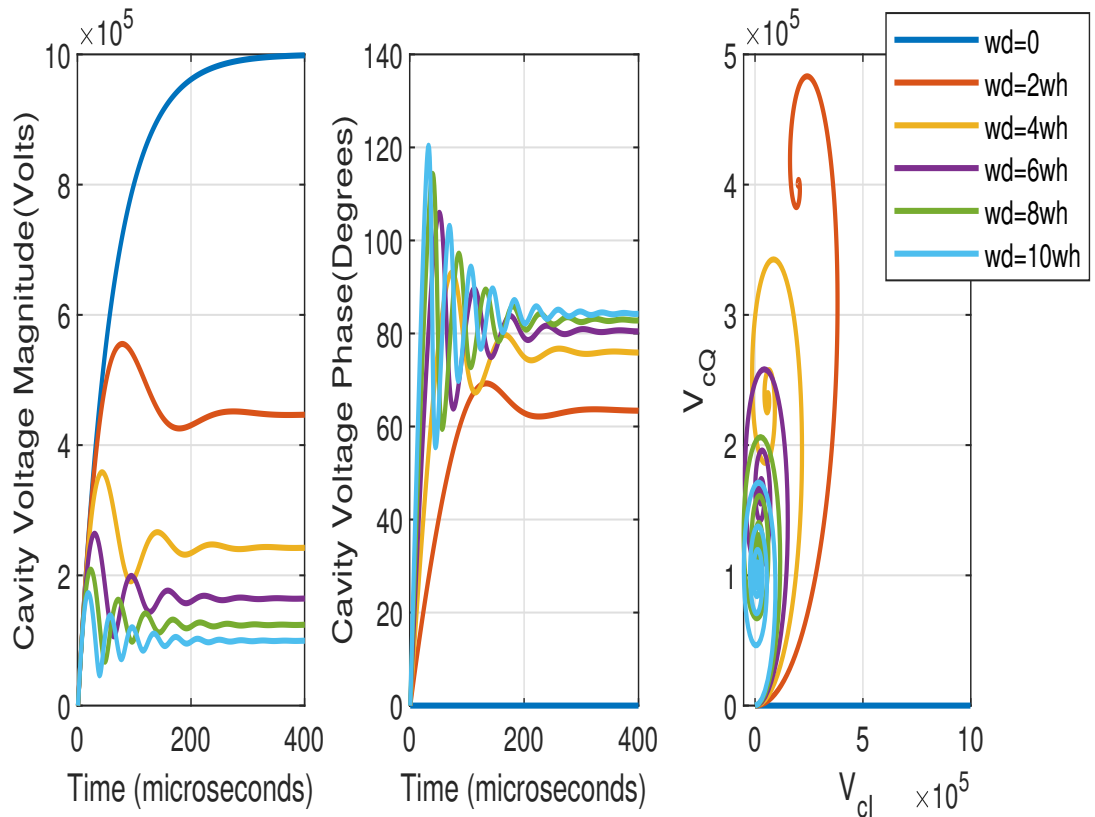
FIGURE 3.28: Step Response of πmode transfer function
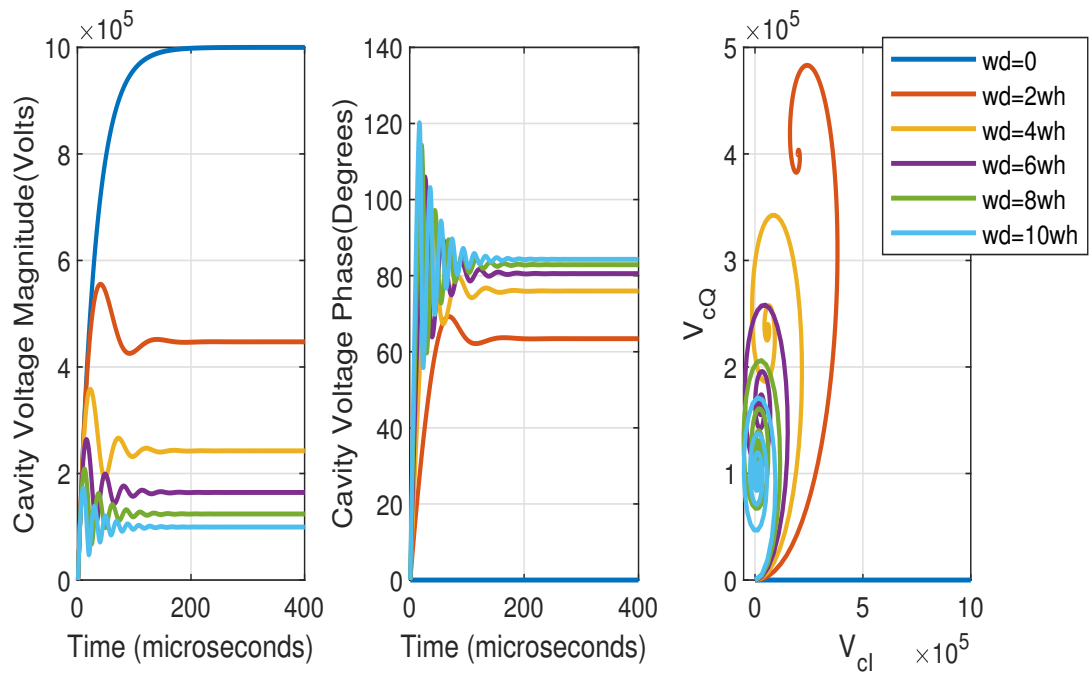
FIGURE 3.29: Step Response of $8\pi/9$mode transfer function
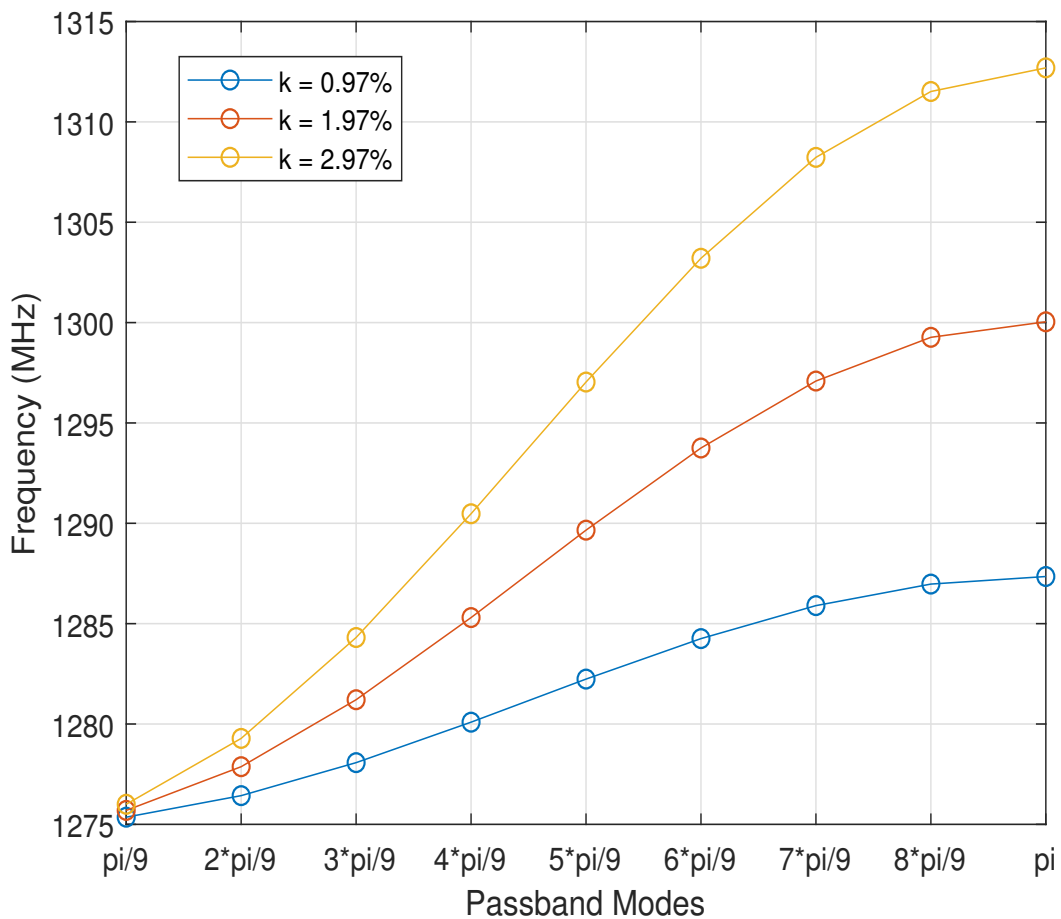
FIGURE 3.30: Disperion curves for various coupling coefficients 'k'
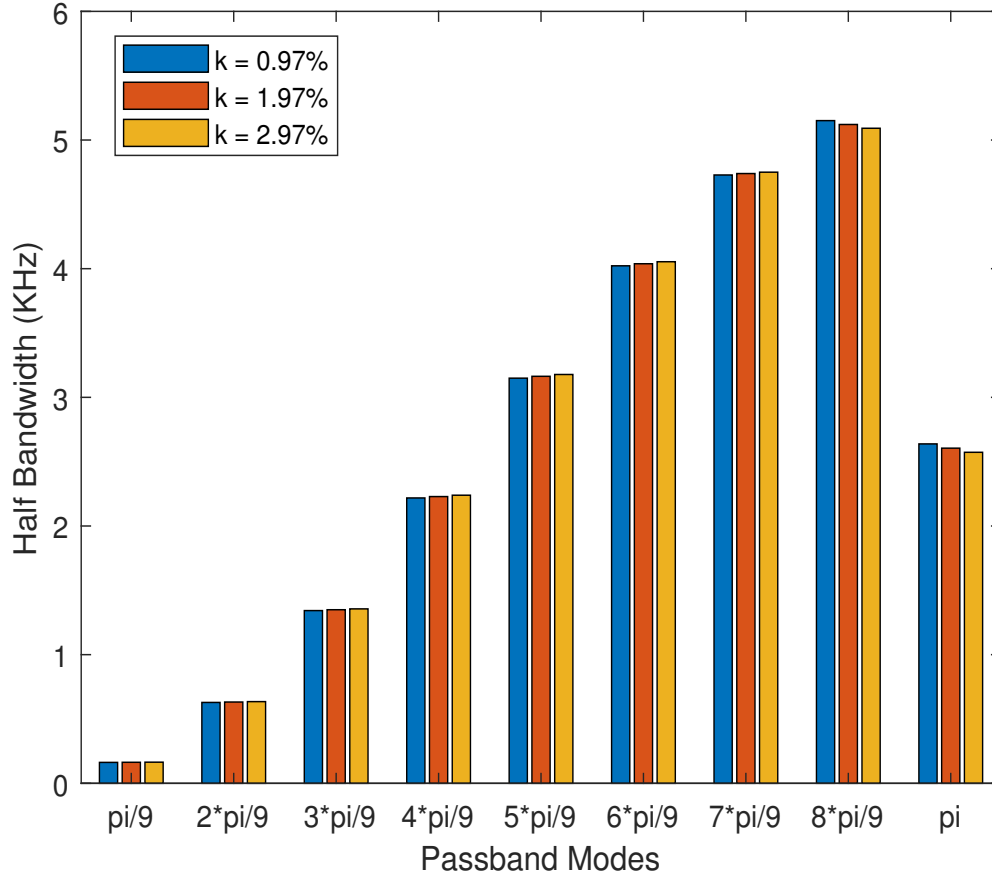
FIGURE 3.31: Half bandwidth of different modes for various coupling coefficients 'k'

In multicell cavity each passband mode will have the step response like the single cell cavity step response and would depend on each mode individual half bandwidth and the cavity detuning.

Since we power the cavity with a narrow band RF source with center frequency equal to the accelerating mode, which is π-mode in this case, so only the nearest mode i-e $8\pi/9$ is considered in field calculation. All the other modes are very far and would not contribute in cavity field. The practically used transfer function would be

$$G(\hat{s}) = \frac{G_\pi . w_{1/2,\pi}}{\hat{s} + w_{1/2,\pi} - j\Delta w_\pi} + \frac{G_{8\pi/9}.w_{1/2,8\pi/9}}{\hat{s} + w_{1/2,8\pi/9} - j\Delta w_{8\pi/9}}. \tag{3.31}$$

Step response of π-mode and $8\pi/9-$mode for different detuning values corresponding to individual modes half bandwidths are plotted in Figure 3.28 and Figure 3.29 respectively. Here individual mode isolated transfer functions are plotted, in actual if the detuning value is increased to such extent that the other mode is excited in the cavity then

that mode's transfer function would contribute in the step response. In Table 3.4 the $8\pi/9$mode has broader half bandwidth as compared to πmode that's why $8\pi/9$mode exhibit faster rise time in step response. This is very important result, as on the basis of time domain signals the cavity mode shifting in between very closely spaced modes can be detected.

The dispersion curve is the plot of passband mode frequency, plotted for three cell-to-cell coupling factor values ($k = 0.97\%, 1.97\%, 2.97\%$) in Figure 3.30. From these dispersion curves, it is evident that by increasing cell to cell coupling factor the mode spacing is increased. In the mode spectrum, the maximum mode spacing is near $\pi/2$ mode, and π.mode has very small mode spacing. In Figure 3.31, the effect of the coupling coefficient on the bandwidth of all the passband modes is elaborated. In the case of π and $\pi/9$ modes the cavities with smaller cell-to-cell coupling have smaller bandwidth as compared to larger cell-to-cell coupling.

3.7   Cavity's Electromechanical Model

Superconducting cavities have very high quality factors and lower bandwidth furthermore their walls are thin for lower cryogenic load, which is why they are very sensitive to mechanical oscillations or disturbances. As the electromagnetic field builds up inside the cavity it exerts Lorentz force on cavity walls and due to thin cavity walls, mechanical oscillations change the resonance frequency and hence the cavity voltage. This coupling between the mechanical and electrical aspects of the RF cavity is dealt with in the electromechanical model. There are several mechanical modes of a cavity structure, at different frequencies, with various oscillation patterns. We have done a modal analysis of nine cell cavity in ANSYS, resulting first six natural resonant modes presented in Figure 3.32 to 3.37. The magnitudes of oscillations are exaggerated by thousands of times to distinguish between modes of oscillation patterns. Since the end cells are fixed with beam pipe static positions, their oscillation magnitudes are minimal in nearly all modes. The lowest frequency mode or first mode is a transverse mode at 35.153Hz frequency, shown in Figure 3.32. In this mode, the maximum displacement is in the middle cells and all cells are displaced in the same transverse direction. The second mode is also a transverse mode at 89.911Hz shown in Figure 3.33, in this mode
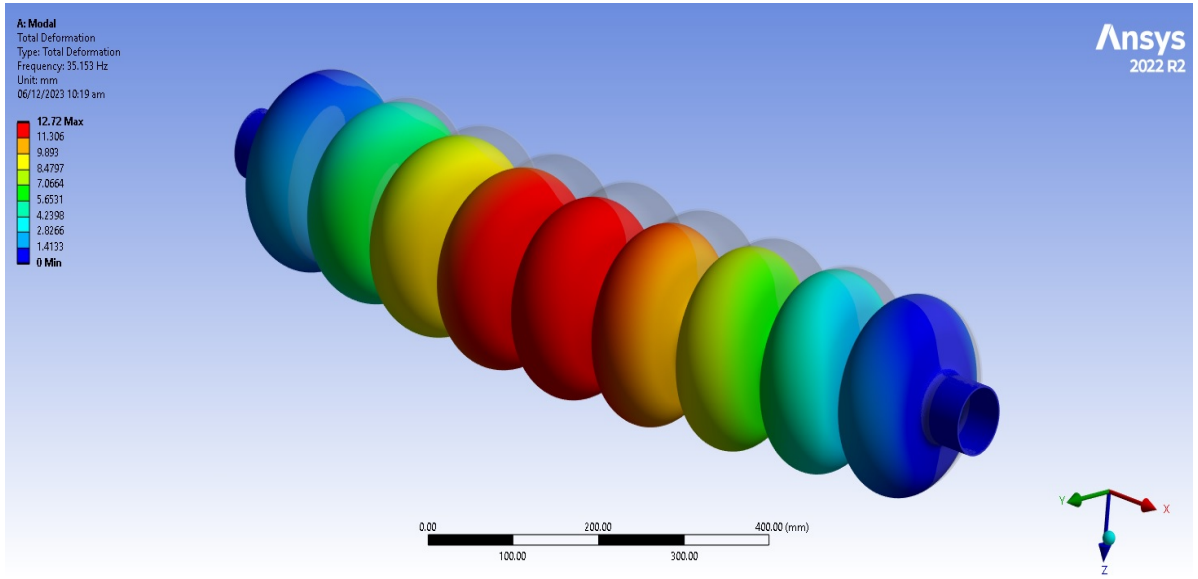
FIGURE 3.32: Mechanical mode1

the middle cells are at the node and two half waves are displaced out of phase with each other. The third mode is the longitudinal mode at 152.77Hz, shown in Figure 3.34, in this mode, the middle cells have more displacement than outer cells, it is different from the first mode as the first mode is in transverse direction and this mode is longitudinal one. The fourth mode is a mixed mode at 160.01Hz, having three half waves along the cavity axis shown in Figure 3.35 similarly in Figure 3.36 another mixed mode at 235.35Hz in which cells are tilted in transverse and longitudinal both directions. The sixth mode is a longitudinal mode at 302.85Hz shown in Figure 3.37 with two half waves and a node at the middle cells. In the simulated modal analysis, the mode frequencies are different from the results by solyak et.al.[74], because we have simulated just the cavity, not including the helium tank, coupler ports, and fitting fixtures.

The relation between cavity detuning and the cavity voltage, having m mechanical modes, is described by the cavity's mechanical model [60] given in Equation 3.32.

$$\frac{d^2 \Delta w_m}{dt^2} + \frac{w_m}{Q_m} \frac{d\Delta w_m}{dt} + w_m^2 \Delta w_m = -K_m w_m^2 |v_c|^2. \tag{3.32}$$

where, $|v_c|$ = Cavity voltage magnitude

w_m = Resonance frequency of mth mechanical mode

Δw_m = Time-varying Cavity detuning for m^{th} mechanical mode

Q_m = Quality factor of mth mechanical mode
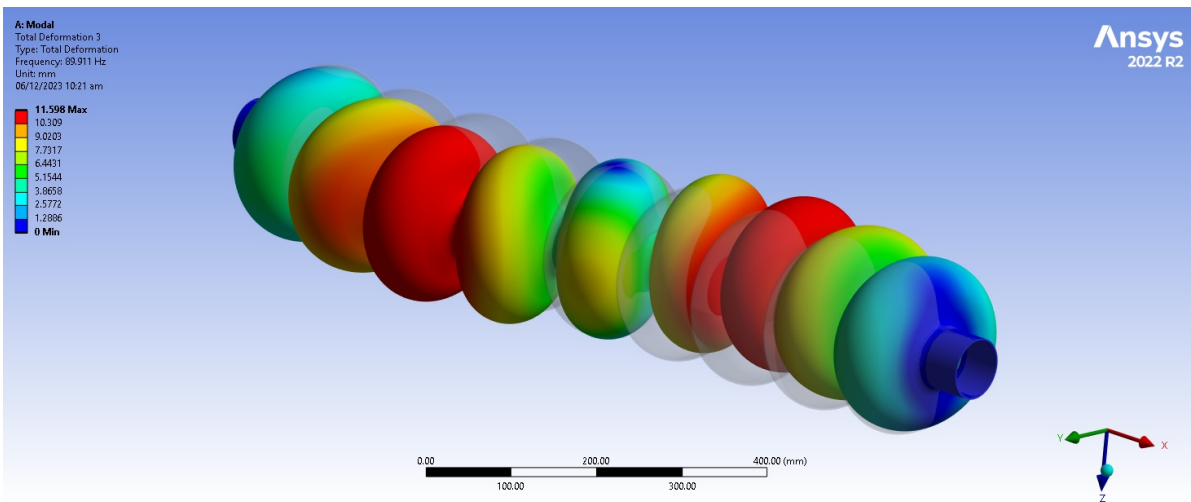
FIGURE 3.33: Mechanical mode2
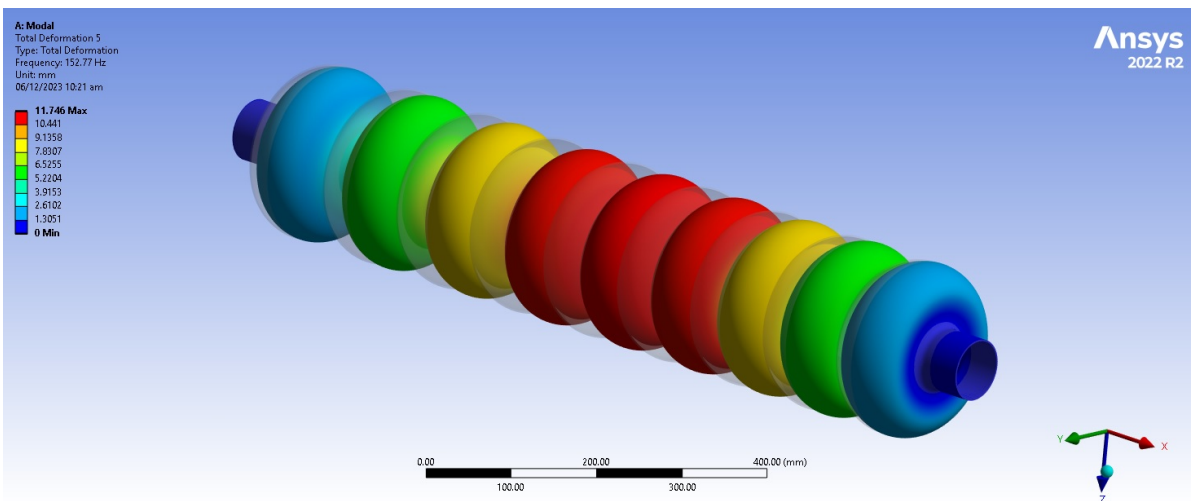
FIGURE 3.34: Mechanical mode3
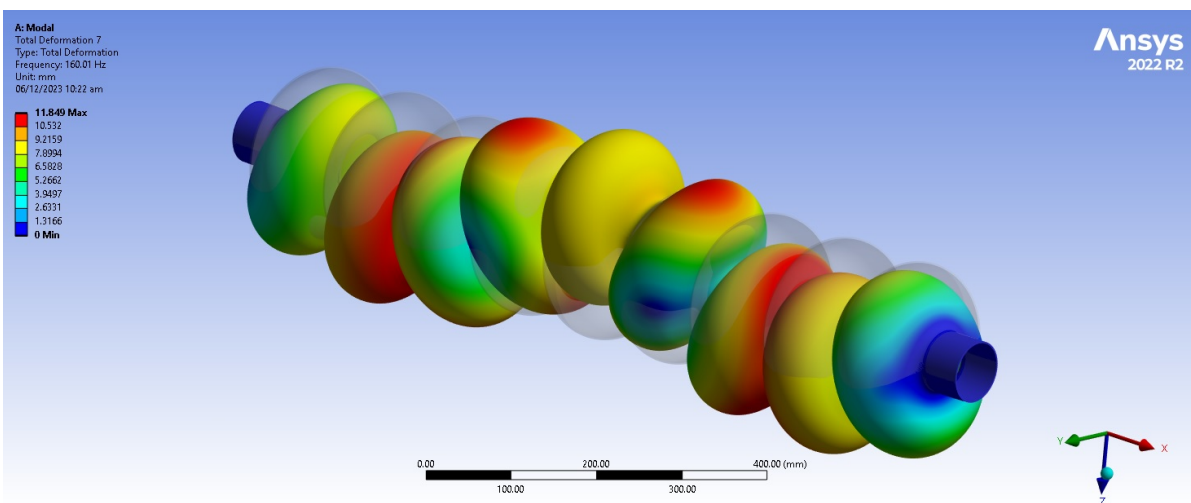
FIGURE 3.35: Mechanical mode4
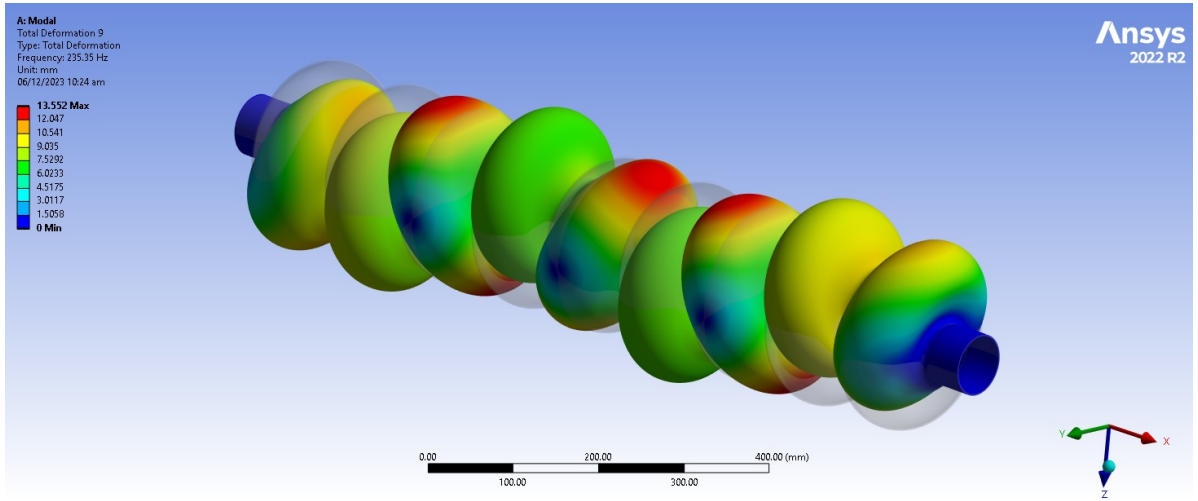
FIGURE 3.36: Mechanical mode5
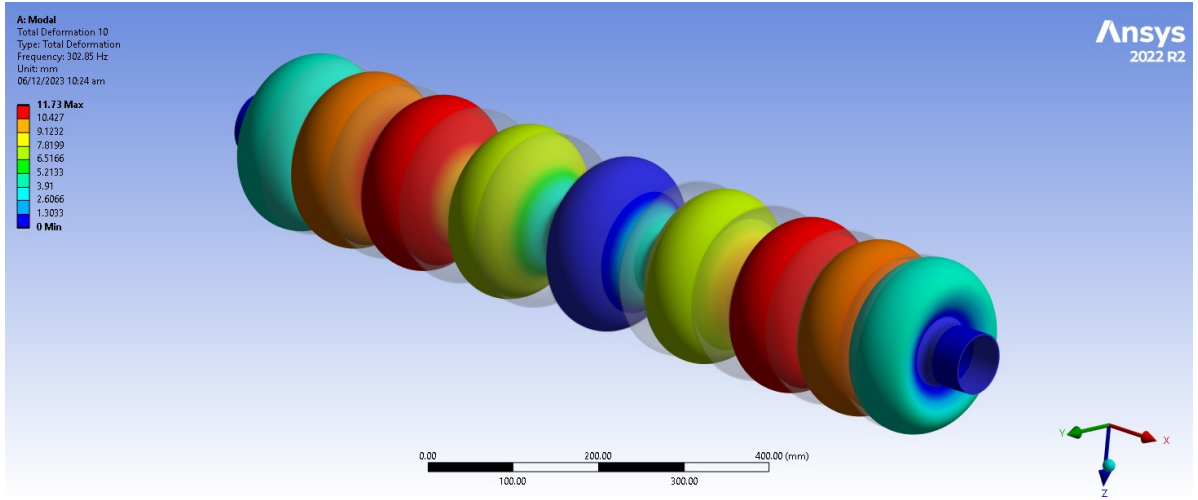
FIGURE 3.37: Mechanical mode6

K_m = Lorentz detuning constant for m^{th} mechanical mode

Equation 3.32 is a nonlinear model in which, cavity detuning is proportional to square of the the cavity voltage magnitude. At steady state $\Delta w_m = -K_m |v_c|^2$. The overall cavity detuning is given by the superposition of all the cavity detunings by each mechanical mode. For M mechanical modes the overall cavity detuning is given by

$$\Delta w(t) = \sum_{m=1}^{M} \Delta w_m(t). \tag{3.33}$$

The state space model of Equation 3.32, is given in Equation 3.34, with following states and input

$$x_1 = \Delta w,$$
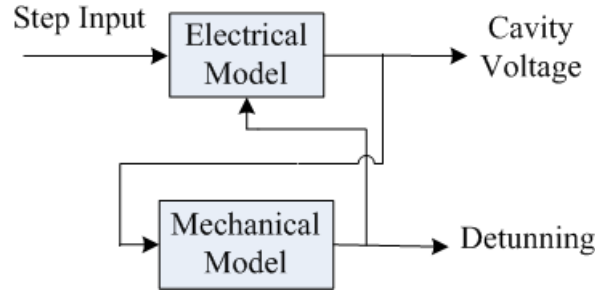
FIGURE 3.38: Electrical and mechanical models coupled with each other

$$x_2 = \Delta \dot{w},$$
$$u = |v_c|^2,$$

$$
\begin{bmatrix} \dot{x}_1 \\ \dot{x}_2 \end{bmatrix} =
\begin{bmatrix} 0 & 1 \\ -w_m^2 & \dfrac{-w_m}{Q_m} \end{bmatrix}
\begin{bmatrix} x_1 \\ x_2 \end{bmatrix}
+ \begin{bmatrix} 0 \\ -K_m w_m^2 \end{bmatrix} u. \tag{3.34}
$$

The cavity's electrical model's output i-e cavity voltage is input to the mechanical model and the cavity's mechanical model's output is cavity detuning which is proportional to the square of the cavity voltage magnitude. This coupling between the electrical and mechanical model is shown in Figure 3.38.

We utilized MATLAB Simulink to simulate both the mechanical and electromechanical aspects of the cavity model and used an adaptive PI controller due to the time-varying cavity model. To ensure the accuracy and realism of the cavity parameters, we sourced the necessary data from the TESLA technical report 2003-06 [75] given as.

Mechanical resonance frequencies = [280 340 420] Hz,

Quality factor all Mechanical resonance frequencies = 100,

Lorentz Force detuning constant = [0.4 0.3 0.2] $Hz/(V/m)^2$,

Load Resistance $R_L = 1560 M\Omega$,

Cavity Half bandwidth $B_{1/2} = 210 Hz$.

The cavity is simulated in MATLAB using the aforementioned parameters. In the step response of the cavity for 15mA input current, we observed time-varying detuning, depicted in Figure 3.39, which exhibits exponential decay. This variation in detuning

TABLE 3.5: I-loop and Q-loop, PI controller gains K_p and K_I for different cavity detuning values.

Cavity Detuning (Hz)	K_p, K_I (I-loop)	K_p, K_I (Q-loop)
1600	0.01, 27.8	0.01, 0.2
1400	0.01, 27.4	0.01, 0.1
1200	0.01, 25	0.01, 1
1000	0.01, 25	0.01, 4.05
800	0.01, 21.5	0.01, 5.2
600	0.01, 19.5	0.01, 7.5
400	0.01, 17	0.01, 9
200	0.01, 15	0.01, 11
0	0.01, 13	0.01, 13
-200	0.01, 13	0.01, 17
-400	0.01, 9	0.01, 17
-600	0.01, 7.5	0.01, 19.5
-800	0.01, 5.2	0.01, 21.5
-1000	0.01, 4.05	0.01, 25
-1200	0.01, 1	0.01, 25
-1400	0.01, 0.25	0.01, 27.5
-1600	0.01, 0.2	0.01, 30
-1800	0.01, 0.1	0.01, 30
-2000	0.01, 0.1	0.01, 31

renders the cavity model time-variant. To maintain stable cavity voltage magnitude and phase, we designed a gain-scheduling PI controller. This controller's proportional and integral coefficients are optimized for various cavity-detuning values. Subsequently, these gains are adjusted according to the cavity detuning computed by the mechanical model, which takes the cavity accelerating voltage magnitude from the output of the cavity electrical model as input. The corresponding proportional and integral gains, denoted as K_p and K_i, for the I and Q loops across various cavity detuning values, are listed in Table 3.5.
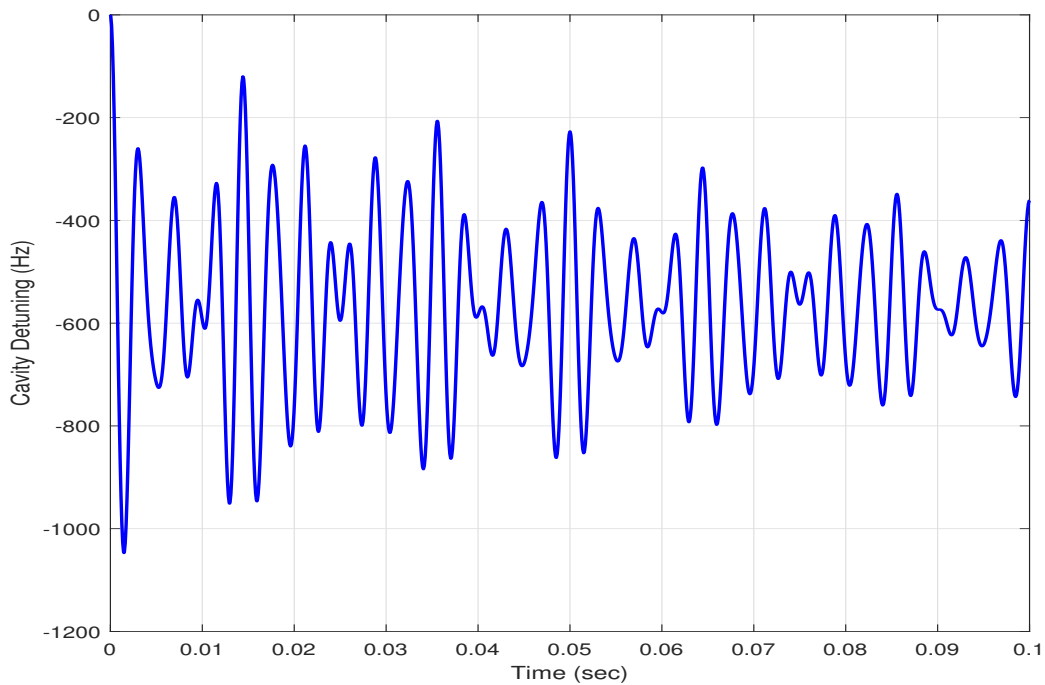
FIGURE 3.39: Time varying cavity detuning resultant of three dominant mechanical resonance frequencies, when a cavity is derived by a step input.

3.8 Low Level RF(LLRF) System

The low-level RF system is a system that measures, controls and regulates the RF field in a particle accelerator. Low-level RF systems include a Master Oscillator, Preamplifier, IQ modulator, IQ demodulator, Mixers, Filters, and RF controller. A generalized block diagram of the field control loop including the low-level RF system is presented in Figure 3.1.

The pickup antenna on the cavity picks up an RF signal which is then down-converted to an intermediate frequency (IF) by mixing it with a local oscillator signal (LO). The resulting IF signal is then processed by an IQ detector to separate the I and Q components. These components are subsequently filtered using an Infinite Impulse Response (IIR) filter before being compared to values in a set point table. Any errors generated by this comparison are then fed to the controller, which in this case is a Proportional Integrator (PI) controller and a disturbance observer-based (DOB) controller. The outputs of these controllers are the I and Q components, which are converted back into an IF signal by the IQ-Demodulator, and then up-converted to an RF signal. This RF signal is then sent to the preamplifier to drive the high-power RF source (such as

a Klystron). The output of the Klystron, via the waveguide and directional coupler, powers the RF cavity through the input power coupler, completing the feedback loop. The basic components of the LLRF system are described as under.

3.8.1 Mixers

Mixers are signal multipliers. The output of a mixer is the signal which is a product of the two input signals. By simple trigonometry, it can be shown that if two signals with frequencies f_{RF} and f_{LO} are multiplied with each other then the output signal will have two frequency components "$f_{RF}+f_{LO}$" and "$f_{RF}-f_{LO}$". By filtering we can get the lower sideband for down-conversion, as depicted in Figure 3.40. The benefit of down conversion lies in the fact that it reduces the signal's frequency while retaining crucial amplitude and phase information that we aim to manipulate. This lower-frequency signal can be effortlessly converted into a digital format using readily available Analog-to-Digital Converters (ADCs), after which digital control algorithms can be implemented. In the
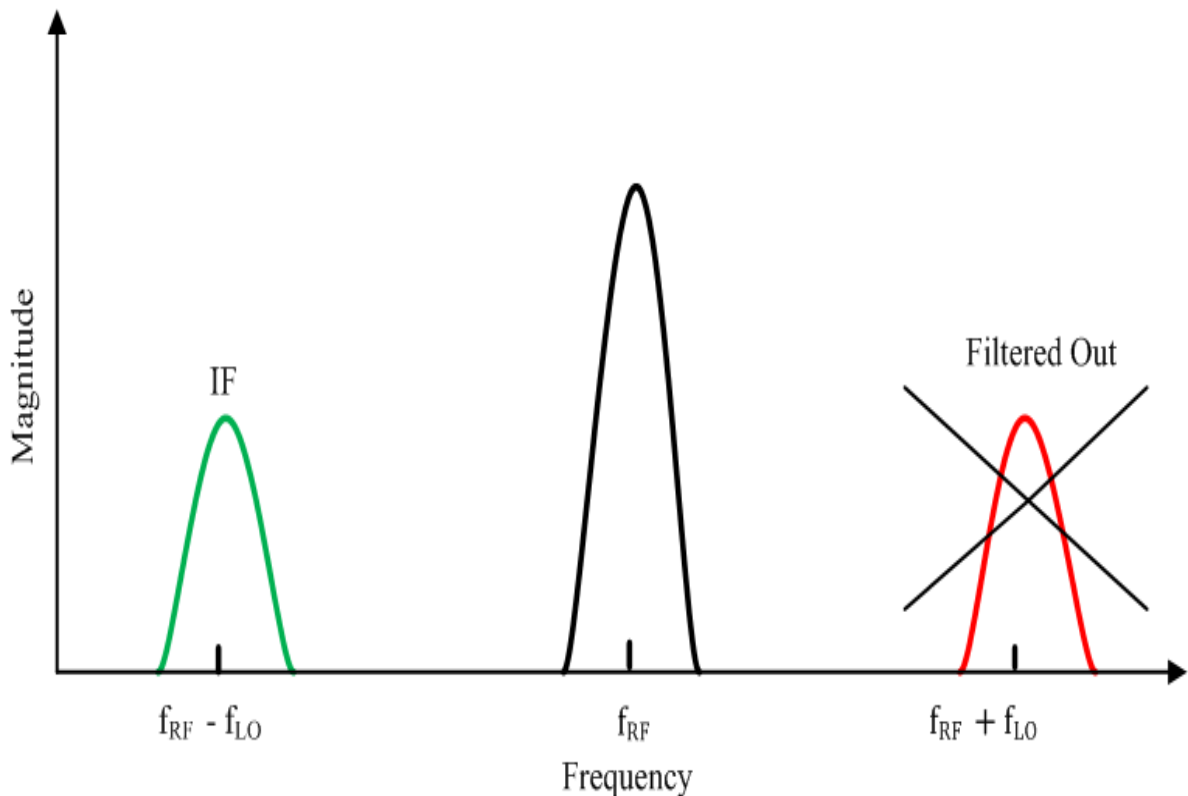
FIGURE 3.40: Mixer output spectrum with centered RF signal

LLRF system mixers are used for down conversion from RF signal at frequency ω_{RF} to

intermediate frequency ω_{IF} and for upconversion from ω_{IF} to ω_{RF}. For this purpose, a stable local oscillator at frequency ω_{LO} is required. For understanding the working principle consider two signals x_1 and x_2 at frequencies ω_{RF} and ω_{IF} respectively with phase difference ϕ as described in Equation 3.35. The output of mixer denoted by y is given in Equation 3.37

$$x_1 = A_1 Cos(\omega_{RF}t + \phi); x_2 = A_2 Cos(\omega_{LO}t). \tag{3.35}$$

$$y = A_1 Cos(\omega_{RF}t + +\phi) * A_2 Cos(\omega_{LO}t). \tag{3.36}$$

$$y = \frac{A_1 A_2}{2}Cos((\omega_{RF} - \omega_{LO})t + \phi) + \frac{A_1 A_2}{2}Cos(\omega_{RF} + \omega_{LO} + \phi)t. \tag{3.37}$$

$$\omega_{IF} = \omega_{RF} - \omega_{LO}. \tag{3.38}$$

3.8.2 IQ modulators

Usually, a fixed-frequency RF signal is represented by its phase and amplitude, which is the signal representation in a polar coordinate system. Consider a signal with amplitude "A" and phase "ϕ", represented as a vector with magnitude "A" at angle "ϕ" with the x-axis. For the IQ representation of the signal, the x-axis is marked as real I i-e in phase and the y-axis as imaginary Q i-e in quadrature. These I and Q are projections of the vectors on real and imaginary axes.

$$x = Ae^{j\phi} = I + jQ. \tag{3.39}$$

when the signal is converted into I and Q components by IQ demodulator as shown in Figure 3.41 the magnitude and phase of signals are preserved, which is the output of IQ modulator as shown in Figure 3.42 and can be computed from IQ components as

$$A = \sqrt{I^2 + Q^2} \quad ; \quad \phi = \tan^{-1}(\frac{Q}{I}). \tag{3.40}$$

To elaborate the IQ variation with magnitude and phase, consider a sinusoidal signal with exponential magnitude variation and low-frequency sinusoidal phase variation represented in Figure 3.43. Its magnitude and phase variation and corresponding I and Q variations are plotted at the bottom of the Figure.
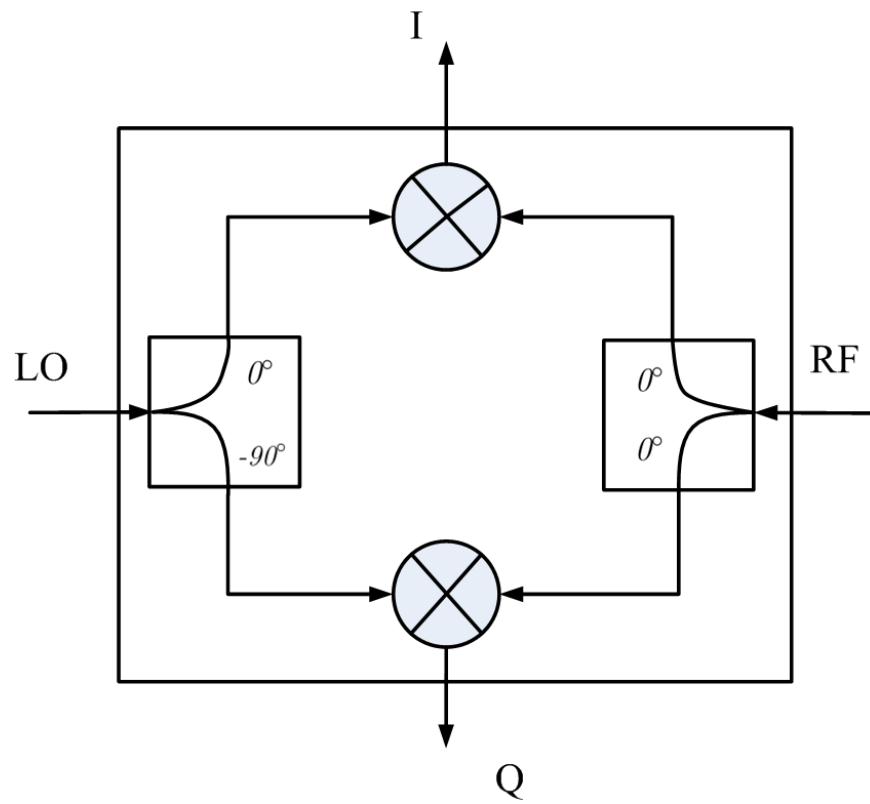
FIGURE 3.41: IQ Demodulator
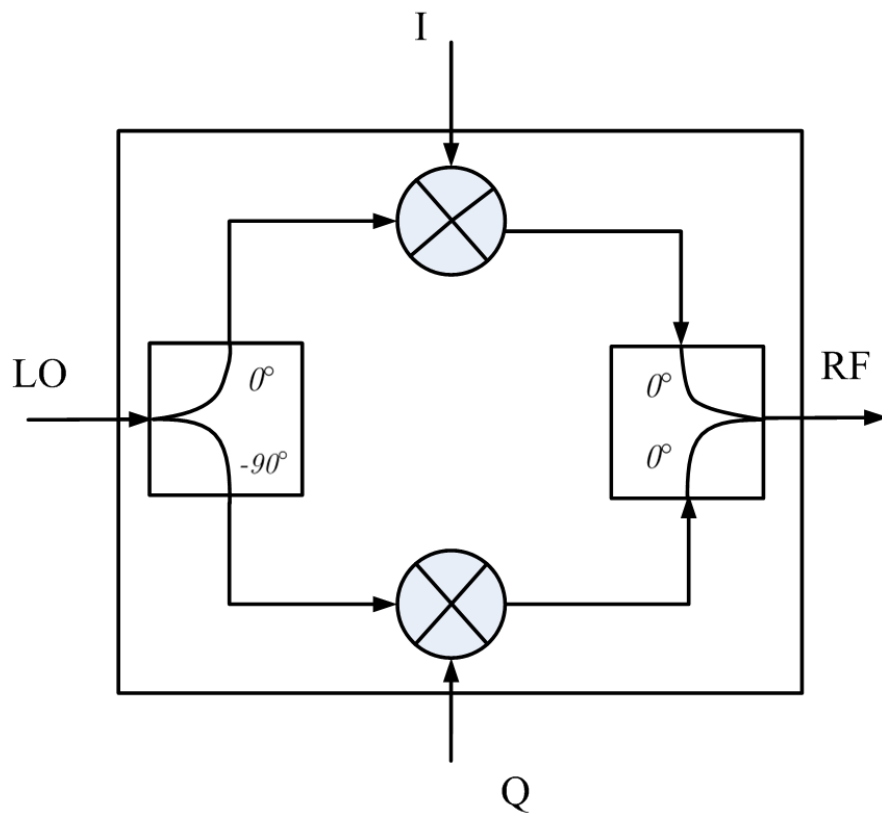
FIGURE 3.42: IQ Modulator
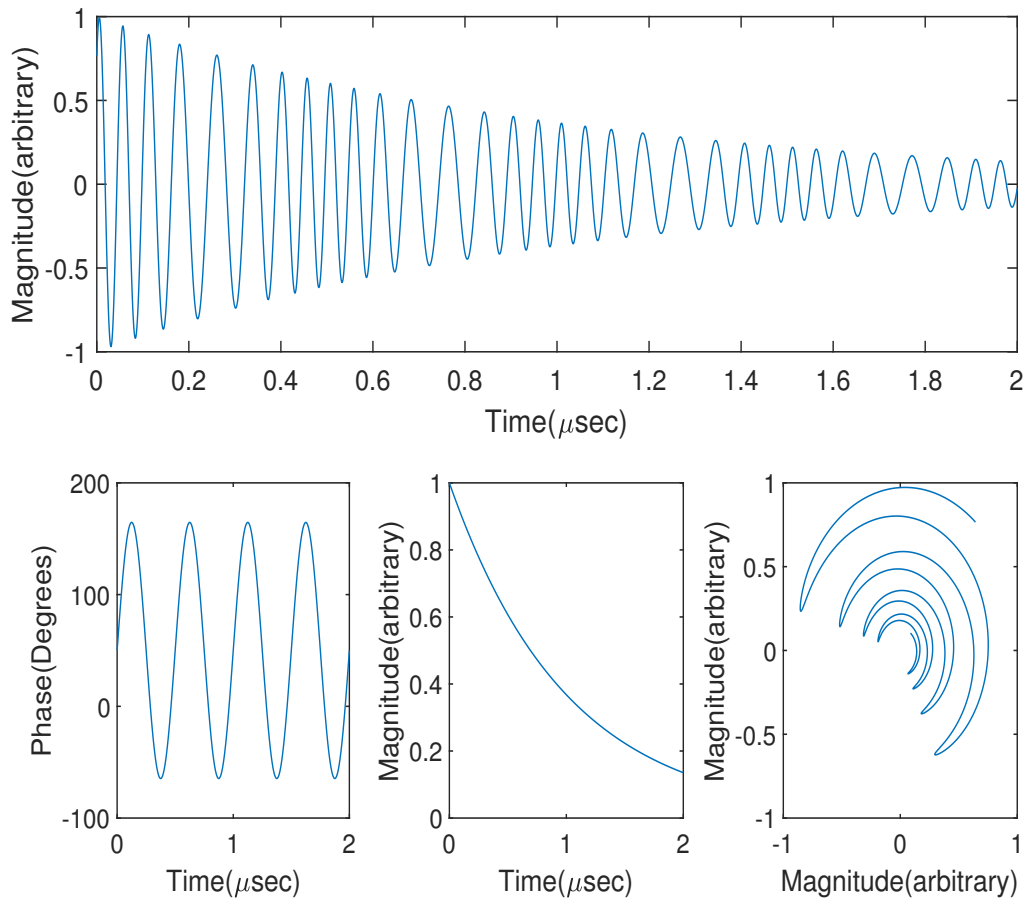
FIGURE 3.43: Magnitude and phase variation in RF signal and their corresponding IQ variation

3.8.3 Reference Master Oscillator

Reference Master Oscillator (RMO) is a highly stable signal source to drive the LLRF system. RMO signal is frequency divided to produce intermediate frequency frequency(IF) and clock(CLK). If signal is further mixed with the RMO signal for the local oscillator(LO) frequency as depicted in Figure 3.44. RMO also provides the RF signal for the Klystron drive amplifier.

3.8.4 Filters

Filters are used at various stages of the LLRF system. For example, at the down-conversion stage a low-frequency bandpass filter is used similarly at upconversion high-frequency bandpass filter is used.
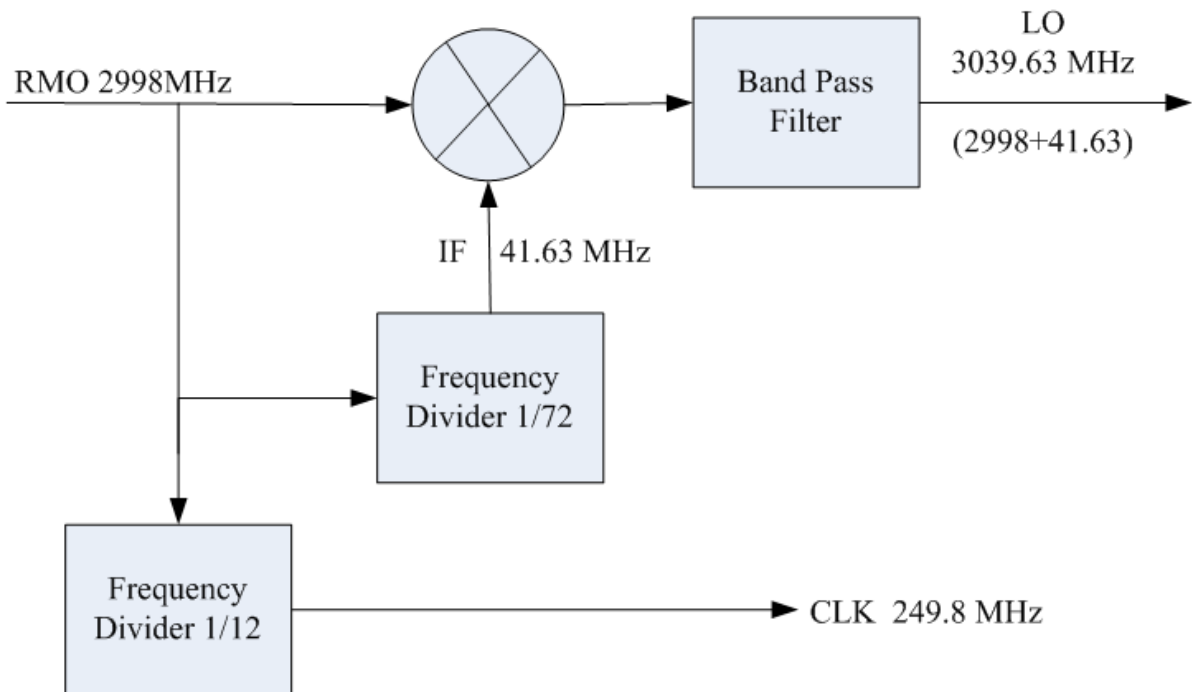
FIGURE 3.44: LO and CLK Generation by RMO

3.8.5 RF Controller

RF controller is designed to generate the control input to drive the RF drive such that the cavity signal follows the reference desired output. The error signal is generated by comparing the cavity signal and setpoint values and in the RF controller section the error signal is processed to produce a control input to achieve the desired cavity field. The setpoint IQ values are compared with the IQ values obtained after down-conversion and IQ modulation of the cavity voltage signal. Nowadays this section is usually implemented in FPGAs. Adaptive feedforward and disturbance observer-based control with PI control have been studied in this thesis.

3.8.6 Pre-amplifier

Nowadays due to development in solid state technology high frequency and Kilowatts power range solid state amplifiers are available. These amplifiers serve the purpose of a klystron driver called pre-amplifiers. For example, a 200W pulsed power amplifier is used to drive 10 MW power Thales TH-2157A klystron. In a pulsed particle accelerator, the trigger for the pre-amplifier is synchronized with a pulsed modulator and electron

gun pulse power supply. The amplitude and phase of the output of the pre-amplifier depend on the master oscillator driving the preamplifier.

3.9 RF Power Sources for Particle Accelerators

The functioning of particle accelerators heavily relies on RF power sources, essential for supplying the energy required to accelerate particles to high velocities. These power sources exhibit a diversity of forms, each designed to meet the specific needs of particular accelerator setups. In this chapter, a concise overview of different radio frequency (RF) sources for accelerators is presented. We will comprehensively explore Magnetrons and Klystrons as RF power sources employed in particle accelerators.

3.9.1 Magnetron
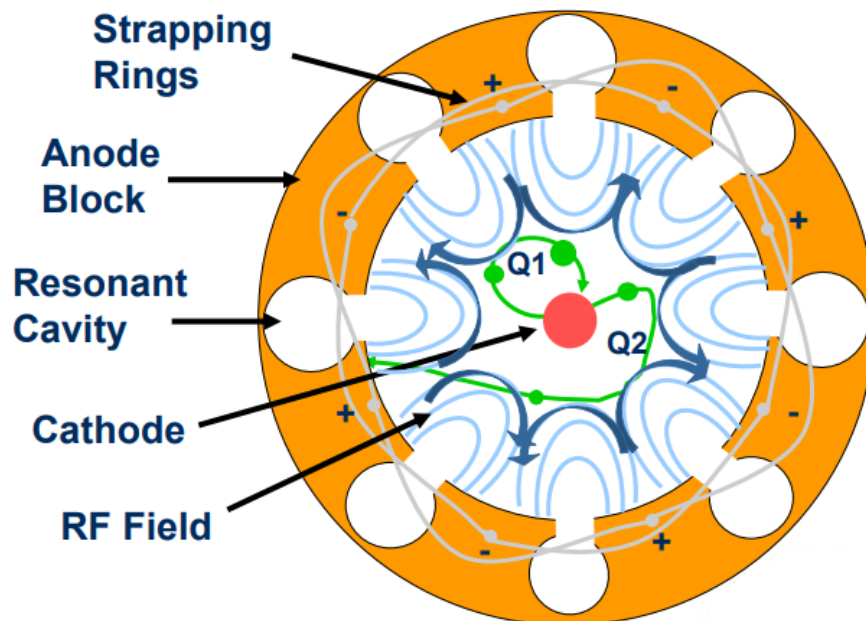
FIGURE 3.45: RF Field and electron trajectories in Crossection diagram of magnetron [77].

The magnetron is a vacuum tube oscillator designed to generate high-power microwaves. Its structure comprises a central cathode responsible for emitting high-energy electrons,
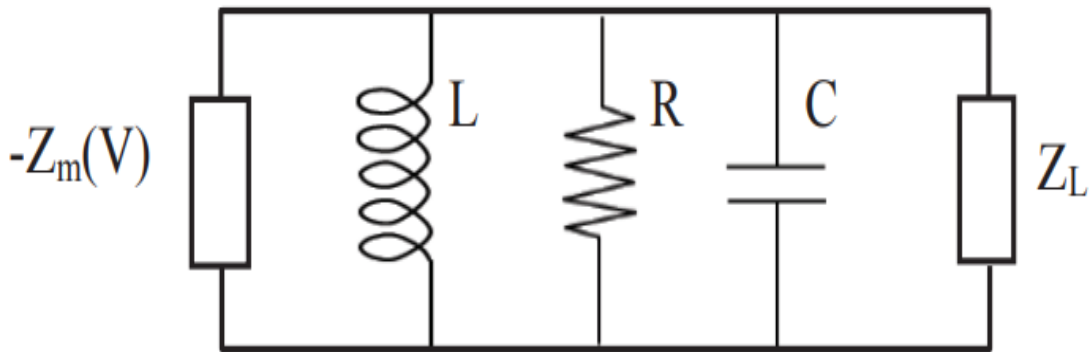
FIGURE 3.46: Magnetron equivalent circuit model with load impedance Z_L

resonant cavities surrounding the cathode within a cylindrical anode, and an axial magnetic field that guides the electrons in the circular path between the cathode and the resonant cavities. A pickup antenna located on one of the resonant cavities serves to couple the microwaves produced within the magnetron to the waveguide.

The cross-section diagram of a magnetron, highlighting the electron trajectories and RF field is depicted in Figure 3.45. The electron Q_1 takes energy from the RF field and hits back the cathode while the electron Q_2 gives energy to the RF field and travels to the anode block. The cloud of electrons is formed between the cathode and anode and due to the presence of a cross-magnetic field these electrons move in a circular path forming wheel spokes type movement in *pi*-mode oscillation, boot straping is used to support this mode.

Magnetron is an oscillator, which is usually modeled as an LC tank circuit, Resistance R for wall losses, a negative impedance Z_m, and load impedance Z_L as shown in Figure 3.46 [76].

3.9.2 Klystron

The Klystron is a vacuum tube amplifier that operates based on the principle of velocity modulation of an electron beam. In the input cavity, known as the buncher cavity, RF energy couples with the electron beam. This RF energy typically originates from a solid-state RF amplifier, known as the Klystron RF drive. As a result of the RF signal, the electron beam undergoes velocity modulation, forming bunches. These bunches travel a distance from the buncher cavity to another cavity called the catcher cavity through
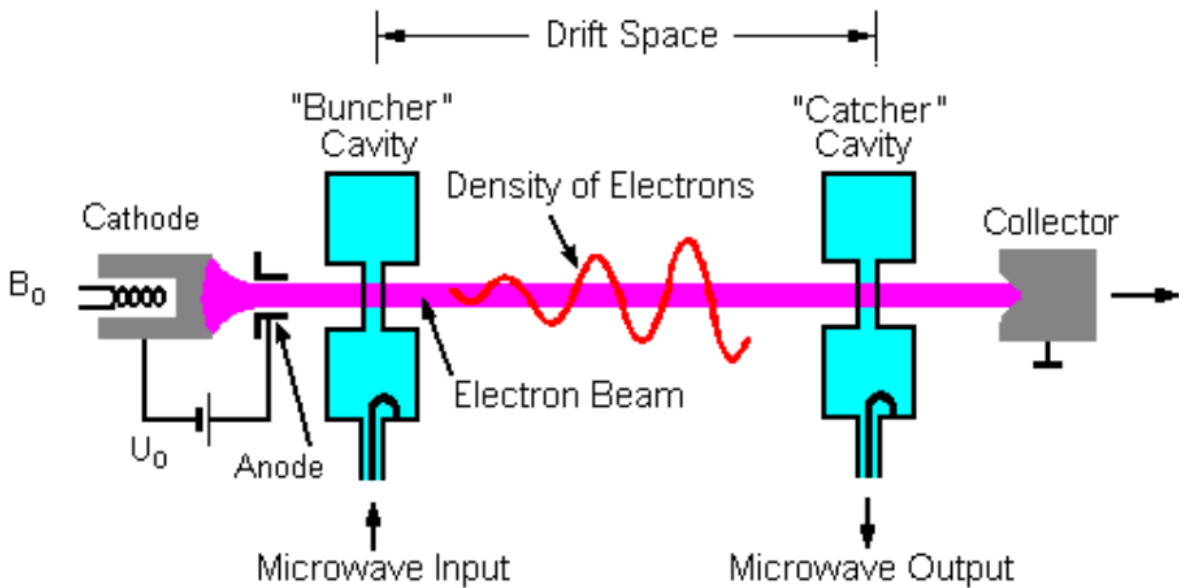
FIGURE 3.47: The Two Cavity Klystron [78].

TABLE 3.6: Comparison of the Magnetron and the Klystron as an RF Source for Particle Accelerator

Parameter	Magnetron	Klystron
Cost	Lower	Higher
Size	Smaller	Larger
Efficiency	Higher	Lower
Frequency Tuning range	Large	small
Noise	Higher	Lower
Modulator Cost	Lower	Higher
Peak Power	Lower	Higher
Frequency and power stability	Lower	Higher

a beam pipe referred to as the drift space. In the catcher cavity, RF energy from the electron bunches couples with an external waveguide through an output antenna. This working principle of klystron is elaborated in Figure 3.47.

Klystrons offers several advantages, including precise frequency control, higher peak power, and the ability to precisely control frequency, amplitude, and phase. However, Klystrons also have drawbacks such as higher cost, larger size, and the need for higher pulse voltage requirements from modulators as compared to magnetrons. the comparison of klystrons and magnetron are presented in Table 3.6.

3.9.3   Tetrodes

In old particle accelerators tetrodes were used as RF power sources to drive RF cavities [79]. The tetrode, an early electronic vacuum tube composed of four essential elements, played a pivotal role in the formative stages of electronics. It featured a cathode, responsible for emitting electrons when heated, and an anode (also known as a plate) that gathered these emitted electrons to facilitate their flow within the tube. Positioned between the cathode and anode, the control grid allowed precise control over the flow of electrons, making tetrodes invaluable for amplifying electrical signals. Furthermore, the screen grid, strategically placed between the control grid and anode, acted as a protective shield, enhancing the tube's performance by mitigating issues like "grid current." Tetrodes found extensive use in early 20th-century electronics, particularly in radio technology and communication systems, due to their ability to achieve high gain and power amplification. However, they were not without their drawbacks, including secondary emission, which introduced distortion into output signals, and the phenomenon known as the "tetrode kink." In response, further technological advancements led to the development of more sophisticated vacuum tube types, such as the pentode. While solid-state devices like transistors eventually supplanted tetrodes in modern electronics, their historical significance in shaping electronic technology remains unquestionable.

3.9.4   Inductive Output Tubes (IOT)

Inductive Output Tubes (IOTs) were initially called klystrodes because they represent a hybrid technology that merges resonant circuit concepts from cavities with grid modulation techniques used by triodes and tetrodes. While initially conceptualized by Haeff in the 1939 [80], but their commercial manufacturing was achieved in 1982 [81].
Traditional IOTs were used in TV transmitters as audio and visual channel amplifiers they are also used in particle accelerators [82]. They are used on several international high-energy particle accelerators such as European Spallation Source (ESS) CERN and Diamond [83].
IOTs function similarly to triodes, permitting the flow of electrons from the cathode to the anode when the plate carries a positive charge, a process regulated by the grid. IOTs extract RF power from an electron beam by directing it through a resonant cavity,

which initiates beam bunching at the cathode through the application of RF voltage. In contrast to Klystrons, IOTs possess a shorter structure due to the utilization of a single resonant cavity. This design allows for better control of a wider electron beam, resulting in enhanced overall efficiency, which has been documented to reach impressive levels, sometimes as high as 80% [84]. However, it's worth noting that IOTs exhibit lower gain and necessitate a higher drive power compared to alternative technologies, such as the Klystron. Another drawback is that its upper-frequency limit is 1.3GHz, which is dependent on transit time between cathode and grid [85]. At CERN in LINAC4 the buncher cavity is powered by high power IOT operating at 352MHz at 1Hz and 2Hz repetition rate, which may be replaced by solid state amplifier in future.

3.9.5 Solid State RF Source

The ongoing advancements in solid-state technology suggest the potential replacement of high-power vacuum tubes within the 100 to 3000 MHz frequency range [86]. The primary advantage of solid-state technology is the enhanced reliability it offers when compared to vacuum tubes, which require extremely high voltage power supplies, typically in the multi-kilovolt range. Solid-state amplifiers operate at significantly lower voltages, reducing this reliability concern by orders of magnitude.

For accelerator projects which require megawatt RF power, Klystron [87–93] and multi-beam Inductive output tubes(MBIOTs) are still the only candidate. Additionally, the use of Solid-State Power Amplifiers (SSPAs) can lead to substantial energy savings in driving Superconducting Radio Frequency (SRF) cavities when employing an optimized feeding profile during pulsed operation. SSPAs offer several advantages, such as modularity, high efficiency, low phase noise, reduced harmonics, lower maintenance and operational costs, redundancy, quick start-up, and cost-effectiveness. These features make them a compelling choice for various projects, especially in the mid-range power levels, ranging from a few kilowatts to several hundred kilowatts. The development of SSPA technology gained momentum at the SOLEIL synchrotron, where it successfully replaced vacuum tube amplifiers for powering its booster and storage rings [94]. This achievement has led to the widespread adoption of SSPA technology in facilities worldwide, resulting in energy savings, cost reduction, compactness, improved reliability, ease

of mass production, and extended use across different frequency bands.

Furthermore, collaborations with industry experts in high-power broadcasting applications have yielded superior SSPA designs, aiming to fully replace mid-range power vacuum tubes. These projects have resulted in significant power reduction and enhanced redundancy. SSPA technology has expanded into higher frequency ranges, such as the L-band, thanks to Gallium Nitride (GaN) semiconductor technology. It has been utilized in various projects, including accelerators, superconducting linear accelerators, and other applications.

Efficiency improvement in RF power sources is a crucial focus, with a 10% increase in efficiency leading to substantial operational cost reductions. However, achieving improved efficiency can sometimes complicate design and increase costs. Higher complexity can also pose challenges in tuning SSPA modules within a system due to amplitude and phase variations. The RF community seeks approaches that balance efficiency, compactness, ease of production, and affordability for next-generation RF power sources. Handling full power reflection during the cavity-filling period is another concern for RF power sources, especially in high-intensity accelerator facilities. This issue remains a subject of theoretical studies, with practical solutions still in development.

In designing RF power sources, SSPA module and sub-system properties are interrelated, making it challenging to prioritize efficiency, cost, and complexity. A successful design not only maximizes DC-to-RF conversion but also minimizes cost and complexity. In summary, the evolving landscape of solid-state technology, particularly SSPAs, is revolutionizing the field of RF power sources by offering improved reliability, energy efficiency, and performance across various applications.

3.10   Summary

In this chapter, we begin by introducing the single-cell cavity model and presenting simulation results, aimed at providing a foundational understanding of accelerator cavities. Subsequently, we explore the internal RF dynamics of the nine-cell TESLA cavity, accompanied by a modal analysis of its mechanical aspects. The simulation results highlight the significance of understanding cavity internal field dynamics within the model. Integrating this understanding into the cavity simulator enhances its accuracy.

We provide an overview of the fundamental building blocks and key components of the low-level RF system of a particle accelerator.

Moving forward, the following chapter explores the application of disturbance observer-based control to address the cavity field control problem.

Chapter 4

Disturbance Observer Based Control

4.1   Introduction

Disturbance observer-based (DOB) control is a control strategy that improves the ability of control systems to withstand external influences that affect the system output but are not directly regulated. These disturbances include system uncertainties, noise, and external forces. The fundamental idea behind DOB control is to estimate and correct these disturbances in real time using a disturbance observer that provides a compensating signal to the controller, thereby optimizing the system's performance. The controller then adjusts the system output to counteract the disturbance's impact. DOB Control is widely used in various fields such as robotics, automotive engineering, aerospace, and particle accelerators. Traditional DOB control block diagram with plant transfer function $\mathbf{G}_p(s)$, nominal plant transfer function $\mathbf{G}_n(s)$ and filter $\mathbf{Q}(s)$ is shown in Figure 4.1. In designing Traditional DOB, the inverse of the plant transfer function is required. To make the inverse realizable the filter $\mathbf{Q}(s)$ is designed. Since nominal plant transfer function $\mathbf{G}_n(s)$, used in DOB design may differ from the actual plant $\mathbf{G}_p(s)$, so disturbance estimation may have errors. The bandwidth of filter $\mathbf{Q}(s)$, further limit the performance of DOB as the disturbances with higher frequency than the bandwidth of filter $\mathbf{Q}(s)$, will not be estimated and so would not be compensated [95].
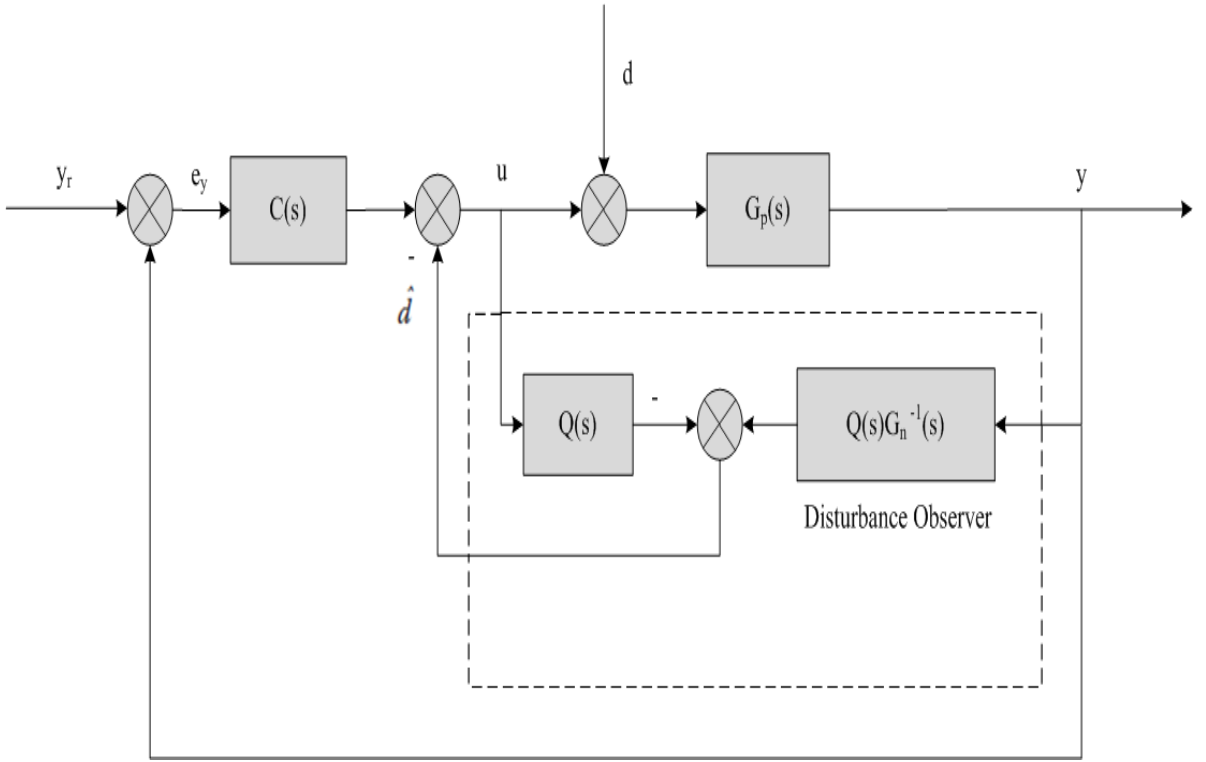
FIGURE 4.1: Conventional DOB Diagram

4.2 Learning based DOB

Learning-based DOB was proposed by Zheng et. al.[53] and is described in this section. The motivation for learning base DOB is the iterative learning control (ILC). It is particularly useful for repetitive disturbances, in our case beam loading and Lorentz force detuning are repetitive disturbances.

In learning-based DOB, the estimation of disturbance by conventional DOB $\hat{d}^o$ is improved by the term $\hat{d}_i^f$, which is computed by the historical data of the system. The learning-based DOB framework is presented in Figure 4.2. The disturbance estimate $\hat{d}$ is given by

$$\hat{d} = \hat{d}^f + \hat{d}^o. \tag{4.1}$$

In the learning scheme, the recursive learning term computed from the previous iteration is added to the current iteration The learning law for the iterative learning scheme is given as under

$$\hat{d}_{i+1}^f = \hat{d}_i^f + \mathbf{L}(z)e_i. \tag{4.2}$$

Where, $\mathbf{L}(z)$ is learning function, $\hat{d}_{i+1}^f$ learning term in current iteration, $\hat{d}_i^f$ and e_i are learning term and tracking error in the previous iteration respectively. If $\mathbf{G}_r(z)$ is
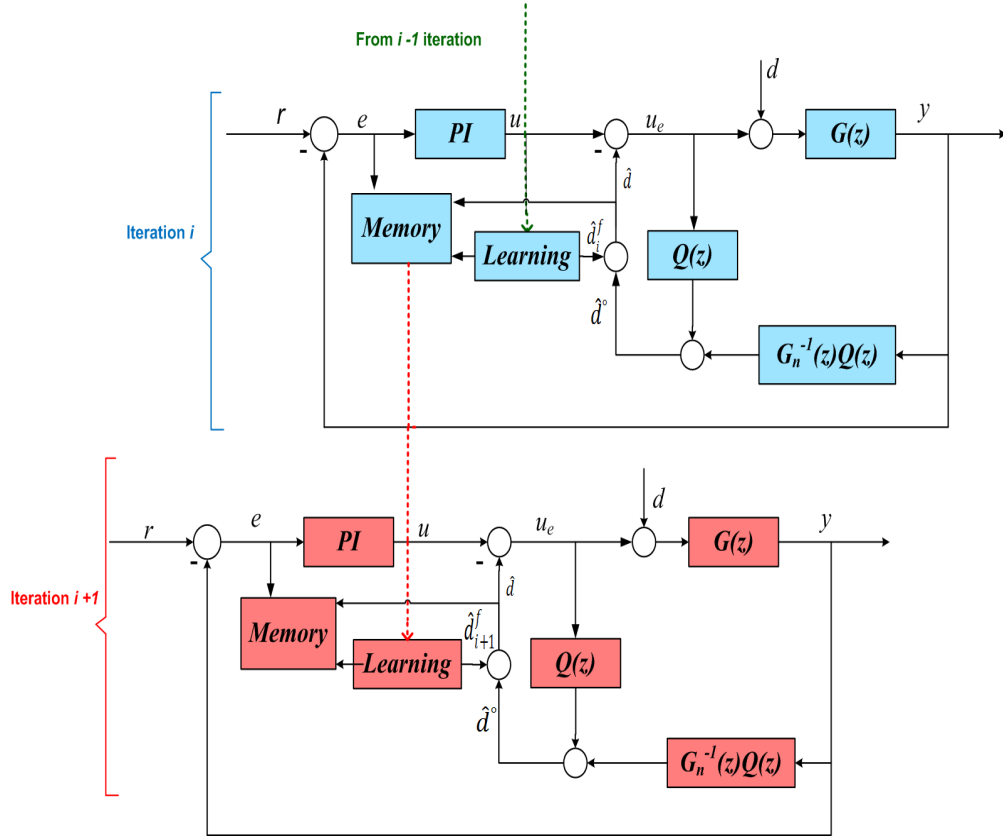
FIGURE 4.2: Learning-based Disturbance Observer Scheme with PI Controller

transfer function from reference to output $\mathbf{G}_f(z)$, is transfer function from $\hat{d}^f$ to output and $\mathbf{G}_d(z)$ is transfer function from disturbance d to output then output can be written as

$$y = \mathbf{G}_r(z)r + \mathbf{G}_f(z)\hat{d}^f + \mathbf{G}_d(z)d. \qquad (4.3)$$

For *ith* iteration output y_i would be

$$y_i = \mathbf{G}_r(z)r_i + \mathbf{G}_f(z)\hat{d}_i^f + \mathbf{G}_d(z)d_i. \qquad (4.4)$$

Similarly fir $i + 1$ iteration output y_{i+1} would be

$$\begin{aligned} y_{i+1} &= \mathbf{G}_r(z)r_{i+1} + \mathbf{G}_f(z)\hat{d}_{i+1}^f + \mathbf{G}_d(z)d_{i+1} \\ &= \mathbf{G}_r(z)r_{i+1} + \mathbf{G}_f(z)[\hat{d}_i^f + \mathbf{L}(z)(r_i - y_i)] \\ &\quad + \mathbf{G}_d(z)d_{i+1}. \end{aligned} \qquad (4.5)$$

From Equation (4.4) we can write

$$\mathbf{G}_f(z)\hat{d}_i^f = -\mathbf{G}_r(z)r_i - \mathbf{G}_d(z)d_{i+1} + y_i. \qquad (4.6)$$

Substituting value in Equation (4.5) we get

$$y_{i+1} = [1 - \mathbf{G}_f(z)\mathbf{L}(z)]y_i + \mathbf{G}_r(z)(r_{i+1} - r_i)$$
$$+ \mathbf{G}_d(z)(d_{i+1} - d_i) + \mathbf{G}_f(z)\mathbf{L}(z)r_i. \tag{4.7}$$

Now the tracking error is given by

$$e_{i+1} = r_{i+1} - y_{i+1}. \tag{4.8}$$

$$e_{i+1} = [1 - \mathbf{G}_f(z)\mathbf{L}(z)](r_i - y_i) - [1 - \mathbf{G}_r(z)](r_{i+1} - r_i)$$
$$- \mathbf{G}_d(z)(d_{i+1} - d_i). \tag{4.9}$$

Assuming r and d are consistent over iterations then $r_{i+1} = r_i$ and $d_{i+1} = d_i$ resulting in

$$e_{i+1} = [1 - \mathbf{G}_f(z)\mathbf{L}(z)](r_i - y_i)$$
$$= [1 - \mathbf{G}_f(z)\mathbf{L}(z)]e_i. \tag{4.10}$$

Learning convergence is achieved by iteratively refining of disturbance estimation. The learning function is designed in such a way that tracking errors will be reduced with time. This can be described as infinity-norm minimization problem:

$$\|1 - \mathbf{G}_f(z)\mathbf{L}(z)\|_\infty < 1. \tag{4.11}$$

4.3 Modified Learning Based DOB for field Control problem

We simulated the iterative learning Equation (4.2), for field control problem in a superconducting accelerator cavity model with a PI controller in MATLAB,Simulink and the result was an unstable system, as the cavity voltage magnitude increasing to infinity. Therefore the learning law is modified by introducing a recursive coefficient a, the modified learning equation is given as

$$\hat{d}_{i+1}^f = a\hat{d}_i^f + \mathbf{L}(z)e_i. \tag{4.12}$$

For stable operation of the system, the value of the recursive coefficient is taken as 0.9. We incorporated learning-based DOB and DOB with PI controller, secondly we have activated the learning scheme after the transient peak of cavity voltage to avoid excessive overshoot in cavity voltage response and gradually increased the recursive coefficient 'a' to its final value '0.9' for better transient response.

By using the modified learning Equation (4.12), the Equation (4.7) will be changed to

$$
\begin{aligned}
y_{i+1} = {}&[a - \mathbf{G}_f(z)\mathbf{L}(z)]y_i + \mathbf{G}_r(z)(r_{i+1} - ar_i) \\
&+ \mathbf{G}_d(z)(d_{i+1} - ad_i) + \mathbf{G}_f(z)\mathbf{L}(z)r_i.
\end{aligned}
\tag{4.13}
$$

With the above updated equation the error in Equation (4.10) will change to

$$
\begin{aligned}
e_{i+1} = {}&[a - \mathbf{G}_f(z)\mathbf{L}(z)]e_i + [1 - \mathbf{G}_r(z)](r_{i+1} - ar_i) \\
&- \mathbf{G}_d(z)(d_{i+1} - ad_i).
\end{aligned}
\tag{4.14}
$$

For consistent values of r and d over iteration as assumed for Equation (4.10), for $a = 0.9$, we can write

$$
\begin{aligned}
e_{i+1} = {}&[0.9 - \mathbf{G}_f(z)\mathbf{L}(z)]e_i + [1 - \mathbf{G}_r(z)](0.1r_i) \\
&- \mathbf{G}_d(z)(0.1d_i).
\end{aligned}
\tag{4.15}
$$

Since in the absence of disturbance, system is tracking well the reference input in steady state, so $\mathbf{G_r}$ is approximately equal to one, therefore $[1 - \mathbf{G}_r(z)](0.1r_i)$ would not contribute much to the error in each iteration and its effect is also reduced by $\mathbf{G}_d(z)(0.1d_i)$ term, which is verified by the results presented in the Section 4.4.

In recursive error Equation 4.15, the dominant term is $[0.9 - \mathbf{G}_f(z)\mathbf{L}(z)]$, Smaller the magnitude of this term, the faster the convergence of learning scheme, as the tracking error in each iteration will be reduced. In Figure 4.3 bode magnitude diagram of $[0.9 - \mathbf{G}_f(z)\mathbf{L}(z)]$ is plotted for different values of L=1:0.5:5. It is evident that below 20KHz the convergence of the learning scheme would be much better so the low-frequency disturbances will be compensated much faster than higher frequency disturbances. In the beam loading case, higher frequency components only exist at the head and tail of the beam pulse, which may be compensated by feed-forward control or would be lower if the rising and falling edges are not very steep.
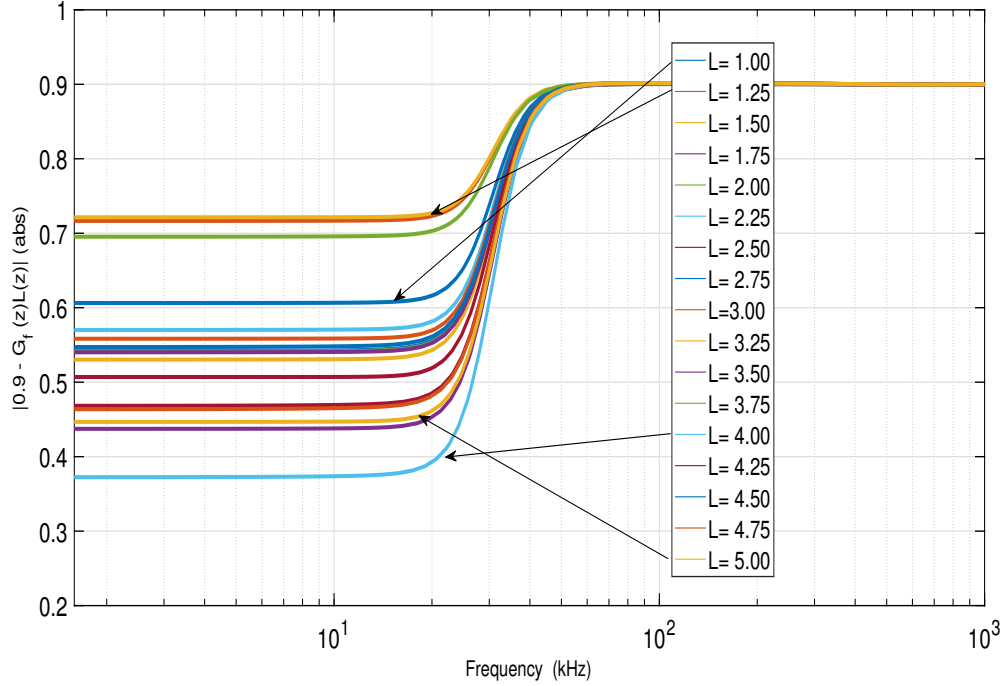
FIGURE 4.3: Effect of learning Function L is studied on learning convergence. Bode magnitude plot of $|0.9 - G_f(z)L(z)|$ for $L = 1 : 0.5 : 5$.

4.4 Simulation Results and Discussion

The cavity baseband model for π-mode is simulated in Simulink MATLAB with PI, DOB, and learning-based DOB controllers. PI gains $K_p = 80$ and $K_I = 1.3 \times 10^5$ are used [25]. For disturbance observer-based (DOB) control, we have assumed the nominal plant model with a mismatch in cavity half bandwidth and $-20Hz$ offset in cavity detuning, $1\mu sec$ loop delay and $50Hz$ cavity half bandwidth. For better transient results the PI gains and DOB gains are gradually increased during the rise time of pulse.

A trapezoidal beam pulse is introduced during the flat portion of the voltage pulse [73] having $66\mu A$ peak current [25] as shown in Figure 4.4. The $\mathbf{Q}(s)$ filter used in disturbance observer-based control to make the inverse of the plant transfer function realizable is second-order low pass filter having a transfer function

$$\mathbf{Q}(s) = \frac{1}{(\tau s + 1)^2}. \tag{4.16}$$

Where τ defines the filter bandwidth. At the rising and the falling edge of beam pulse frequency components are higher and to compensate for a very sharp beam pulse higher
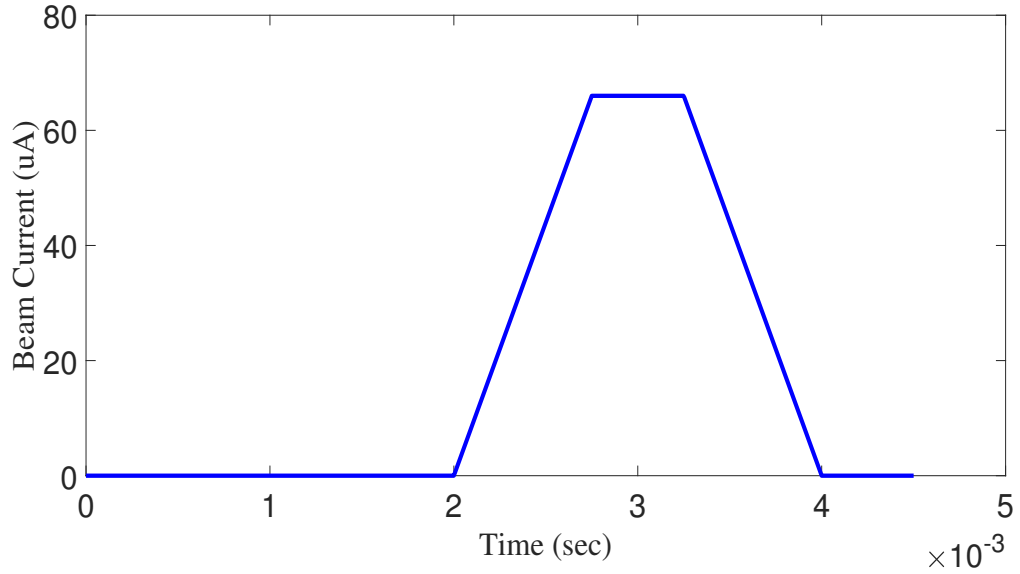
FIGURE 4.4: Trapezoidal Beam Pulse Waveform, $66\mu A$, $2ms$

bandwidth the filter is required in the disturbance observer otherwise higher frequency components in disturbance would not be estimated and compensated. If the sampling time is T_s then the actual system's time delay T_d is modeled as digital delays equal to the floor value of ratio of T_d and T_s, given as

$$Delay = z^{-k}, where \quad k = \lfloor \frac{T_d}{T_s} \rfloor. \tag{4.17}$$

In Figure 4.5. the cavity voltage magnitude for DOB+PI and LDOB+PI controller, are ploted. The reference tracking convergence time and steady-state tracking error are much better in the case of LDOB as compared to DOB control. Due to faster convergence, flat top duration is increased and wider beam pulse load can be managed. The cavity voltage phase is plotted in Figure 4.6, showing better tracking to the reference phase in the case of LDOB+PI as compared to DOB+PI controller.

In Table 4.2, a comparison of the performance of DOB and LDOB is presented. The learning function was tuned to the value of 4.4 for $-10Hz$ cavity detuning, for other cavity detuning, it needs to be optimized that's why for $L = 4.4$, at detuning of $-10Hz$, LDOB gives best results. Overall performance in magnitude and phase stability of LDOB+PI control is much better than DOB+PI control. From the results presented it is evident that a learning-based DOB gives a better magnitude and phase stability in superconducting cavity field control problem as compared to conventional DOB.
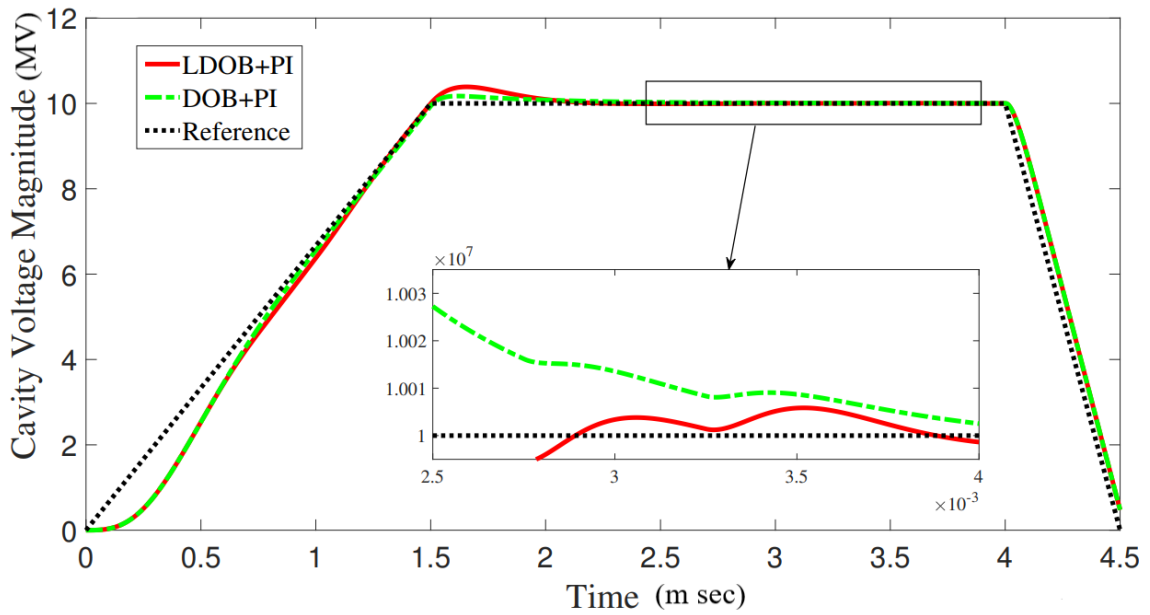
FIGURE 4.5: Cavity Voltage Magnitude for LDOB+PI and DOB+PI Controller, Elaborating Flat Top Voltage Stability
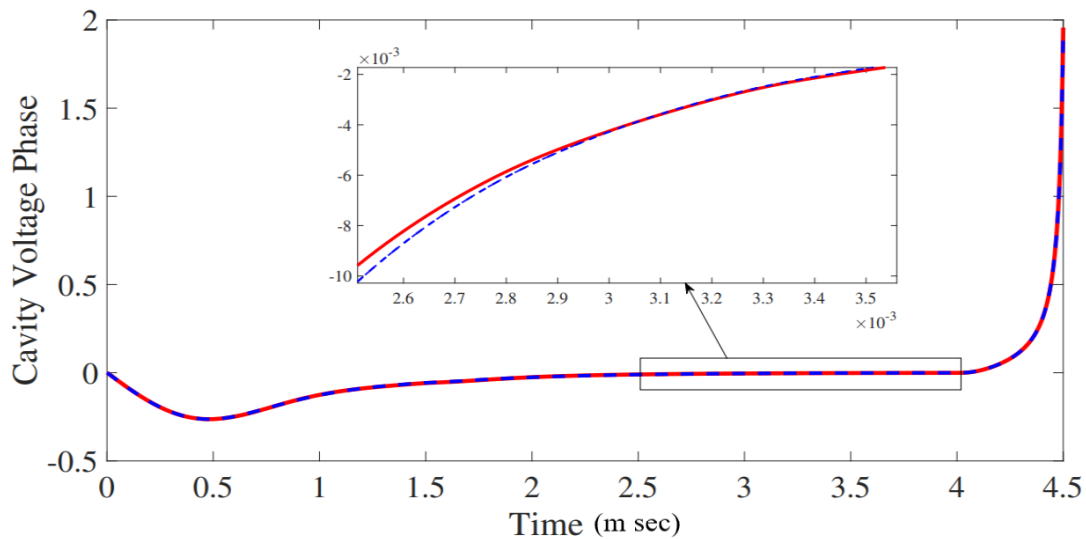
FIGURE 4.6: Cavity Voltage Phase for LDOB+PI and DOB+PI Controllers, Elaborating Phase Stability during Flat Top

In [25] results of conventional disturbance observer with proportional control for beam loading compensation was presented, which were better than proportional only or PI control only. Proportional control without integral action gives a steady-state error, which might be improved by feedforward control, furthermore the flat top portion is lesser in proportional plus DOB control as compared to PI plus DOB control, not suitable for longer beam pulse operation. We have simulated PI plus DOB and PI plus learner-based DOB and improvement in Magnitude and phase stability was observed as
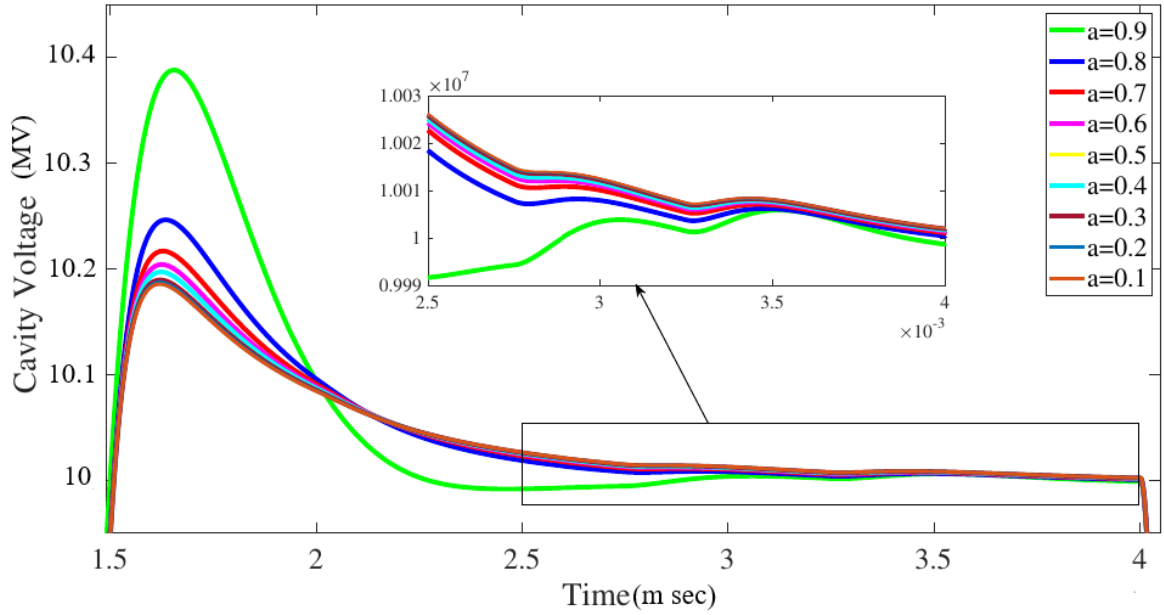
FIGURE 4.7: Effect of Recursive Coefficient a on Cavity Voltage Magnitude Transients, Elaborating Overshoot and Magnitude Stability in Flat Top

presented in Table 4.2.

In [28] iterative learning control plus DOB control were tested in the RF cavity simulator test bench but in iterative learning control the data from the previous pulse was used to improve the current pulse and disturbance observer performance was not improved

TABLE 4.1: Effect of Recursive Coefficient a on Overshoot and Magnitude Stability.

a	%**Overshoot**	Voltage Magnitude Stability Δ**A/A (% rms)**
0.9	3.88	0.0447
0.8	2.47	0.0849
0.7	2.17	0.1067
0.6	2.05	0.1161
0.5	1.97	0.1213
0.4	1.93	0.1245
0.3	1.90	0.1267
0.2	1.88	0.1283
0.1	1.86	0.1295
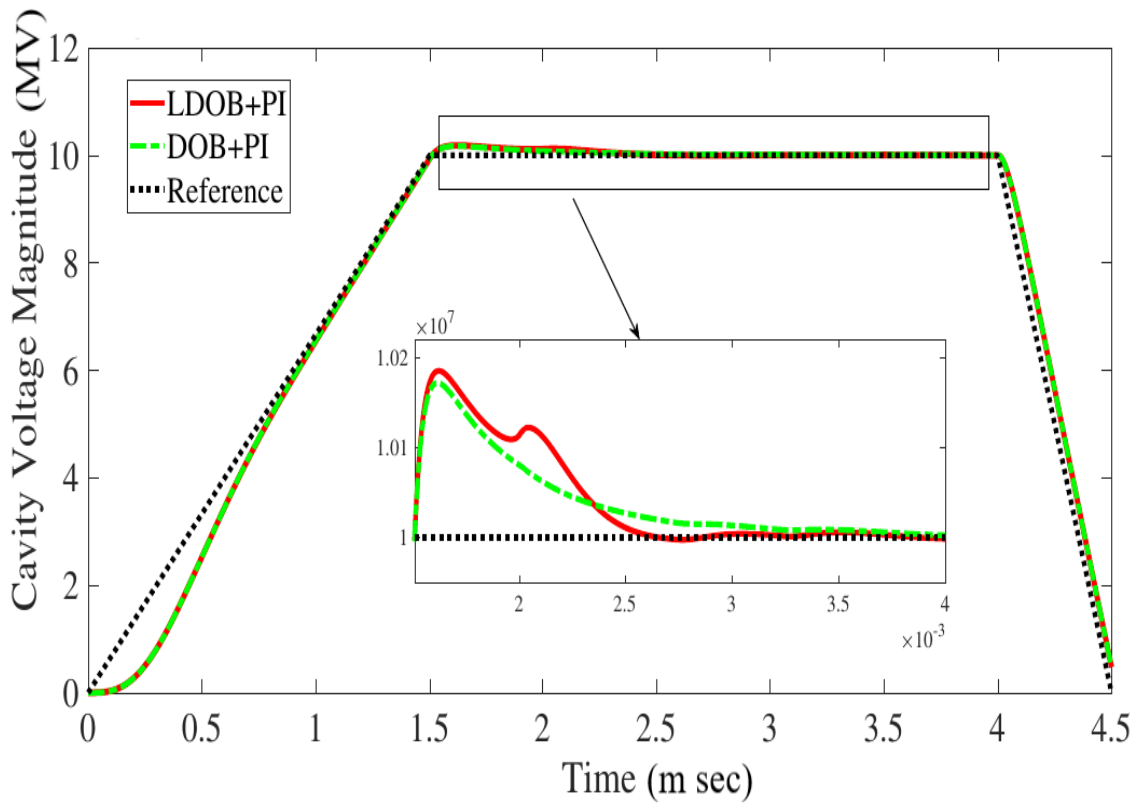
FIGURE 4.8: Cavity Voltage Magnitude for LDOB+PI and DOB+PI Controllers, variable Recursive Coefficient a Switched on at 1.5msec and Reach to 0.9 at 2msec, Additional Overshoot due to LDOB is Reduced

during the current pulse operation. In learning-based DOB, during the current pulse the error is reduced by iterative learning. In future iterative learning disturbance observer in combination with iterative learning control may be tested for further improvement in cavity voltage stability from pulse to pulse. For different values of recursive coefficient 'a' the learning- based DOB is simulated and the cavity voltage is plotted as shown in Figure 4.7. The percent overshoot and voltage magnitude stability ($\triangle\mathbf{A}/\mathbf{A}$ ($\%rms$)) during flat top is given in Table 4.1. The percent overshoot during transient the response is lower at lower values of recursive gain 'a' in the learning scheme but $\triangle\mathbf{A}/\mathbf{A}$ ($\%rms$) is degraded, so there is the trade off between the transient overshoot voltage, the cavity can withstand, and the performance of the learning scheme. One way of avoiding access cavity voltage during transient is to make the recursive gain variable and switch it on after the transient peak and gradually increasing its final value. In Figure 4.8, the cavity voltage magnitude is plotted, the recursive coefficient 'a' is switched on at 1.5 msec and gradually its value is increased from 0.1 to 0.9. By switching delay and gradually increasing the recursive coefficient value the access percent overshoot during

transient is decreased by a considerable amount and $\triangle\mathbf{A}/\mathbf{A}$ ($\%rms$) during beam time is also acceptable as compared to DOB control.

4.5   Summary

Performance analysis of a learning-based Disturbance Observer controller for compensating beam loading and cavity detuning in pulsed superconducting radio frequency cavities is presented in this chapter. The cavity standard π-mode model, with PI controller and both the observers, i-e conventional DOB and learning-based DOB, are simulated in MATLAB/Simulink.

A modified learning-based DOB is proposed to address stability issues and transient additional overshoot problems with the existing learning-based DOB. Simulation results demonstrate that the proposed learning-based DOB outperforms the conventional DOB controller in terms of disturbance estimation and cancellation, resulting in a 33% reduction in cavity voltage magnitude variation during the flat top. Also, the cavity voltage phase variation is slightly improved with the use of a learning-based DOB. The learning function may need to be optimized for better results at different cavity detuning values. A detailed study and critical analysis of recursive coefficient on performance of learning based disturbance observer control will be explored in future.

To compensate for additional overshoot in the transient response, the recursive coefficient in the learning scheme is varied and the learning scheme is switched after the transient peak time, gradually increasing the recursive coefficient to its final value. The effect of measurement noise and other disturbances, such as power supply ripples and microphonics, and higher-order adaptive disturbance observer filters will be studied in future research.

TABLE 4.2: Performance of conventional DOB and learning-based DOB in the presence of beam loading and different cavity detuning.

Detuning	PI+DOB			PI+LDOB					
	Q = 8kHz		———	Q = 8kHz		Q = 16kHz		Q = 32kHz	
	$\triangle$A/A	$\triangle\Phi$		$\triangle$A/A	$\triangle\Phi$	$\triangle$A/A	$\triangle\Phi$	$\triangle$A/A	$\triangle\Phi$
(Hz)	(%rms)	(deg)		(%rms)	(deg)	(%rms)	(deg)	(%rms)	(deg)
0	0.1502	0		0.0488	0	0.0195	0	0.0082	0
1	0.1484	$5.2e^{-4}$		0.0480	$4.96e^{-4}$	0.0188	$4.95e^{-4}$	0.0088	$4.94e^{-4}$
5	0.1400	0.0026		0.0447	0.0025	0.0178	0.0025	0.0143	0.0025
10	0.1275	0.0052		0.0426	0.0050	0.0225	0.0050	0.0251	0.0049
15	0.1132	0.0078		0.0448	0.0075	0.3340	0.0074	0.0389	0.0074
20	0.0970	0.0104		0.0526	0.0099	0.0483	0.0090	0.0550	0.0099
25	0.0780	0.0130		0.0658	0.0124	0.0662	0.0124	0.0730	0.0124

Chapter 5

Iterative Learning Control

5.1 Introduction

Iterative learning control (ILC) is a control strategy used to improve the performance of a system that repeats a task over time. It compensates for repetitive disturbances like cavity detuning and beam loading in superconducting cavities. In the previous chapter the disturbance estimation was improved using an iterative method, in this chapter iterative learning control is explained in detail, and simulation results of norm optimal iterative learning control for cavity field stability are presented. A combination of disturbance observer-based control and iterative learning control would improve the field stability [28].

In ILC, the control input is updated after each task iteration [96]. The idea is to use the knowledge gained from previous iterations to improve the performance in subsequent iterations. The learning process is typically done offline, where the system is first run through several iterations to collect data on the system's behavior. Once enough data is collected, a learning algorithm is applied to adjust the control law for the next iteration. The process is then repeated until the desired level of performance is achieved. ILC can be used to improve the accuracy and consistency of a system, reduce the amount of time required to complete a task and improve the quality of the output. It is particularly useful in situations where there is a high degree of repeatability in the task being performed. Some common applications of ILC include robotics, manufacturing, automation, and RF accelerators [96–98].

The learning process involves updating the control inputs based on the error between the desired output and the output of the previous iteration. The idea is to use the knowledge gained from previous iterations to adjust the control inputs systematically, thereby reducing the error in subsequent iterations.

There are several types of iterative learning control (ILC) techniques that are used depending on the nature of the system and the task being performed. Here are some common types of ILC:

Repetitive control: This is a basic form of ILC that is used for systems that repeat the same task over and over again. It involves using a feedback loop to compare the actual output of the system with the desired output, and then adjusting the control input to minimize the error between the two.

Adaptive control: This type of ILC is used when the system's parameters are changing over time. The control law is updated based on the system's current state, and the learning process continues as the system operates.

Robust control: Robust ILC is used when the system is subject to uncertainties or disturbances that can affect its performance. It involves designing a control law that is robust to these uncertainties and can still achieve the desired level of performance.

Iterative feedback tuning: This technique is used to tune the parameters of a feedback controller to improve the performance of a system. It involves running the system through multiple iterations and using the data collected to adjust the controller parameters.

Model-based ILC: This approach uses a mathematical model of the system to predict its behavior and improve the control inputs. It involves updating the control law based on the difference between the predicted output and the actual output of the system.

Overall, the choice of ILC technique depends on the specific system and task being performed, as well as the goals and performance requirements. It is important to carefully consider the advantages and limitations of each type of ILC before choosing the most appropriate one for a given application.

For a linear model RF system, model-based iterative learning control can be analyzed using variables $\mathbf{u}$ as control input, $\mathbf{e}$ as tracking error, $\mathbf{L}$ as learning function, $\mathbf{r}$ as reference and $\mathbf{y}$ as the output, shown in a generalized block diagram of iterative learning control in Figure 5.1. The subscript j and j+1 are index of two consecutive iterations. In this figure $C(z)$ and $G_p(z)$ are controller and plant transfer functions, $L(z)$ and $Q_{ILC}(z)$
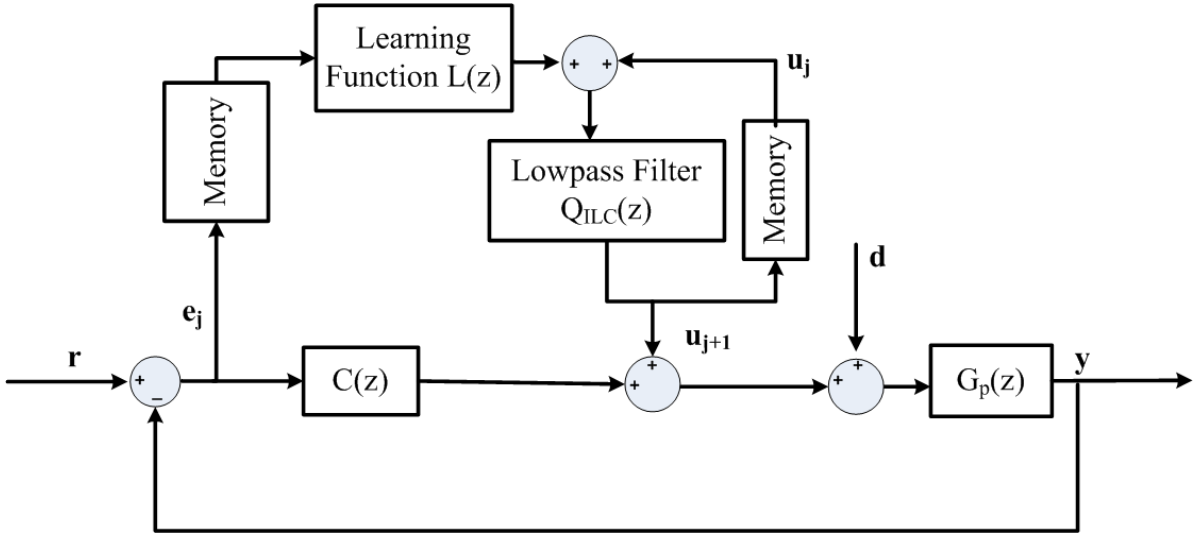
FIGURE 5.1: A generalized block diagram of ILC

are learning function and low pass filter. For pulsed operation of superconducting cavity j i-e iteration number may be taken as the pulse index.

$$\mathbf{u}_{j+1} = \mathbf{u}_j + \mathbf{L}\mathbf{e}_j$$
$$\mathbf{e}_j = \mathbf{r} - \mathbf{y}_j \qquad j = 0, 1, 2, ... \tag{5.1}$$

Here, $\mathbf{L}$ is a $K \times K$ matrix derived from the system model, and the rest are the vectors given under

$$\begin{aligned}
\mathbf{u}_j &= [\mathbf{u}_j(0) \quad \mathbf{u}_j(1) \qquad \mathbf{u}_j(K-1)]^T, \\
\mathbf{y}_j &= [\mathbf{y}_j(0) \quad \mathbf{y}_j(1) \qquad \mathbf{y}_j(K-1)]^T, \\
\mathbf{e}_j &= [\mathbf{e}_j(0) \quad \mathbf{e}_j(1) \qquad \mathbf{e}_j(K-1)]^T, \\
\mathbf{r} &= [\mathbf{r}(0) \quad \mathbf{r}(1) \qquad \mathbf{r}(K-1)]^T.
\end{aligned} \tag{5.2}$$

Here, we assumed consistent reference for each pulse that means set oint is not changing with time.

5.2   FIR Model of RF System

For a discrete linear system with a finite pulse width, its output $\mathbf{y}_j$ and input $\mathbf{u}_j$ of the jth pulse are connected by the system's impulse response:

$$\mathbf{y}_j(n) = \sum_{m=0}^{M-1} \mathbf{h}(m)\mathbf{u}_j(n-m) \qquad n = 0, 1, 2, ..., K-1. \tag{5.3}$$

$$\mathbf{y}_j = \mathbf{G}\mathbf{u}_j. \tag{5.4}$$

where, the transfer matrix $\mathbf{G}$ is given by

$$\mathbf{G} = \begin{bmatrix} \mathbf{h}(0) & 0 & \cdots & 0 \\ \mathbf{h}(1) & \mathbf{h}(0) & \cdots & 0 \\ \vdots & \vdots & \ddots & \vdots \\ 0 & \mathbf{h}(M-1) & \cdots & \mathbf{h}(0) \end{bmatrix}. \tag{5.5}$$

The simplified cavity differential equation representing cavity voltage as $\mathbf{y}(t)$ and input $\mathbf{u}(t)$ is given by

$$\dot{\mathbf{y}}(t) = -(\omega_{1/2} - j\triangle w)\mathbf{y}(t) + \omega_{1/2}\mathbf{u}(t). \tag{5.6}$$

Representing the above continuous time differential equation into a discrete-time equation

$$\frac{\mathbf{y}(n) - \mathbf{y}(n-1)}{T_s} = -(\omega_{1/2} - j\triangle w)\mathbf{y}(n-1) + \omega_{1/2}\mathbf{u}(n). \tag{5.7}$$

$$\mathbf{G}_C(z) = \frac{T_s\omega_{1/2}}{1 - z^{-1}[1 - T_s(\omega_{1/2} - j\triangle w)]}. \tag{5.8}$$

As an example we simulated a cavity transfer function having 200Hz of cavity half bandwidth, cavity detuning equal to cavity half bandwidth and the sampling frequency of 1Mhz. With the inverse z-transform of $G_C(z)$, the impulse response of the cavity can be computed by Equation 5.9. The cavity's impulse response magnitude and phase are plotted in Figure 5.2 and Figure 5.3 respectively.

$$\mathbf{h}(n) = T_s\omega_{1/2}[1 - T_s(\omega_{1/2} - j\triangle w)]^n \qquad n = 0, 1, 2, ... \tag{5.9}$$

5.2.1   P-Type ILC

P-type ILC, also known as proportional-type ILC, is a type of iterative learning control (ILC) that is based on the proportional control principle. In P-type ILC, the learning function is proportional gain, which is a tuning parameter. The idea is to adjust the
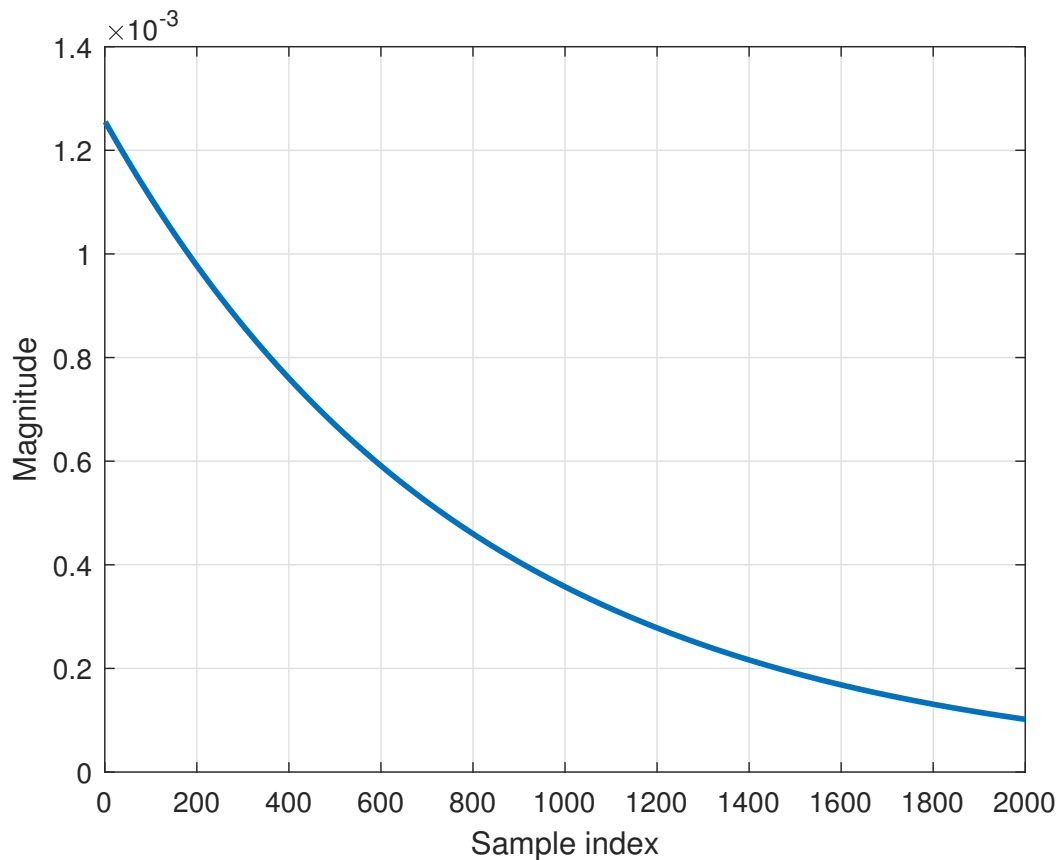
FIGURE 5.2: Impulse Response Magnitude, sampling time $1\mu sec$.

control input in each iteration based on the error in the previous iteration so that the system's performance improves over time [99]. One of the benefits of P-type ILC is that it is simple and easy to implement, making it a popular choice for many applications. However, it may not be as effective as other types of ILC when dealing with complex systems or tasks that require more sophisticated control strategies.

5.2.2 Higher Order ILC

Higher-order ILC is a type of iterative learning control (ILC) that uses higher-order models to improve the performance of a system. In traditional ILC, a first-order model is used to capture the dynamics of the system being controlled. However, in some cases, the system's behavior cannot be accurately represented by a first-order model, and a higher-order model is needed. Higher-order ILC can be implemented in various ways, such as through the use of higher-order differential equations or by using state-space models. The main idea is to capture the higher-order dynamics of the system being
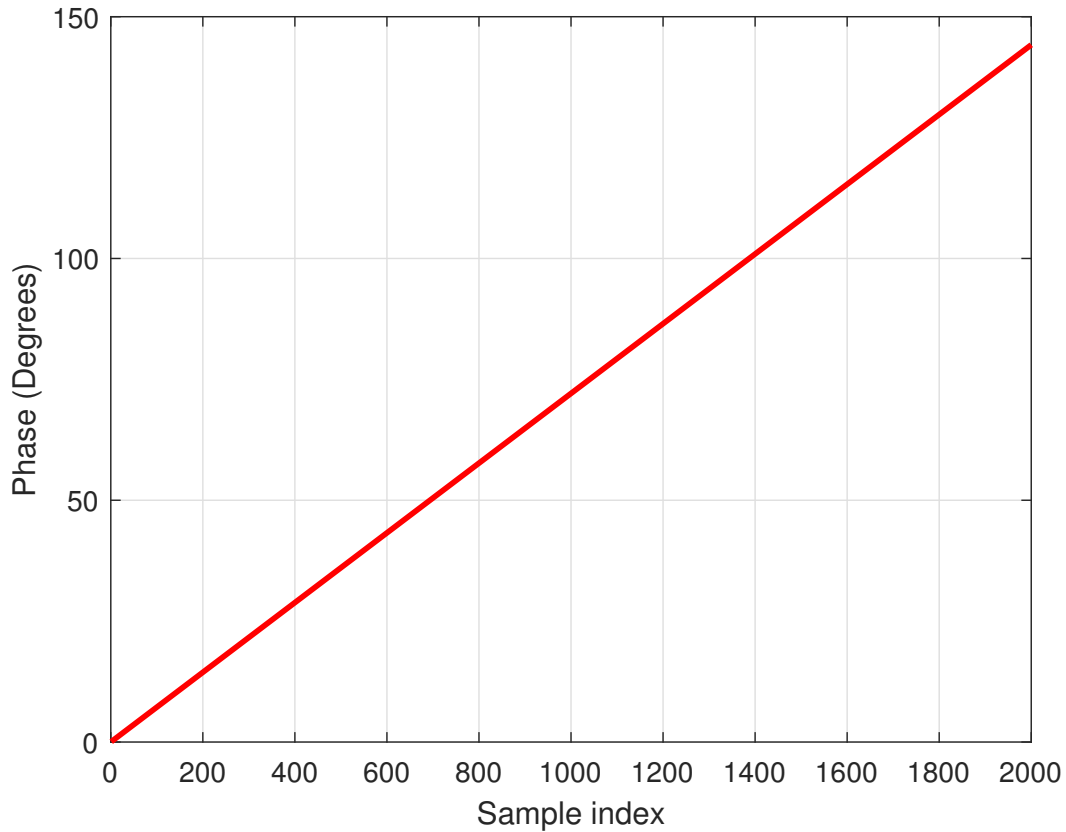
FIGURE 5.3: Impulse Response Phase, sampling time $1\mu sec$.

controlled and use this information to develop a more accurate control law. One of the benefits of higher-order ILC is that it can be used to control systems with complex dynamics, such as flexible structures or nonlinear systems. However, it can be more challenging to implement and may require more computational resources compared to traditional first-order ILC.

5.2.3 H_∞ based ILC

H_∞ based ILC is a type of iterative learning control (ILC) that is based on the H_∞ control theory. H-infinity control is a robust control method that is used to design controllers that are robust to uncertainties and disturbances in the system.

In H_∞ based ILC, the control law is designed to minimize the H_∞ norm of the error between the desired output and the actual output of the system. The H_∞ norm is a measure of the worst-case disturbance that the system can tolerate while still meeting its performance specifications.

The advantage of using H_∞ based ILC is that it provides a robust and optimal control strategy that is effective in handling uncertainties and disturbances in the system. This makes it a popular choice for systems with uncertain or varying dynamics, such as flexible structures or robotic systems.

However, H_∞ based ILC can be more complex and computationally intensive than other types of ILC and may require more careful tuning of the controller parameters. It is important to carefully consider the advantages and limitations of H_∞ based ILC before choosing the most appropriate type of ILC for a given application.

5.2.4 Plant inversion based ILC

Plant inversion-based ILC is a type of iterative learning control (ILC) that is based on the principle of plant inversion [99]. The idea behind plant inversion is to design a feedback controller that inverts the dynamics of the plant being controlled so that the feedback loop behaves as if the plant were an ideal unit.

In plant inversion-based ILC, the control law is designed by inverting the plant model and then using this inverted model to calculate the control input in each iteration. The inversion process involves finding a mathematical function that relates the desired output to the control input, based on the known dynamics of the plant.

The advantage of using plant inversion-based ILC is that it can provide accurate and fast control for systems with simple dynamics, such as those with linear time-invariant (LTI) models. However, it may not be as effective for systems with more complex dynamics, or those that are subject to uncertainties or disturbances.

Plant inversion-based ILC can be a powerful tool for improving the performance of systems with simple dynamics, but it may not be appropriate for more complex systems. It is important to carefully consider the advantages and limitations of plant inversion-based ILC before choosing the most appropriate type of ILC for a given application.

5.2.5 Norm Optimal ILC

Optimization-based ILC is a type of iterative learning control (ILC) that is based on optimization techniques to design the control law. The control law is formulated as an
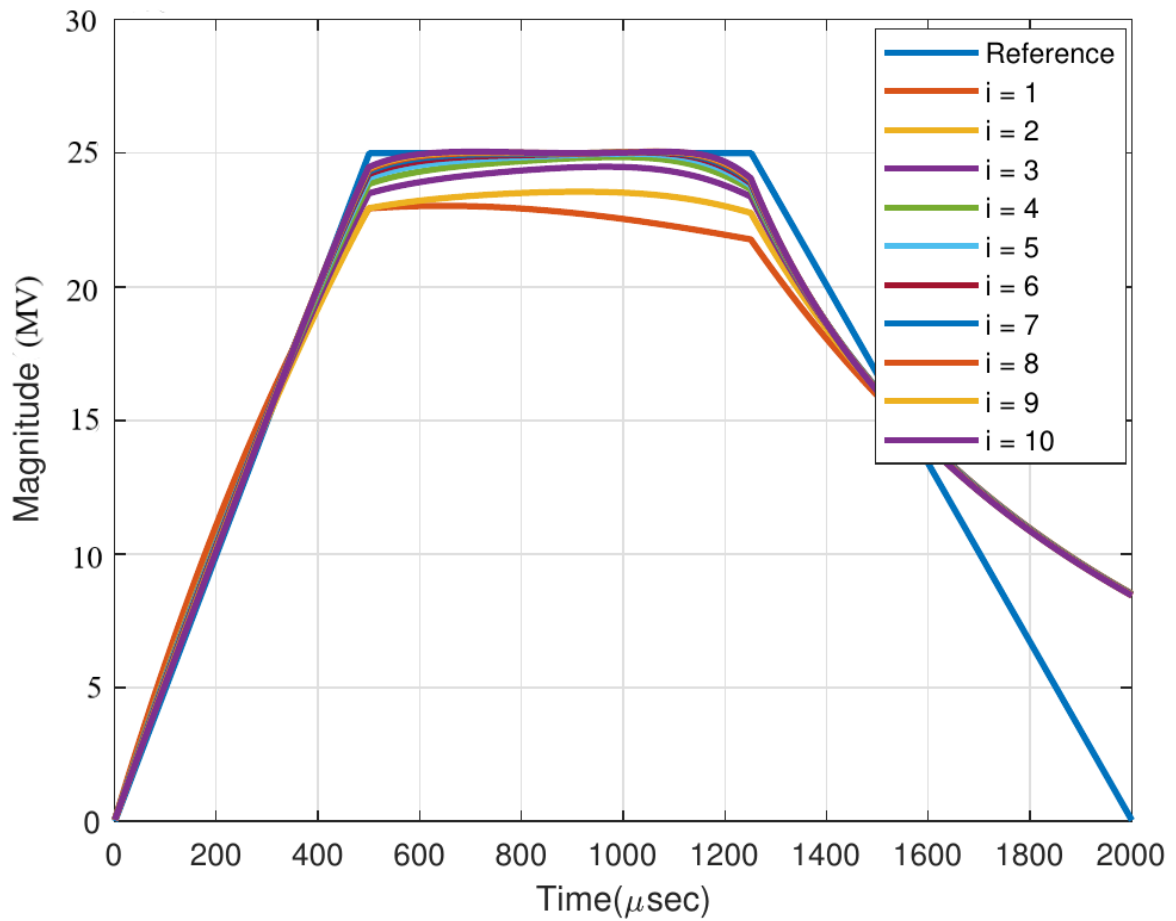
FIGURE 5.4: Cavity Voltage Magnitude for iteration i=1 to 10 in ILC Algorithm

optimization problem, where the objective is to minimize a cost function that represents the error between the desired output and the actual output of the system. The optimization problem is typically subject to constraints that represent the limitations of the system, such as control input limits or physical constraints on the system. The solution to the optimization problem provides the optimal control input for each iteration of the ILC process.

The advantage of using optimization-based ILC is that it provides a flexible and powerful tool for designing control laws that can handle a wide range of systems and performance requirements. It can also be used to incorporate different types of constraints and objectives into the control law.

However, optimization-based ILC can be computationally intensive and may require careful tuning of the optimization algorithm and cost function to achieve good performance. It is also important to ensure that the optimization problem is well-posed and that the solution is feasible and stable.
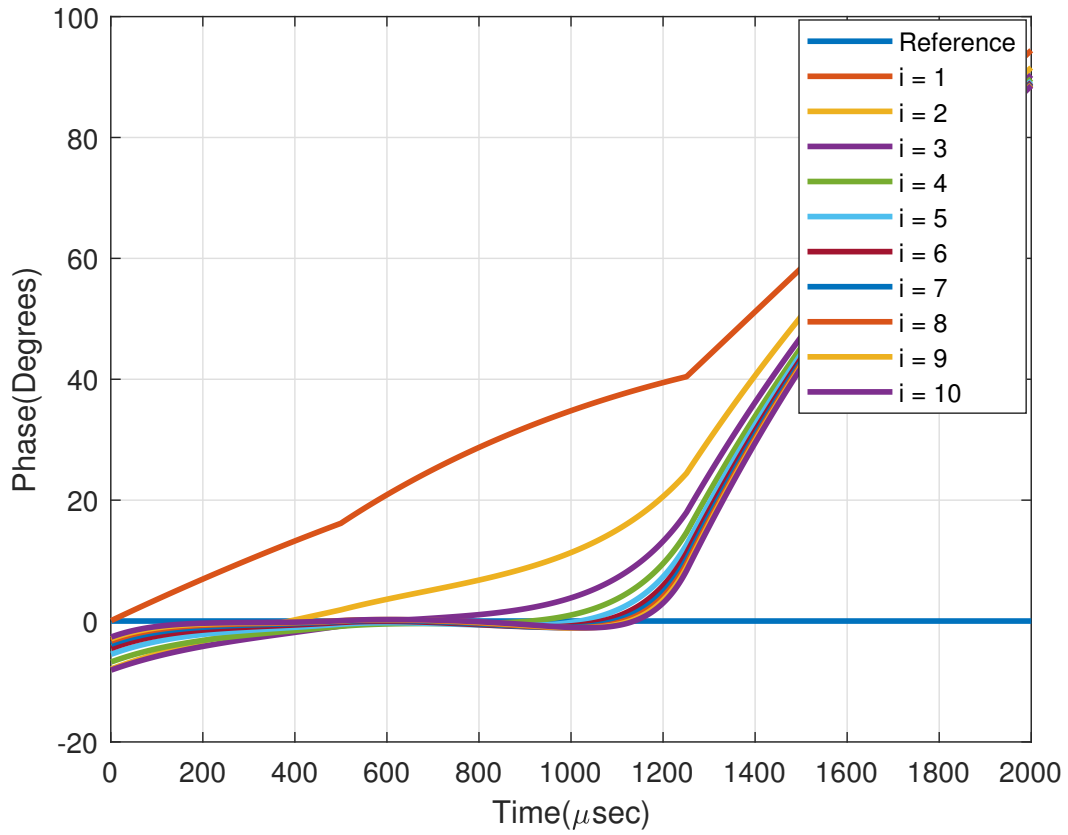
FIGURE 5.5: Cavity Voltage Phase in for iteration i=1 to 10 in ILC Algorithm
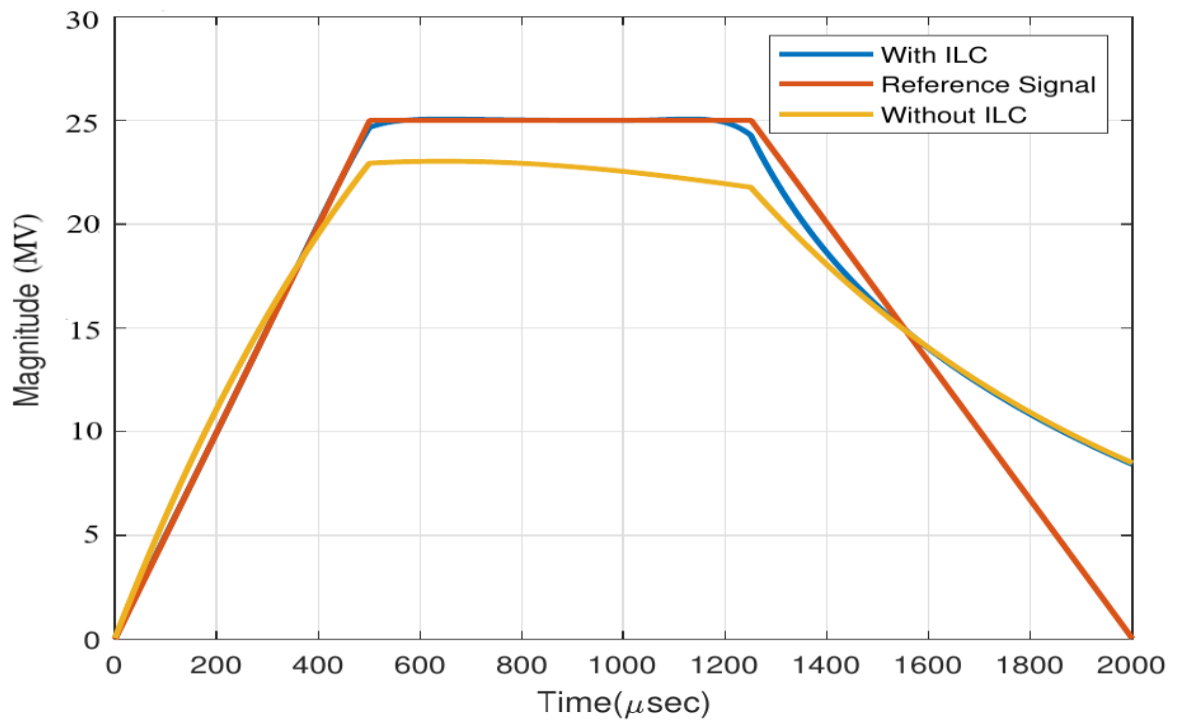
FIGURE 5.6: Cavity Voltage Magnitude After 20 iterations of ILC compared with reference and without ILC
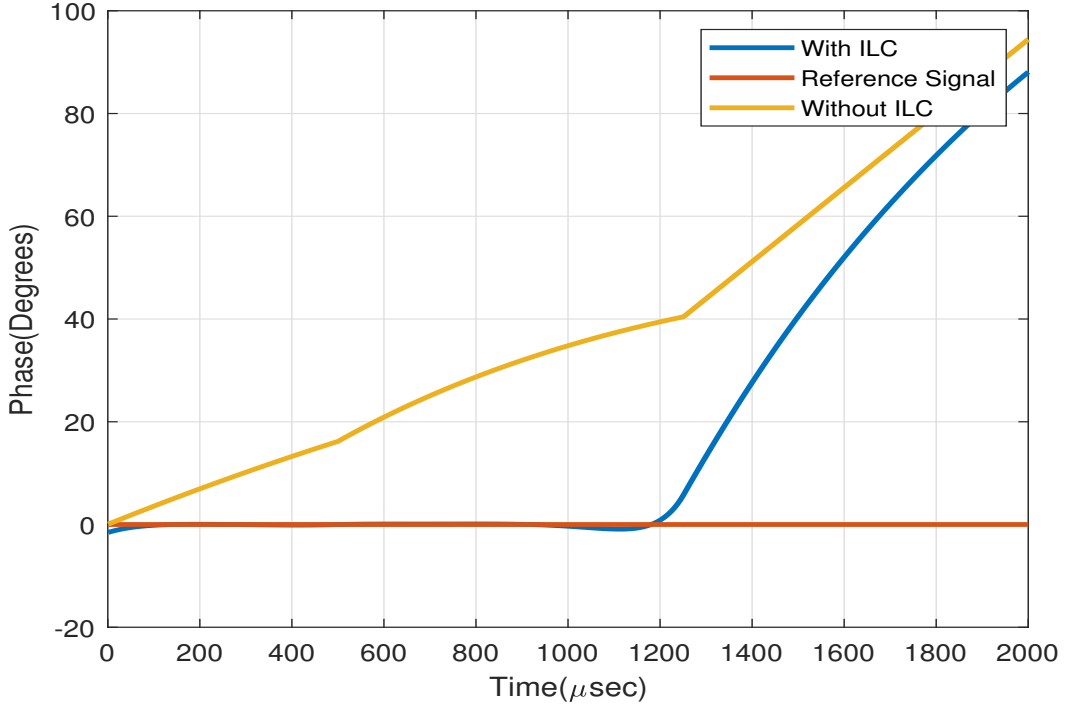
FIGURE 5.7: Cavity Voltage Phase After 20 iterations of ILC compared with reference and without ILC

Optimization-based ILC can be a powerful tool for designing control laws that can handle a wide range of systems and performance requirements, but it may require more computational resources and careful tuning compared to other types of ILC.

Given the known vectors u_j and y_j obtained from the measurement of the jth pulse, our objective is to find a new drive vector u_{j+1}, that minimizes the output error of the $(j+1)^{th}$ pulse while avoiding significant changes in the drive signal. By using the positive definite weight matrices $\mathbf{P}$ and $\mathbf{Q}$, the cost function J for this problem can be formulated as

$$J = \mathbf{e}_{j+1}^{H}\mathbf{P}\mathbf{e}_{j+1} + \triangle\mathbf{u}_{j+1}^{H}\mathbf{Q}\triangle\mathbf{u}_{j+1}. \tag{5.10}$$

where H represents the conjugate transpose of a vector, the tracking error vector for the $(j+1)^{th}$ pulse is given by

$$\mathbf{e}_{j+1} = \mathbf{r} - \mathbf{y}_{j+1} \approx \mathbf{r} - \mathbf{y}_j - \mathbf{G}\triangle\mathbf{u}_{j+1}. \tag{5.11}$$

The alterations made to the drive signal, correspond to the feedforward correction signal is

$$\triangle\mathbf{u}_{j+1} = \mathbf{u}_{j+1} - \mathbf{u}_j. \tag{5.12}$$

To minimize J, the gradient of J with respect to $\mathbf{u}_{j+1}$ should be zero, which leads to the condition $\nabla_{\mathbf{u}_{j+1}} J = 0$. This condition determines the solution for $\mathbf{u}_{j+1}$ as

$$\mathbf{u}_{j+1} = \mathbf{u}_j + (\mathbf{Q} + \mathbf{G}^H \mathbf{P} \mathbf{G})^{-1} \mathbf{G}^H \mathbf{P} \mathbf{e}_j. \tag{5.13}$$

Comparing the above equation with Equation 6.1 resulted in

$$\mathbf{L} = (\mathbf{Q} + \mathbf{G}^H \mathbf{P} \mathbf{G})^{-1} \mathbf{G}^H \mathbf{P}. \tag{5.14}$$
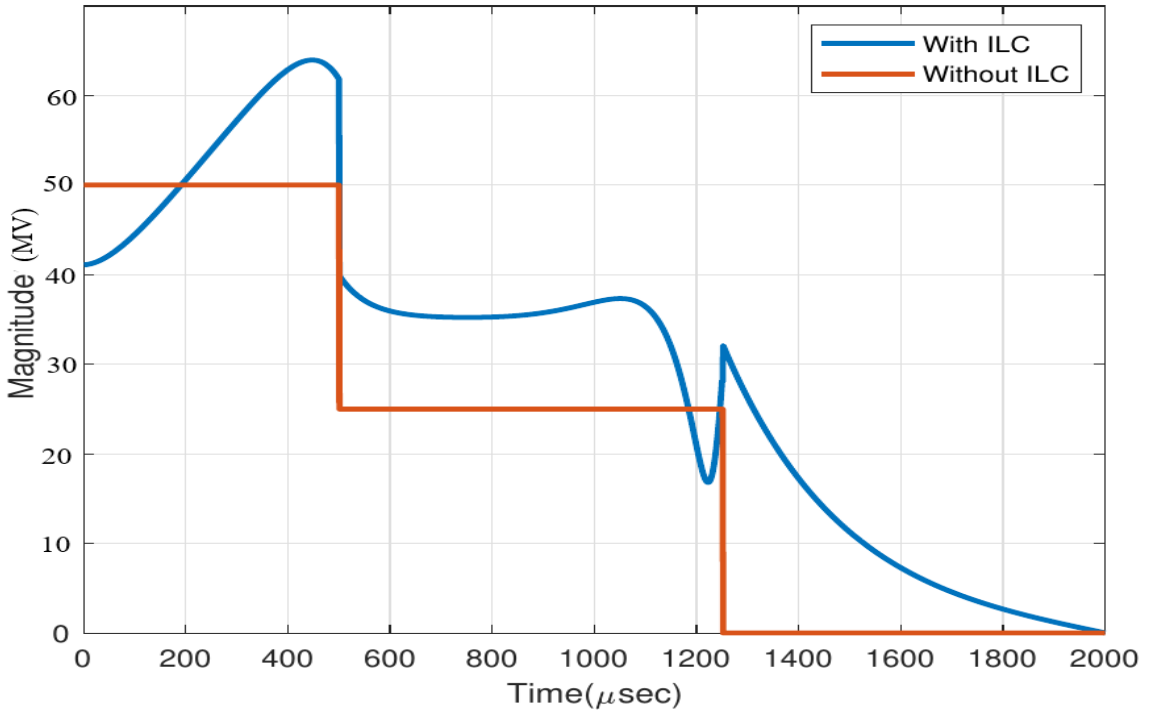
FIGURE 5.8: Control Input Magnitude

5.2.6   Results and Discussion

We simulated norm optimal iterative learning control for the cavity field control problem. The performance of the algorithm is dependent on the choice of matrices $\mathbf{P}$ and $\mathbf{Q}$. Which are often chosen empirically [60]. To maintain stability, we restrict the utilization of the feedforward correction to a fraction. Consequently, we introduce a smaller gain, which is multiplied by the feedforward correction signal in the ILC law Equation 5.13.
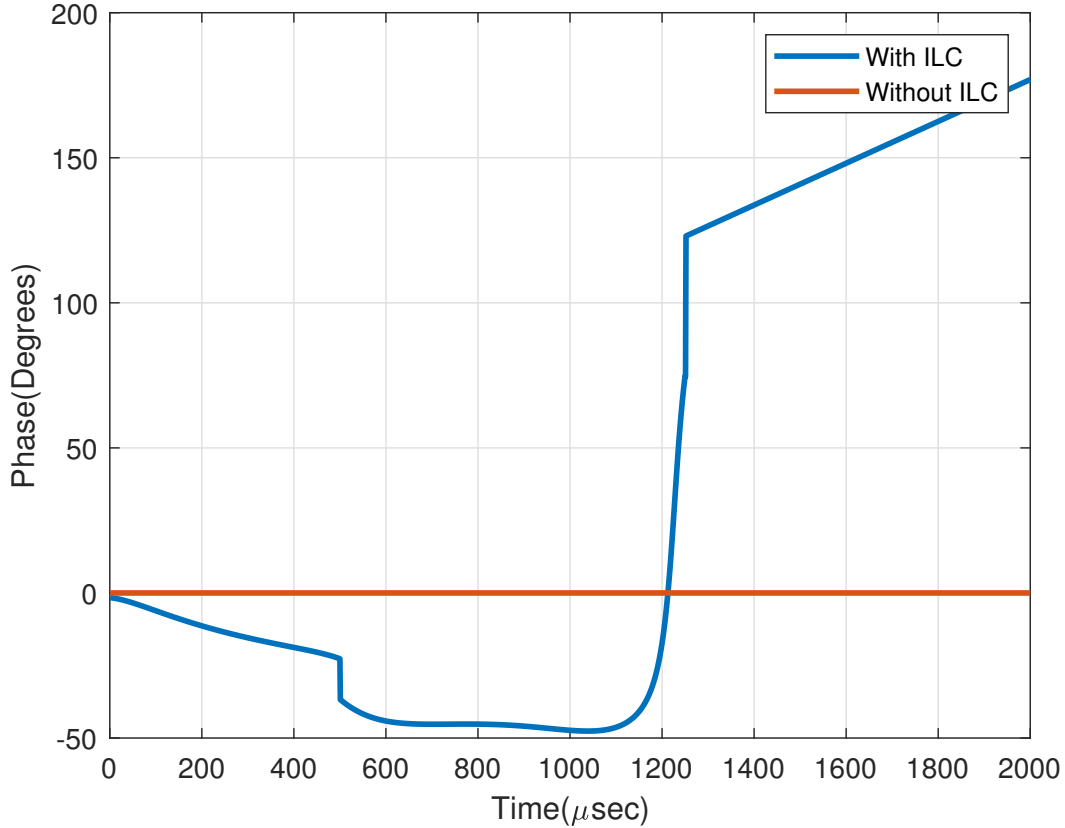
FIGURE 5.9: Control Input Phase

We simulated the FIR cavity model transfer function as described in section 5.2, the matrices **P** and **Q** are chosen as diagonal matrices with elements 10 and 1 respectively. The cavity voltage magnitude and phase from 1st to 10th iteration are plotted in Figure 5.4 and Figure 5.5 respectively. It is evident from these results that as the number of iterations is increased the cavity voltage magnitude and phase approaches to the reference set point values so tracking of the reference is improved significantly. At the falling edge of RF pulse after about $1200\mu sec$ the tracking error in magnitude and phase of cavity voltage is increased, this will not affect the beam quality as the charge article beam is introduced during the flat top of RF pulse. furthermore the cavity voltage pulse rising and falling are exponential that's why it does not follow the ramp rising and falling reference signal.

Results of norm optimal ILC after 20 iterations are shown in Figure 5.6 and Figure 5.7 to further elaborate the improvement in reference tracking. For this improvement the Control input magnitude and phase with and without norm optimal ILC are plotted in Figure 5.8 and Figure 5.9 respectively. For ease of simulation, we have used a ramp

rising edge for the reference pulse so the control input has a higher magnitude during the rising edge before $450\mu sec$ or cavity filling time, for exponential rising in the reference signal the control input magnitude would be lower. So actually we would not require much overhead in control input for improved magnitude and phase stability during flat top.

The discussed control algorithm can be used for klystron field flattening by iteratively modifying the magnitude and phase of klystron drive input signal according to the control input computed.

One of the major limitation of this algorithm is that it is highly dependent on the accurate modeling of the accelerating cavity. As the cavity model is changed the required control input must be modified accordingly. Therefore runtime system identification is required if system model is changing randomly. Since beam loading and cavity detuning are predictable disturbances, so set of cavity models would be available in the control card for modified control input generation.

5.3   Summary

In this chapter, different types of ILC algorithms are briefly described including Proportional type ILC, Higher order ILC, Plant inversion based ILC, H_∞ based ILC and norm optimal ILC. The norm optimal ILC algorithm with FIR model cavity is simulated and results are presented. The tracking of set point cavity voltage magnitude and phase are improved as the number of iterations are increased. The performance of the algorithm is dependent on the choice of weighting matrices which are chosen empirically, this area needs more research. Furthermore, the simulated plant transfer is dependent on cavity detuning and during the pulse, the cavity detuning is changed so a set of plant transfer functions for a set of detuning values would provide the more optimized control input to minimize error in reference tracking in more realistic time-varying plant transfer function. A combination of iterative learning control and disturbance observer-based control may enhance the performance.

In the next chapter High pulsed power magnetron frequency control for for particle accelerators is presented.

Chapter 6

Magnetron Frequency Control

Microwave power source frequency stability is crucial for consistent and precise field control in the accelerator cavity. Any controller whether it is a disturbance observer, iterative learning, OR conventional PI controller, its performance is severely affected if the microwave power source frequency is not stable. Klystrons are much more robust in terms of frequency stability as compared to magnetrons but magnetrons are very cost-effective and have some other advantages as described in section 3.9.2. In this Chapter frequency control of a high pulsed power magnetron is explored in detail and since the superconducting cavity and cryogenic system was not available we did experiments with a normal conducting cavity with unusual narrow mode spacing.

High pulsed power Magnetrons are commonly employed as RF power sources in medical linear accelerators. One notable example is the MG5193 magnetron depicted in Figure 6.1, which is used as an RF power source in S-band electron accelerators. The operating conditions for this magnetron, as outlined in the datasheet, are illustrated in Figure 6.2. This figure readily indicates that the magnetron functions as a dynamic load, with its output power and frequency contingent upon several parameters. They offer advantages such as compact size, reduced costs, and lower operating voltages compared to Klystrons. However, they do come with drawbacks, including frequency drift and random phase variations in each pulse. These limitations can hinder their application in beamlines within large particle accelerator projects where multiple RF sources power numerous cavities. The magnetron is a type of cross-field vacuum tube. Within the magnetron, the magnetic field runs perpendicular to the plane formed by the cathode and anode
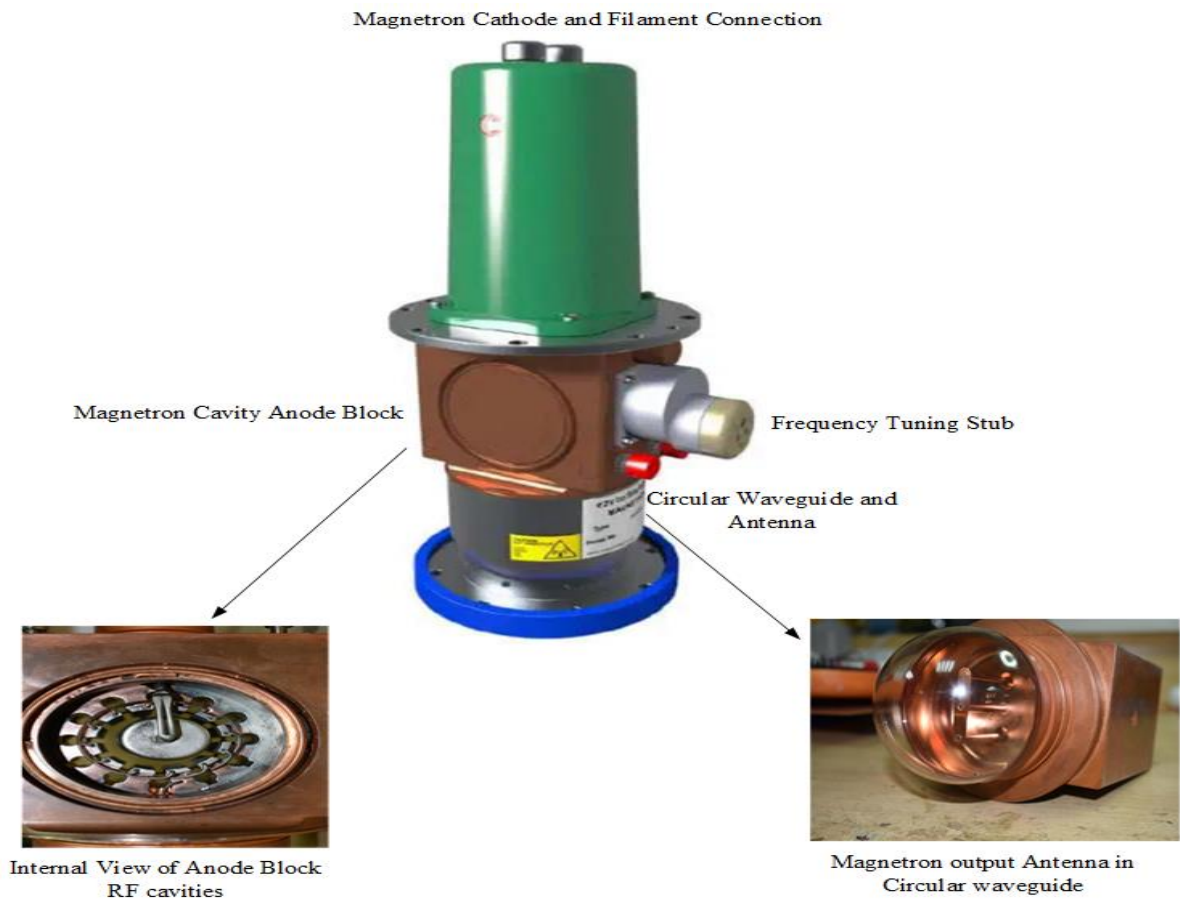
FIGURE 6.1: S-band Magnetron and its internal structure

cavities. As electrons are emitted from the cathode, they are propelled towards the anode block by the substantial negative accelerating potential. However, owing to the perpendicular magnetic field, these electrons, which initially move radially outward, are compelled to follow a circular trajectory within the space situated between the cathode and anode.

6.0.1 Sources of Frequency Variation in Magnetron

The frequency change of the magnetron depends on the following parameters, as depicted in Figure 6.3.

1. Magnetic Field (change in electromagnet power supply current).

2. Frequency Pushing, Magnetron Current change.

3. Frequency Pulling, Reflected power to the magnetron from the mismatched microwave load.

4. Magnetron Cathode temperature.
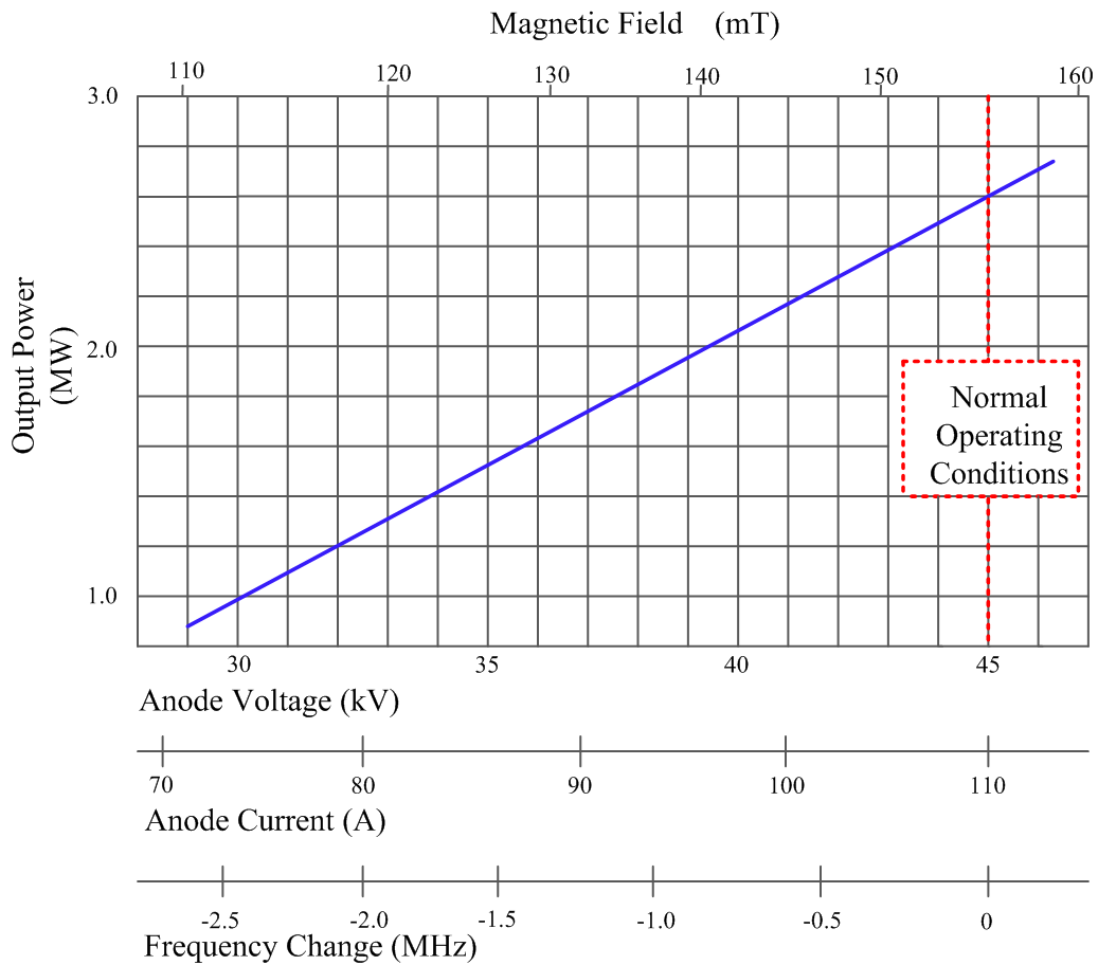
FIGURE 6.2: MG5193, Load line and corresponding Electromagnet magnetic field and frequency variation for full range of output power

6.0.1.1 Magnetic Field

To adjust the power levels of the magnetron, variations in the magnetron input voltages are made alongside adjustments to the corresponding magnetic field. This ensures that the magnetron operates within a constant impedance line. As part of this process, the magnetron's output frequency is also modified. The load line for the pulsed magnetron MG5193 is depicted in Figure 6.2. To fine-tune the magnetron frequency, a tuning stub is employed, allowing for precise adjustment of the magnetron's output frequency to the desired value.

6.0.1.2 Magnetron Current Change

The change in magnetron current also causes the change in magnetron output frequency. This phenomenon is called magnetron pushing. For stable frequency operation, the
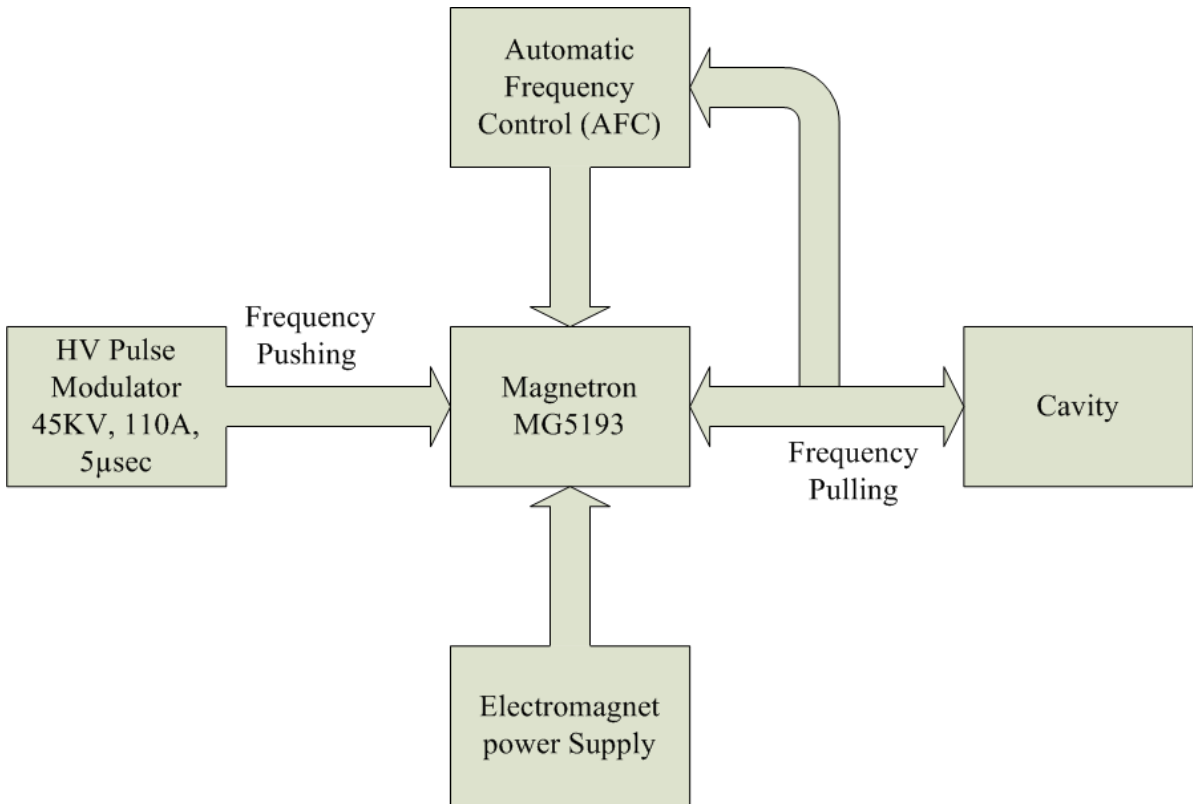
FIGURE 6.3: Factors on which Magnetron Frequency Depends

current should be maintained constant. Due to imperfections in the pulse modulator output or the overheating of the magnetron cathode, the magnetron current may change causing a change in the magnetron output frequency. This phenomenon may occur within the magnetron RF pulse or from pulse to pulse. To maintain the temperature of the magnetron cathode to a certain limit the cathode filament voltages are gradually decreased with increasing magnetron pulse rate and at a certain threshold input average power the filament is turned off, as mentioned in the magnetron datasheet or application notes. The magnetron injection locking can also be used to avoid frequency shifts in magnetron output. In injection locking a low-power RF signal is injected into the magnetron to lock the magnetron output frequency with the injected signal frequency.

6.0.1.3 Power Reflected from load

The magnetron is sensitive to the reflected power from the mismatched load. This not only changes the magnetron output frequency but also the high reflected power can cause arcing inside the magnetron. For stable operation of the magnetron, the circulator and isolator are used between the magnetron and the load. The change in

frequency of the magnetron depends on the phase and magnitude of the reflected signal. The Reike diagram of magnetron 725A taken from [100] is shown in Figure 6.4. A Rieke diagram depicts the load characteristics of an oscillator on a Smith chart. It typically comprises two sets of curves: one indicating constant power levels and the other indicating constant frequency levels, here these curves are represented by red and green colors respectively. The mathematical polynomials representing these contours for a pure sinusoidal oscillator are described by Katsumi et al [101]. The magnetron frequency is increased or decreased based on the phase of the reflected signal as it varies $\pm 90\,$deg. It can also be noted that the output power is changed when the reflected power has phase $\pm 180\,$deg.

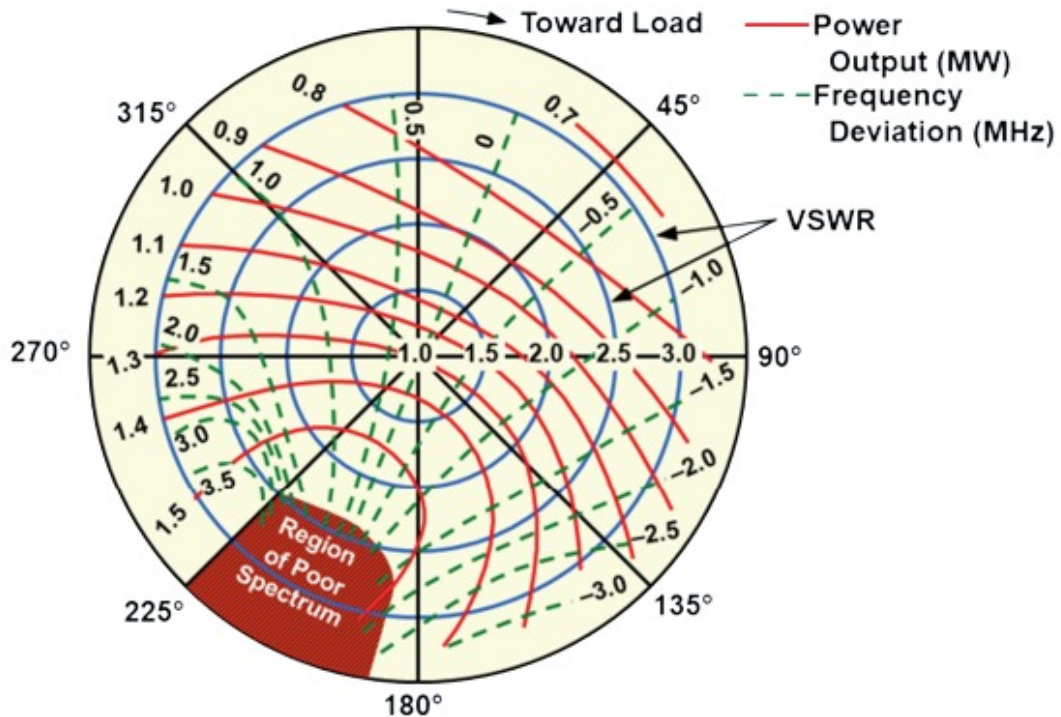FIGURE 6.4: Reike diagram of a Magnetron, elaborating effect of load on Magnetron output power and frequency [102]

6.0.1.4   Magnetron Cathode Temperature

For stable operation of magnetron the magnetron cathode temperature is very important. When a magnetron is operated at a higher duty cycle or higher repetition rate, due to the back bombardment of electrons to the cathode its temperature is increased

therefore the filament voltages are gradually decreased. In MG5193 the filament voltage scheduling is done based on average input power to the magnetron. At higher temperature magnetron arcing is occurred, which shorten its operating life. Magnetron anode is water cooled and usually operated at around 40 degree centigrade of cooling water temperature. At lower or higher water temperature not only the magnetron operating frequency and bandwidth is shifted.

6.0.2 Automatic Frequency Control of Magnetron

In ideal conditions, RF source frequency and cavity resonance frequency are the same, but if the cavity is slightly off-resonance then RF source frequency can be adjusted to operate the accelerating cavity at resonance. The decision to increase or decrease the source frequency can be made by the algorithm described in Figure 6.5, usually applied in medical LINACs. The directional couplers on the feeding waveguide transmit both forward and reflected signals, which are then routed to the quadrature hybrid. One signal takes a direct path, while the other is adjusted using a variable phase shifter before entering the quadrature hybrid. The quadrature hybrid has two outputs one is the sum of input signals and the other is the difference of input signals. these output signals are passed through identical diode detectors to get their DC magnitude envelopes 'A' and 'B'. The difference between 'A' and 'B' is maintained near to zero at resonance by adjusting the phase shifter at quadrature hybrid input. Once the zero value is obtained the phase shifter is locked. When the cavity resonance frequency is shifted the difference between signal 'A' and 'B' would be either positive or negative indicating that RF source frequency should be increased or decreased to operate the cavity at resonance. In the MG5193 S-band magnetron, there exists a tuning stub within the anode cavity block, depicted in Figure 6.1. This tuning stub serves the purpose of frequency adjustment. The tuning stub is connected to a motor, whose driver card receives feedback from the AFC module to precisely adjust the frequency of the magnetron.

To tune the AFC loop, the process begins with operating the magnetron tuner motor in an open loop configuration while observing the forward and reflected signals on the scope. The tuner motor is adjusted until the optimal condition is achieved, typically indicated by minimizing the reflected signal. The reflected signal is not minimized to zero,

but when the electron beam is switched on, this reflected signal will further decrease. After achieving optimal reflected power, the phase shifter within the AFC tuning box is fine-tuned to minimize the error signal resulting from the difference between AFC outputs 'A' and 'B', aiming for near-zero deviation. Once this adjustment is made, the phase shifter is locked into position, effectively closing the AFC loop. By closing the AFC loop, the system gains the ability to continuously monitor and adjust its frequency, ensuring stability and accuracy over time. The close loop block diagram of automatic frequency control of RF source is presented in Figure 6.6, as described in the SIEMENS service training manual for medical linear accelerators [77].

6.0.3   Injection Locking of Magnetron

The AFC loop of the Magnetron operates relatively slowly due to the mechanical motor tuner. However, its frequency tuning range is significantly higher. For instance, in the case of MG5193, the magnetron's output frequency can be varied from 2992 to 3002MHz using the mechanical tuner. When the magnetron operates near the resonance frequency of the accelerator cavity, typically within a $\pm 0.5 MHz$ offset, injection locking of the magnetron can be employed [103]. Injection locking provides a fast frequency control compared to the AFC loop. In self-injection locking, a small portion of the reflected power is fed back to the magnetron. For the derivation of the injection locking frequency range consider the equivalent circuit of magnetron oscillator with injection current source I_{inj} in Figure 6.7. applying the Kirchhoff's current law on the node mentioned we can get the equation

$$
\begin{aligned}
C\frac{dV}{dt} + \frac{1}{L}\int V dt + \frac{V}{R} - \frac{V}{Z_m} + \frac{V}{R_L} &= I_{inj}, \\
\frac{d^2V}{dt^2} + \left(\frac{1}{RC} + \frac{1}{R_LC} - \frac{1}{Z_mC}\right)\frac{dV}{dt} + \frac{1}{LC}V &= \frac{1}{C}\frac{dI_{inj}}{dt}.
\end{aligned}
\tag{6.1}
$$

For the derivation of the injection locking range of frequency, we use the injection signal and oscillator output voltage in exponential form as

$I_{inj} = I_o e^{\omega_{inj}t}$ and $V = V_o(t)e^{\omega_{inj}t+\theta(t)}$,

where, I_o is the injection current magnitude, $V_o(t)$ is the oscillator output envelop voltage and $\theta(t)$ is the output phase modulation due to the injection signal. The second and

$$\vec{V_f} + \vec{V_r} = \vec{A}$$

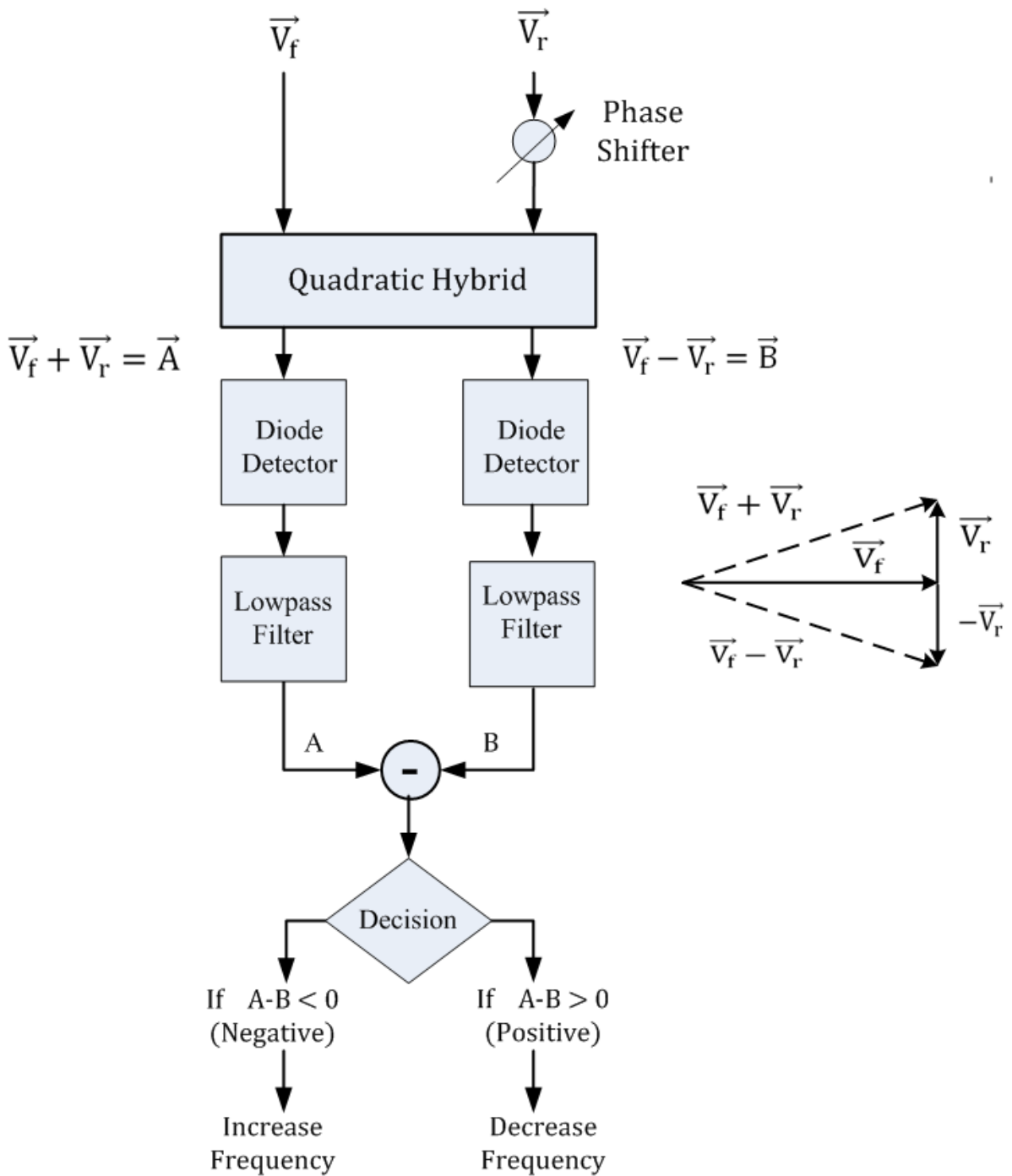$$\vec{V_f} - \vec{V_r} = \vec{B}$$

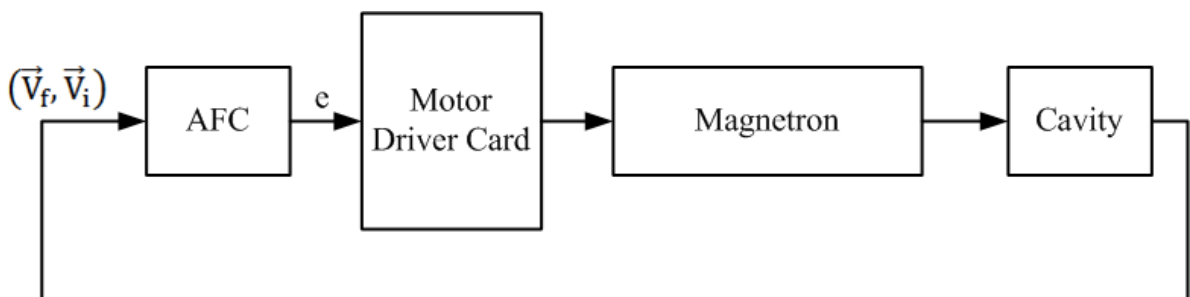FIGURE 6.5: Automatic Frequency Control (AFC) of RF source

FIGURE 6.6: AFC loop for frequency control of magnetron [77].
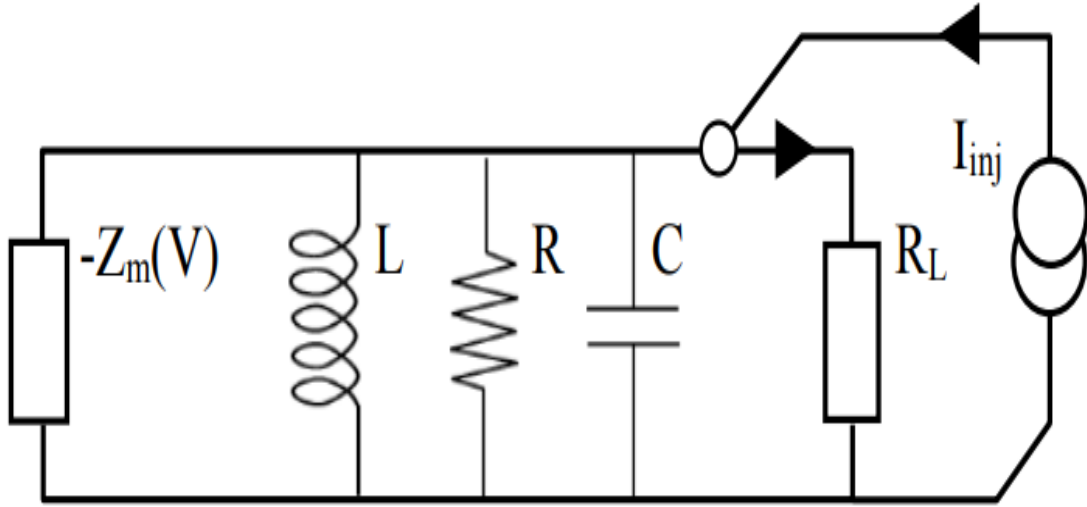
FIGURE 6.7: Magnetron Circuit Model with injection locking

first derivative terms in 6.1 would be

$$\frac{dI_{inj}}{dt} = j\omega_{inj}I_o e^{j[\omega_{inj}t+\theta(t)]}.e^{-j\theta(t)}$$

$$\frac{dV}{dt} = e^{j[\omega_{inj}t+\theta(t)]}\left[\frac{dV_o}{dt} + j\left(\omega_{inj} + \frac{d\theta}{dt}\right)V_o(t)\right]$$

$$\frac{d^2V}{dt^2} = e^{j[\omega_{inj}t+\theta(t)]}\left[j\left(\omega_{inj} + \frac{d\theta}{dt}\right)\left[\frac{dV_o}{dt} + j\left(\omega_{inj} + \frac{d\theta}{dt}\right)V_o(t)\right]+\right.$$
$$\left.\left[\frac{d^2V_o}{dt^2} + j\left(\omega_{inj} + \frac{d\theta}{dt}\right)\frac{dV_o(t)}{dt} + j\frac{d^2\theta}{dt^2}V_o(t)\right]\right]$$

By using the above expressions in Equation 6.1 we get

$$\left[\frac{d^2V_o}{dt} + j\frac{d^2\theta}{dt}V_o(t) + 2j\left(\omega_{inj} + \frac{d\theta}{dt}\right)\frac{dV_o(t)}{dt} - \left(\omega_{inj} + \frac{d\theta}{dt}\right)^2V_o(t)\right]$$
$$+ \frac{1}{LC}V_o(t) + \left[\frac{1}{RC} + \frac{1}{R_LC} - \frac{1}{Z_mC}\right]\left[\frac{dV_o}{dt} + j\left(\omega_{inj} + \frac{d\theta}{dt}\right)V_o(t)\right]$$
$$= \frac{\omega_{inj}}{C}I_o(sin\theta + jcos\theta). \tag{6.2}$$

By equating the real and imaginary parts of the above equation it can be shown

$$\left[\frac{d^2V_o}{dt^2} - \left(\omega_{inj} + \frac{d\theta}{dt}\right)^2V_o(t)\right] + \left[\frac{1}{RC} + \frac{1}{R_LC} - \frac{1}{Z_mC}\right]\frac{dV_o}{dt} +$$
$$\frac{1}{LC}V_o(t) = \frac{\omega_{inj}}{C}I_osin\theta. \tag{6.3}$$

$$2\left(\omega_{inj} + \frac{d\theta}{dt}\right)\frac{dV_o}{dt} + \left[\frac{1}{RC} + \frac{1}{R_L C} - \frac{1}{Z_m C}\right]\left(\omega_{inj} + \frac{d\theta}{dt}\right)V_o(t)+$$
$$\frac{d^2\theta(t)}{dt^2}V_o(t) = \frac{\omega_{inj}}{C}I_o cos\theta. \tag{6.4}$$

To simplify the equations, the following assumptions are made

(i) $V_o(t)$ and $\theta(t)$ are varying slowly resulting in $\frac{1}{V_o(t)}\left(\frac{dV_o}{dt}\right) << 1$ and $\frac{1}{\omega_o}\left(\frac{d\theta}{dt}\right) = 1$, where $\omega_o = \frac{1}{\sqrt{LC}}$.

(ii) The envelope voltage magnitude maximum value is equal to the peak oscillator current I_{osc} times Resistance R. Since $Q = \dfrac{R}{\omega_o L}$, we can write

$max(V_o) = I_{osc} * R = I_{osc} * Q\omega_o L$

(iii) $\omega_o \approx \omega_{inj}$ and $\omega_o^2 - \omega_{inj}^2 \approx 2\omega_o(\omega_o - \omega_o)$

Using the above-mentioned approximations the Equation 6.3 will reduce to

$$\frac{d\theta}{dt} = \omega_o - \omega_{inj} - \frac{\omega_o I_o}{2QI_{osc}}sin\theta. \tag{6.5}$$

This is the famous Adler's equation. At steady state $\frac{d\theta}{dt} = 0$ and maximum value of $sin\theta = 1$, resulting in the maximum range of frequency for which oscillator can be locked, given by

$$\omega_o - \omega_{inj} = \frac{\omega_o}{2Q}\frac{I_o}{I_{osc}}. \tag{6.6}$$

The locking range of the oscillator depends on the injection signal amplitude, the output signal strength, the quality factor of the oscillator, and its natural resonance frequency ω_o. The loaded quality factor Q needs to be computed at the operating point for determination of locking range [76].

6.0.4 Experimental Setup

To power a 6 MeV standing wave cavity we utilized MG5193 magnetron operated with HV pulse modulator with specs 48KV, 110A and $5\mu sec$ pulse width and rep-rate up to 250Hz. The microwave transmission scheme is through four ports circulator and shut T to RF cavity and water load. The experimental setup is shown in Figure 6.8. We utilized an 11-cell side-coupled, standing wave cavity designed for a 6 MeV LINAC. The accelerating mode in this cavity is $\pi/2$-mode. In $\pi/2$-mode the field in consecutive cells is at $\pi/2$ phase, and since each on-axis cell is connected to a side cell, so two adjacent on-axis cells will have π or 180 deg phase difference in electric field. The electric field

simulated in CST microwave studio for the $\pi/2$ and the immediate next neighboring mode are presented in Figure 6.9 and Figure 6.10 respectively. Unfortunately, im-
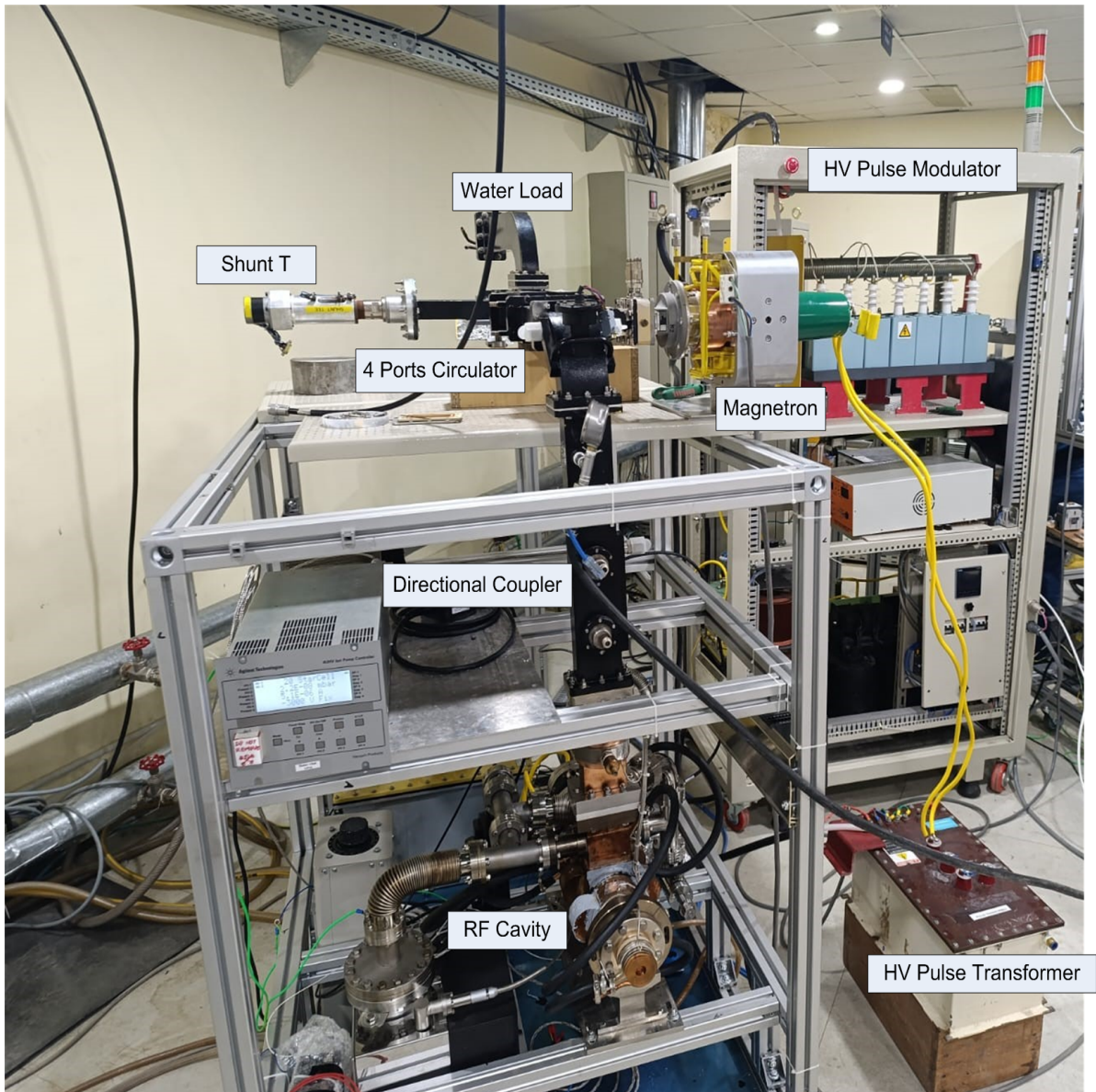
FIGURE 6.8: Experimental Setup for high power microwave operation of 6MeV standing wave cavity

perfections in the brazing or machining processes during the construction of the said cavity, resulted in a very narrow mode spacing between the accelerating $\pi/2$-mode and its immediate neighboring mode. Additionally, the coupling of the desired $\pi/2$-mode was minimal, measuring approximately -6.54 dB, as illustrated in Figure 6.11. To rectify this issue, we placed a ceramic bead on the waveguide window on the high-pressure SF_6 side, resulting in a notable increase in the coupling of the accelerating mode to approximately -10.8 dB. However, this adjustment led to the merging of the immediate
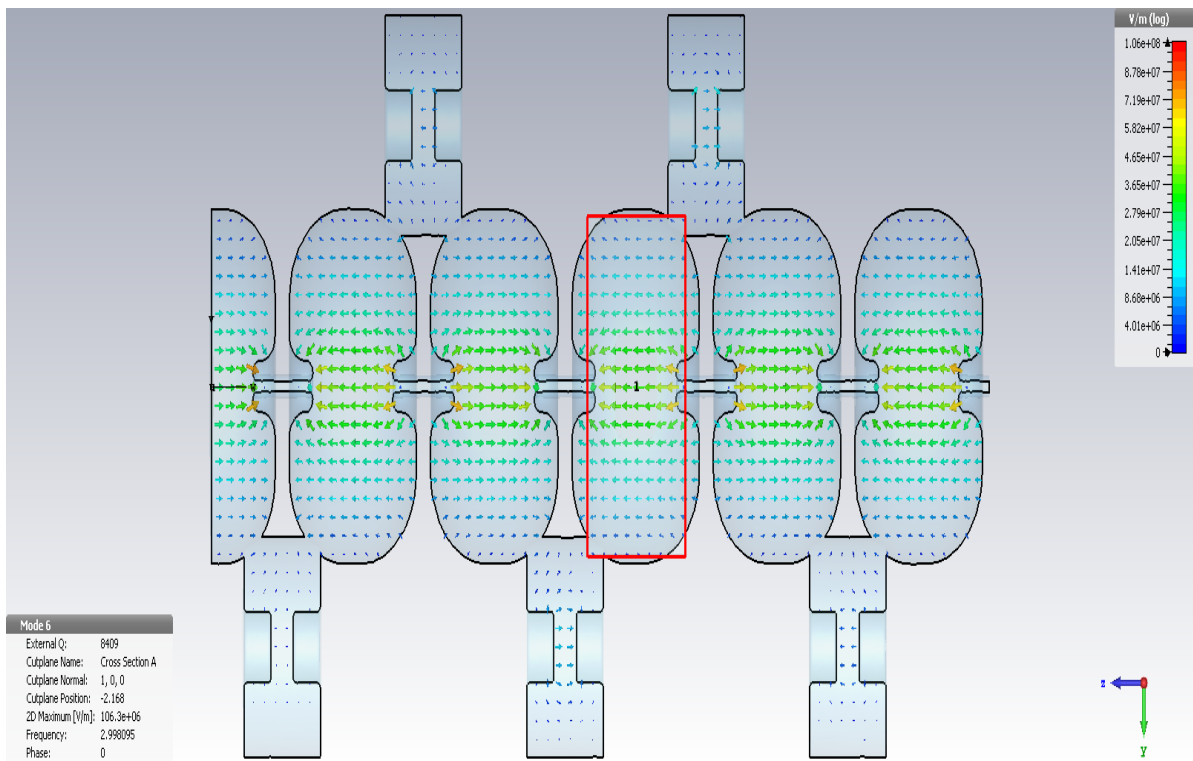
FIGURE 6.9: CST Simulation results of Electric Field profile of $\pi/2$ Mode of Side Couple standing wave cavity
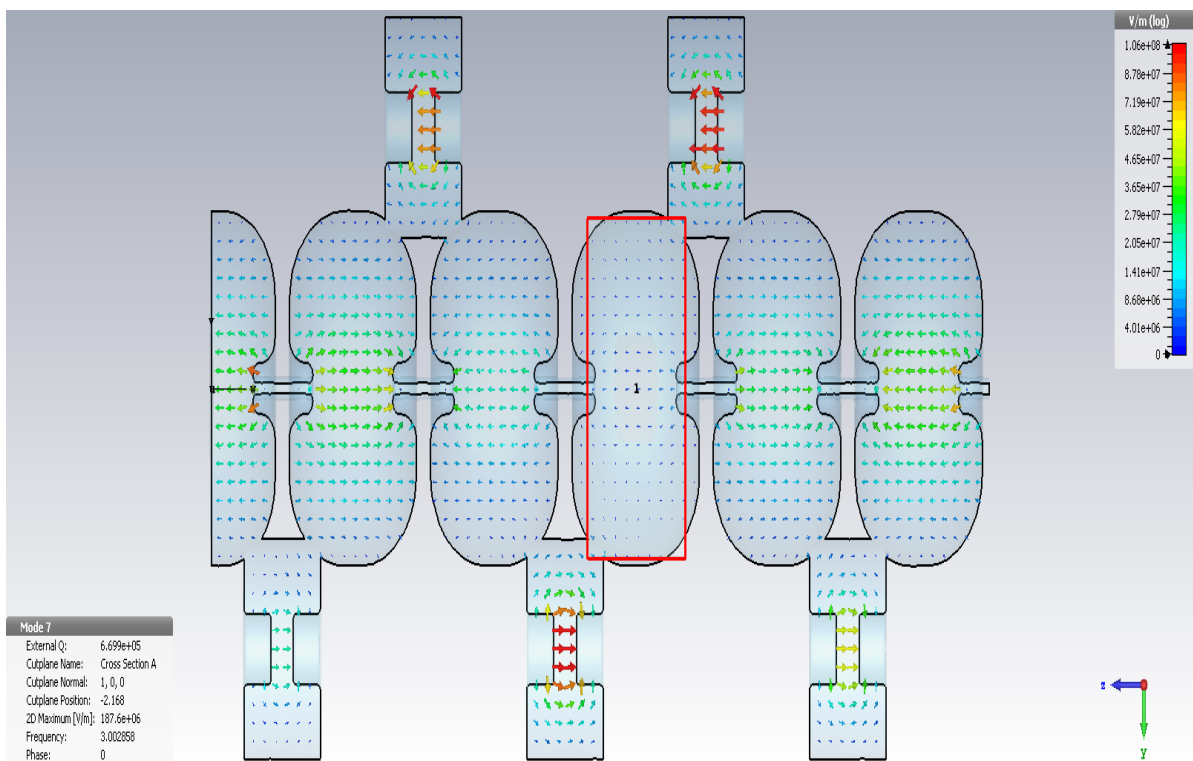
FIGURE 6.10: CST Simulation results of Electric Field profile of immediate next mode to $\pi/2$ Mode of Side Couple standing wave cavity

neighboring mode, as shown in Figure 6.12.
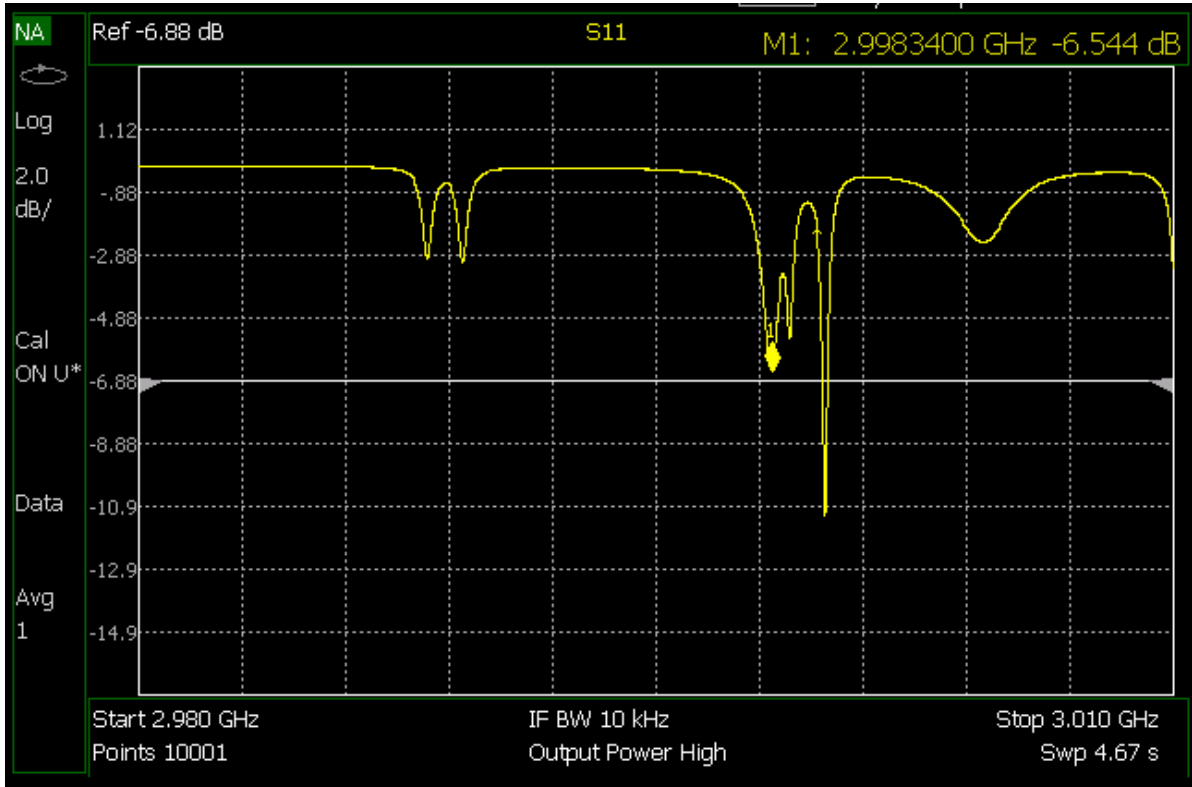
FIGURE 6.11: Vector Network Analyzer measurements of Side Coupled standing wave cavity mode spectrum highlighting $\pi/2$ and neighbouring mode.

Powering the cavity involves a microwave waveguide transmission system, which includes waveguide transitions, a four-port circulator, a directional coupler, and a water load all illustrated in Figure 6.13.

6.0.5   Results and Discussion

When we power the cavity with this conventional waveguide transmission system, we observe fluctuation in reflected signal, and after about mid of the pulse the reflected signal is increased, shown in Figure 6.14. This behavior in reflected signal indicates that the cavity's input RF power frequency is changing during the pulse and the desired mode is not excited during the whole pulse duration. The measured frequency spectrum of RF power entering the cavity is shown in Figure 6.15, which indicates that the magnetron is operating at two output frequencies, called frequency twining of magnetron. We did not have the real-time spectrum analyzer to distinguish the two RF frequencies in time during the pulse width of the magnetron. When the reflected signal was observed on the
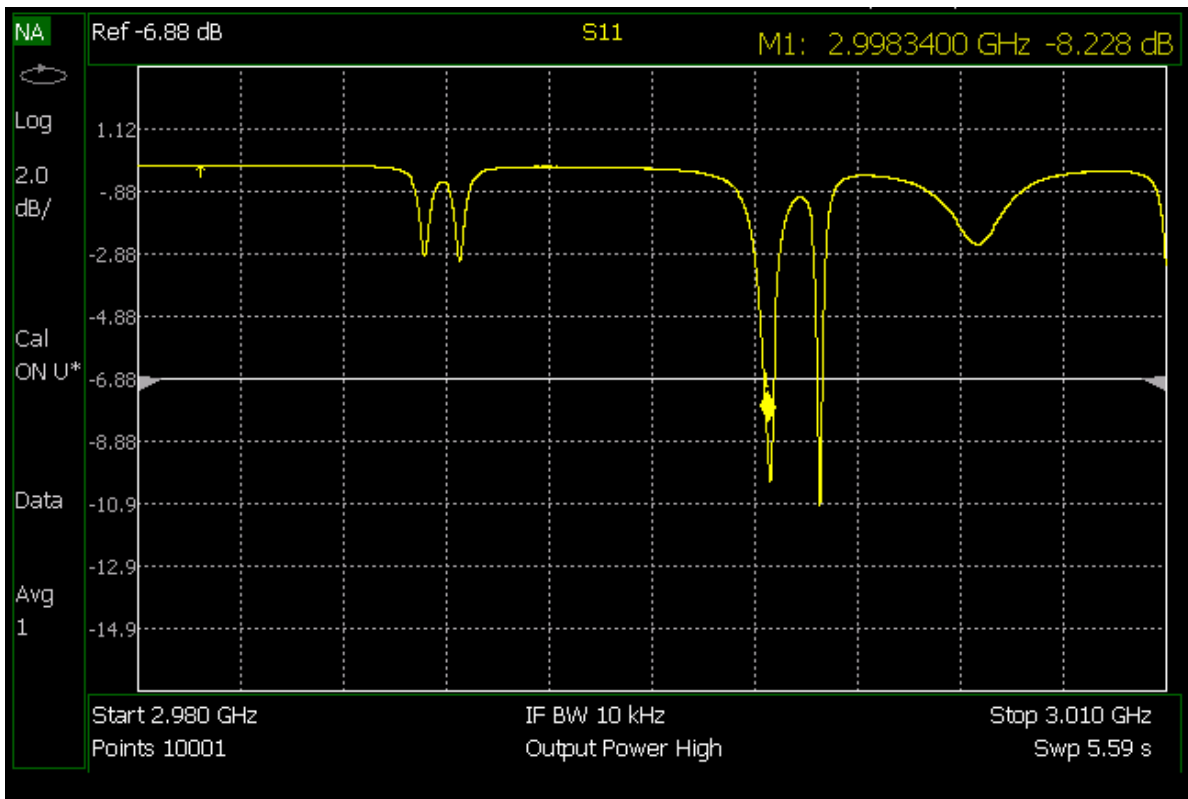
FIGURE 6.12: Vectror Network Analyzer measurements of cavity mode spectrum after placing a ceramic bead on waveguide window

scope and the AFC tuning loop was operated, the reflected signal was minimized during the first half of the microwave pulse but during the second half of the pulse reflected signal was higher in magnitude. This phenomenon indicates the mode jumping of the cavity and the increase in reflected power during the second half of the RF pulse. To solve this problem we have to stabilize the magnetron frequency during the whole RF pulse which is changing due to injection pulling.

To analyze the effect of reflected RF power from the cavity to the magnetron, we analyze the performance of the four-port circulators. The four-port circulator ensures the directional flow of RF power in this conventional microwave waveguide transmission system. The high-pulsed power magnetron is connected to port 1. Ideally, the RF power generated by the magnetron at port 1 is transmitted to port 2, while ports 3 and 4 remain uncoupled. Similarly, the power reflected from the cavity incident on port 2 is transmitted to port 3, with ports 1 and 4 remaining uncoupled. However, in practice, the four-port circulator has limited isolation between uncoupled ports.

To measure the isolation between port 1 and port 2, we used a network analyzer. Port 1 was designated as the source port, and port 2 was terminated with a perfect short to
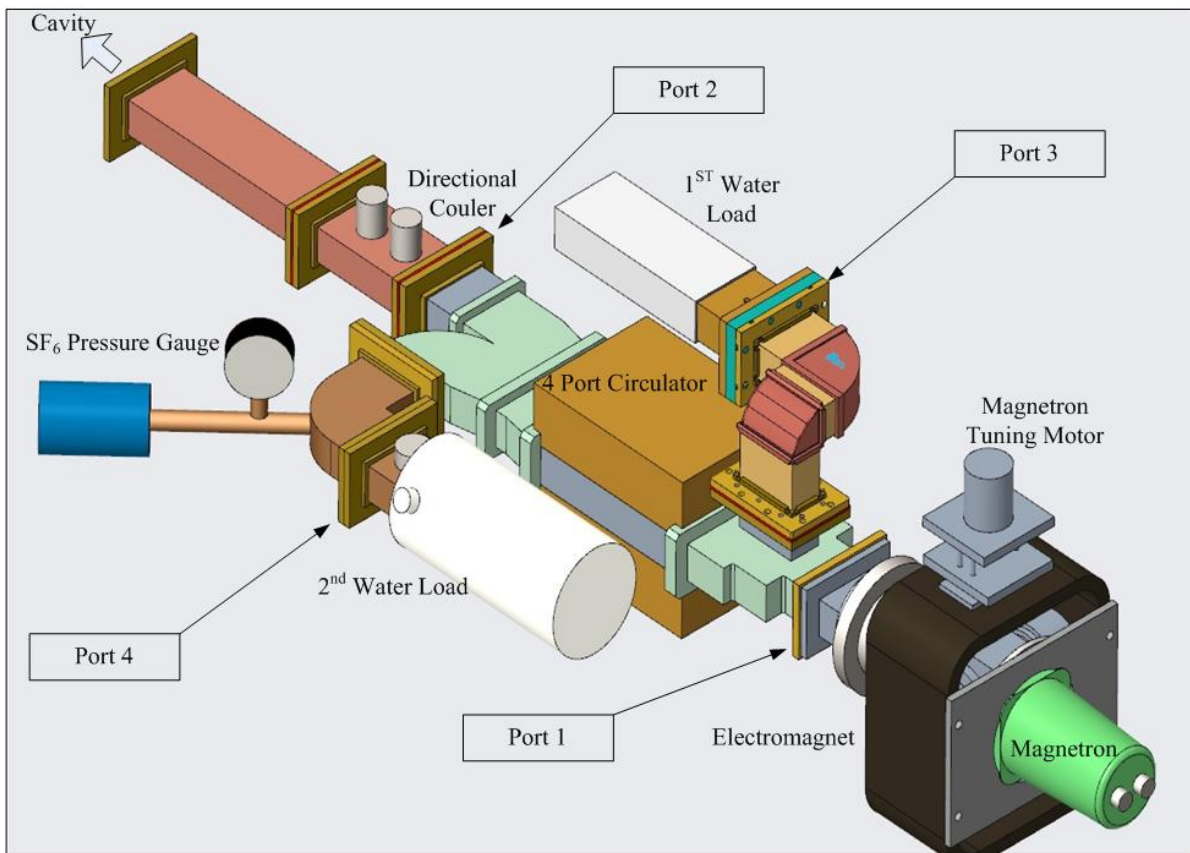
FIGURE 6.13: Experimental setup depiction of Conventional Microwave waveguide transmission system to power standing wave accelerator cavity

ensure maximum reflection. Ports 3 and 4 were connected to matched loads. With this measurement scheme, the isolation between port 1 and port 2 was found to be -29.62 dB as shown in Figure 6.16. This indicates that the microwave power reflected from the cavity connected to port 2 is attenuated by 29.62 dB before reaching back to port 1, where the high-power magnetron is connected the phase of the signal is plotted in Figure 6.17. The phase of the reflected signal at 2998MHz frequency has a definite value 0f -45.66 deg and significantly varies as the signal frequency is slightly changed. Since the actual load at port 2 would be the accelerator cavity i-e a reactive load, the phase of the reflected signal at port 1 will vary as the cavity resonance frequency is changed and also when the magnetron frequency is changed.

Similarly the isolation between port4 and port1 was measured by making port4 as source port, while port1 is connected to a short circuit plate and the other two ports were connected to matched loads. The reflection coefficient in this configuration has an amplitude and phase response shown in Figure 6.18 and Figure 6.19. This measurement shows the isolation of -17.27dB between port 4 and port 1 and the phase response has

FIGURE 6.14: Time domain Scope signal measurement of Reflected(purple) and Forward signal(green) in Magnetron twining case
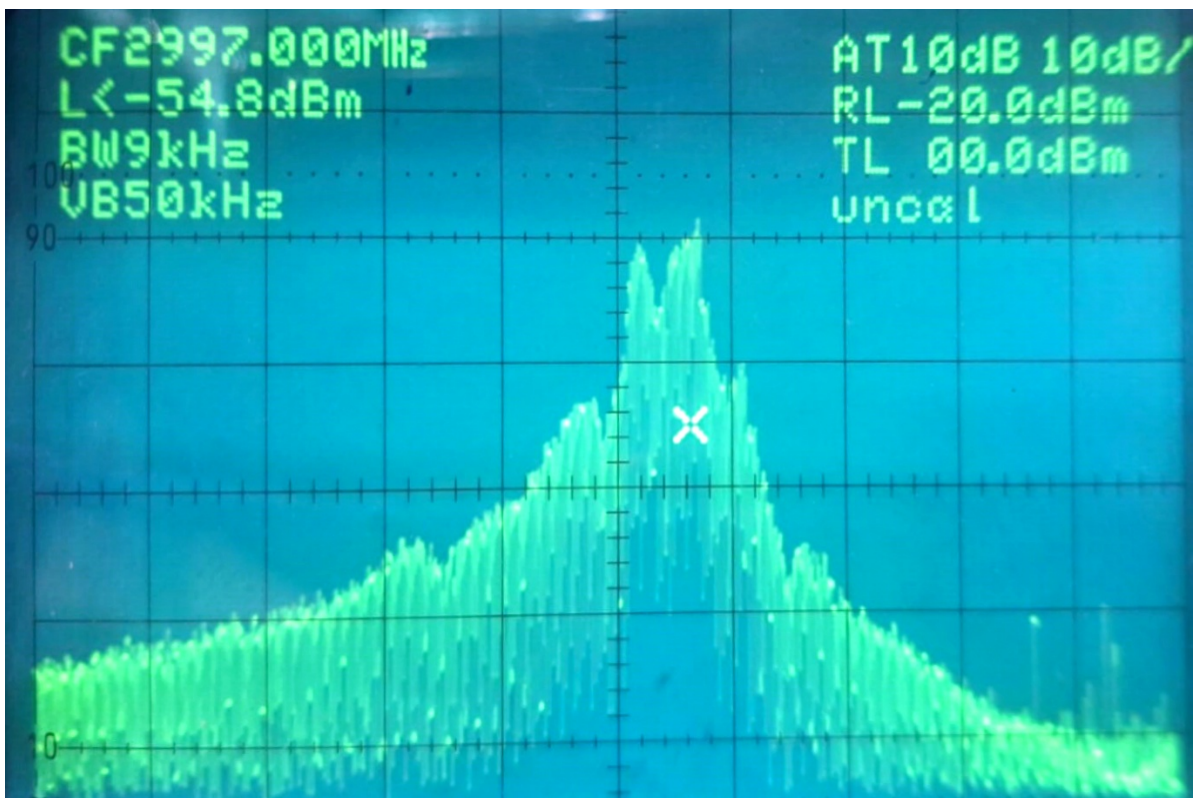
FIGURE 6.15: Frequency Spectrum of Magnetron forward power feed to 6 MeV standing wave cavity
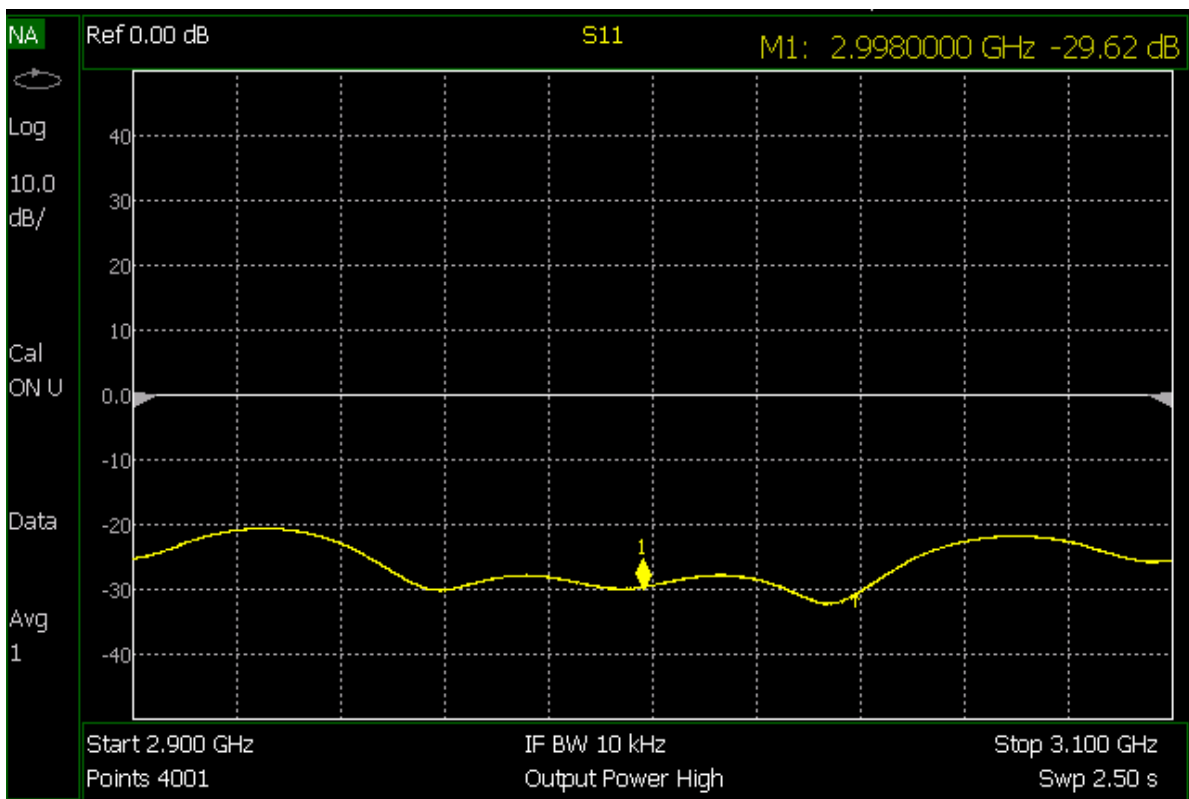
FIGURE 6.16: Four port circulator port1 and port2 isolation measurement using VNA, S11 Magnitude plot
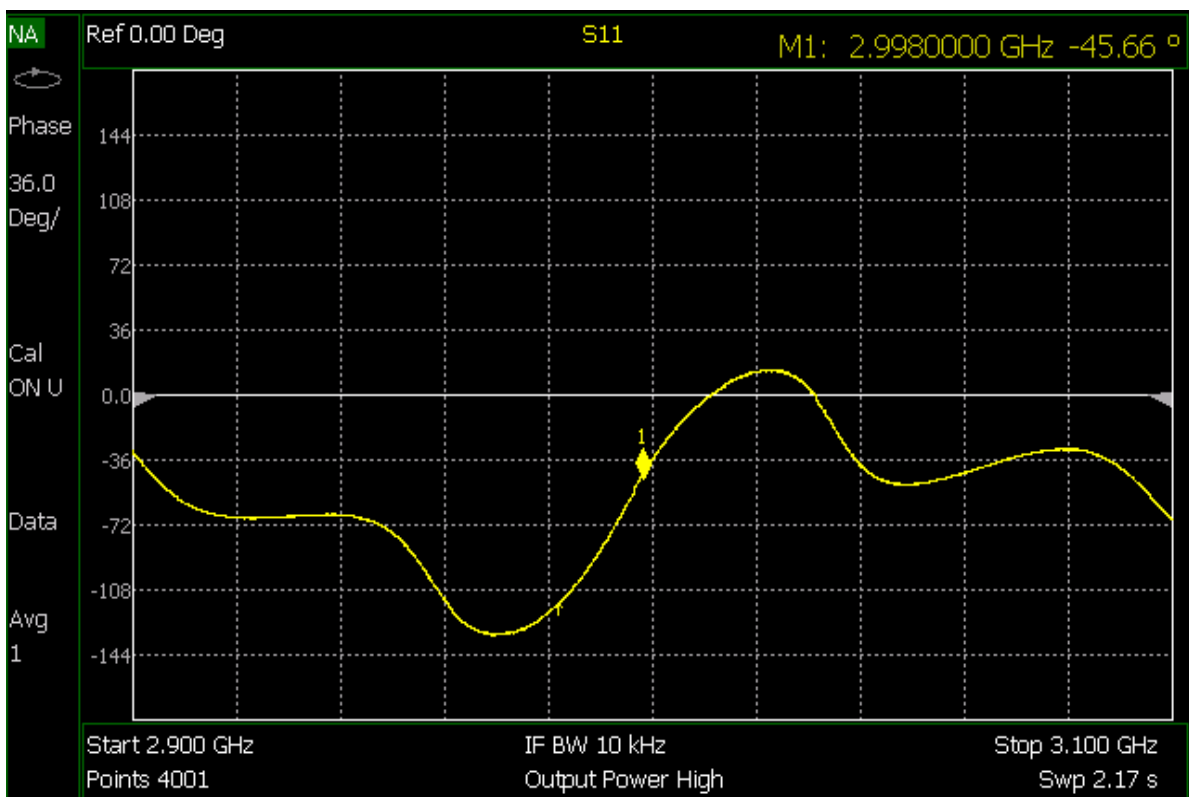
FIGURE 6.17: Four port circulator port1 and port2 isolation measurement using VNA, S11 Phase plot
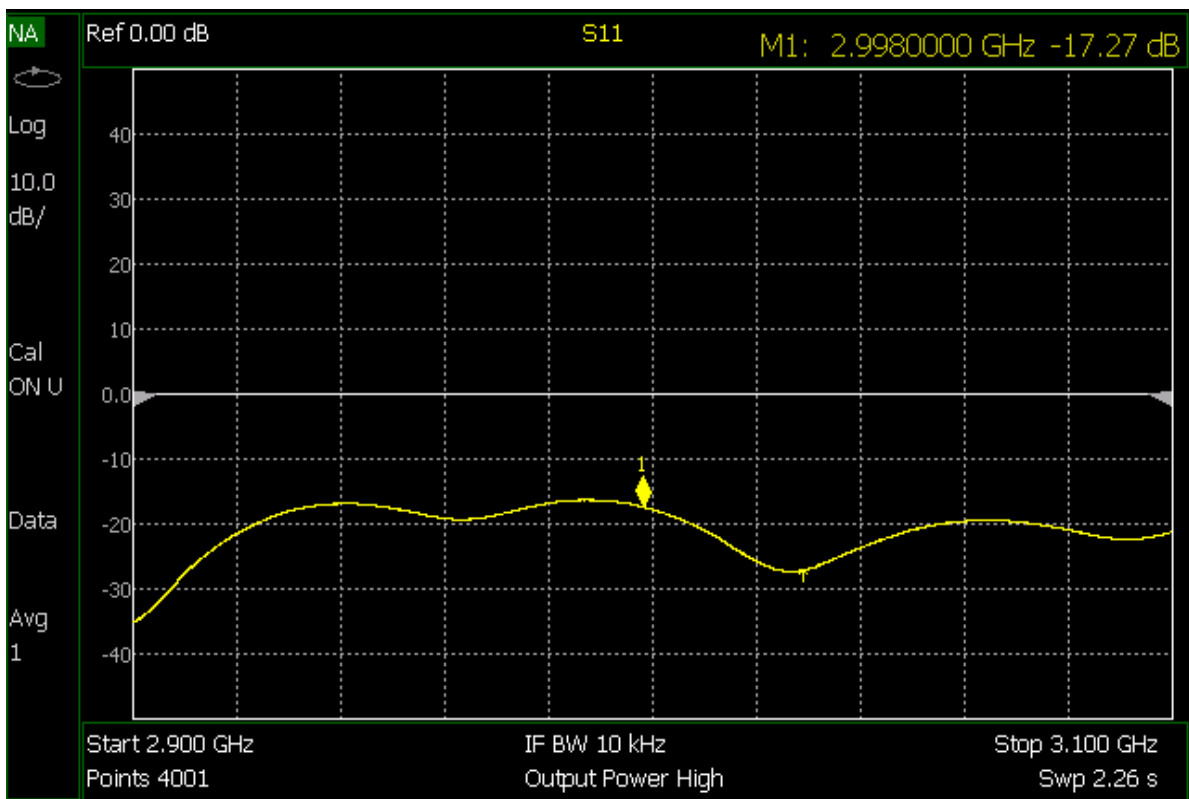
FIGURE 6.18: Four port circulator port4 and port1 isolation measurement using VNA, S11 Magnitude plot
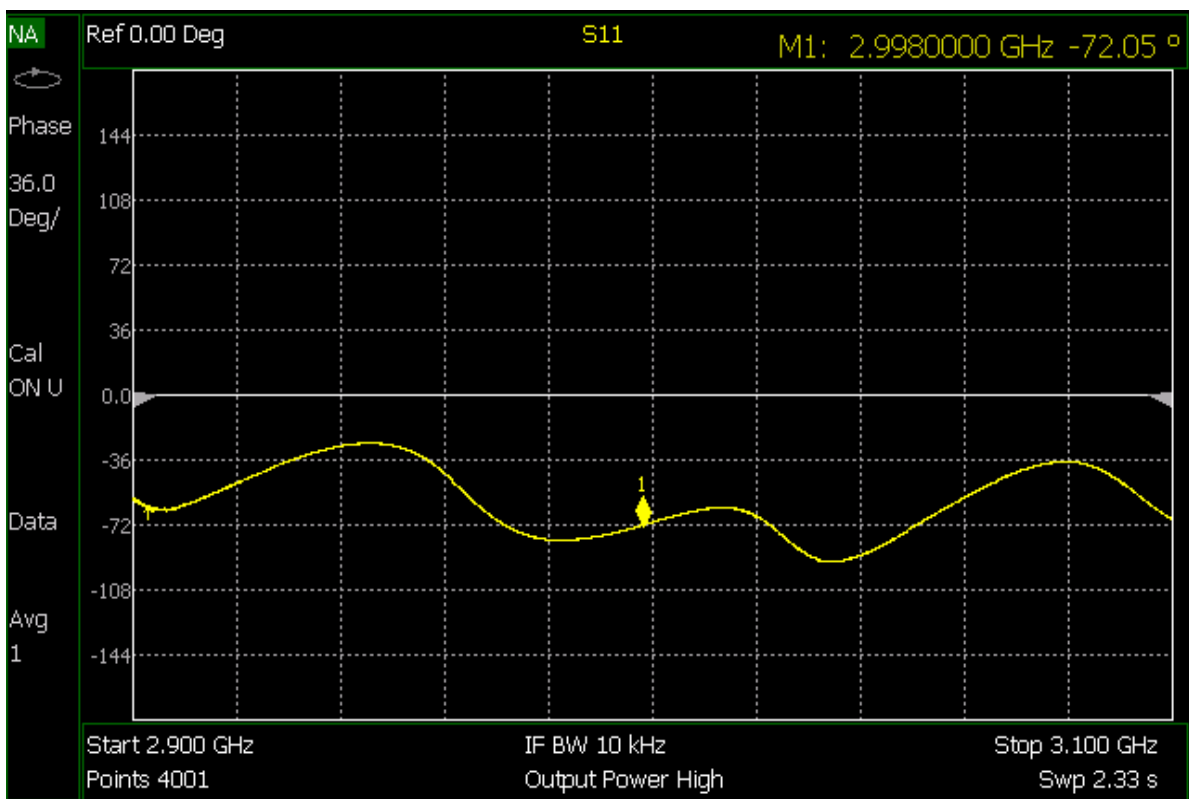
FIGURE 6.19: Four port circulator port4 and port1 isolation measurement using VNA, S11 Phase plot
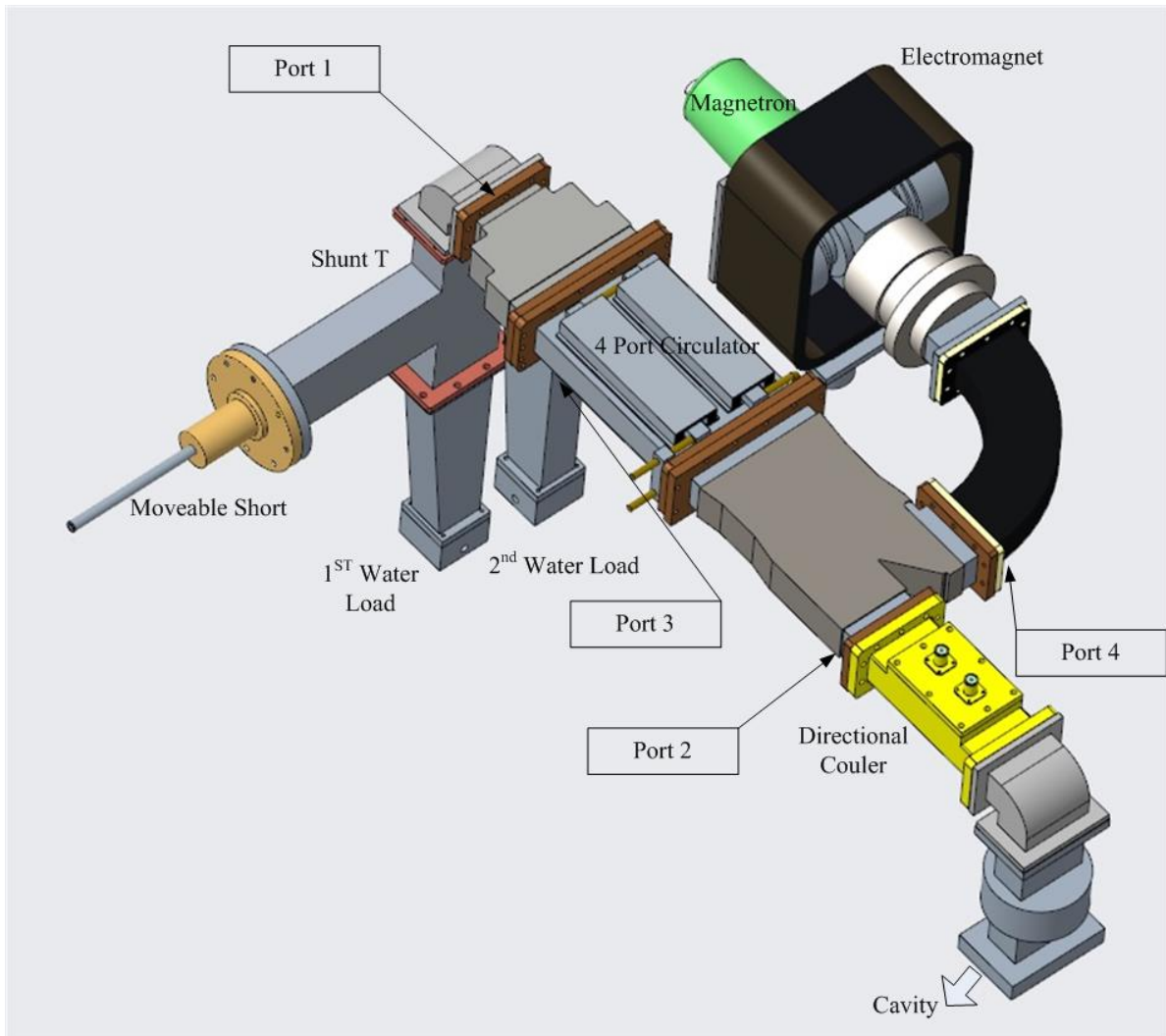
FIGURE 6.20: Modified Microwave waveguide Transmission system to power a standing wave cavity, Magnetron is connected at Circulator's port4 and shunt-T at port1.

slight variation as the frequency is slightly varied around the cavity resonance frequency of 2998MHZ.

To stabilize the magnetron frequency we need a controlled or stable signal injection to the magnetron. We modified the RF transmission system by connecting a magnetron at port 4 and a shunt T at port 1. The shunt T main arm is connected with a water load and the side arm with the movable short. The accelerating cavity is connected at port 2 and the water load at port 3. By moving the movable short in the shunt T, the amount of RF power reflected to port 1 can be controlled. the power reflected to Port 1 will be transmitted to the RF cavity at Port 2. Some of the RF power that is reflected to Port 1 from shunt T will be transmitted back to the magnetron connected at Port 4, due to limited isolation between Port 1 and Port 4 of the four Port circulators. We conducted simulations of the shunt-T using CST Microwave Studio, varying the position of the
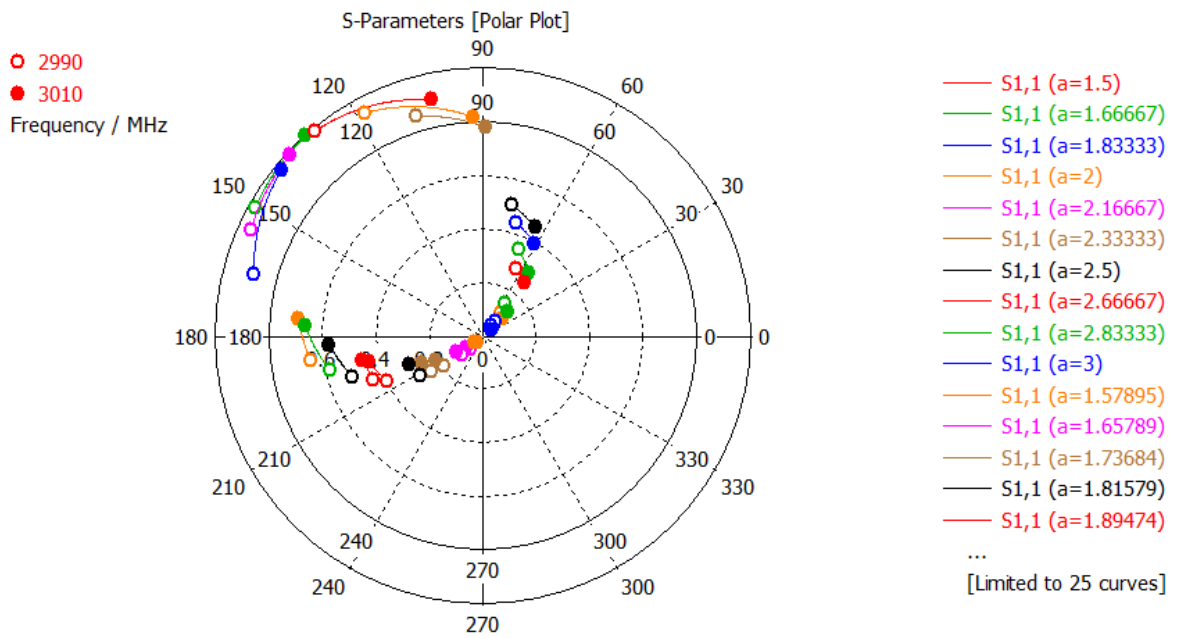
FIGURE 6.21: CST simulation results for Reflection coefficient of an S-band Shunt-T for different short circuit plate positions.

FIGURE 6.22: Frequency Spectrum of Magnetron forward Power after Injection Pulling/ Locking

FIGURE 6.23: Forward(green) and reflected signal(purple) from the directional coupler for minimum reflection

movable short plate, and recorded the reflection coefficients, as shown in Figure 6.21. The frequency sweep for the simulation was set from 2990 to 3002MHz, aligning with the frequency range of MG5193 magnetron. The obtained reflection coefficient polar plot results provide insight into the range of power levels that can be fed back to port 1 of the circulator and also the phase variation with different short circuit late positions at different frequencies can be seen by the polar chart of simulation results. In this proposed scheme the RF power is injected back into the magnetron and its phase is stable and depends on the short circuit plate position and is not varied abruptly due to the mode spectrum of the cavity. When we power the cavity with this microwave power transmission scheme the magnetron frequency twining is avoided as shown in the frequency spectrum measured, shown in Figure 6.22. Also the desired stable reflected power signal, usually called rabbit ear signal is achieved, as shown in Figure 6.23. By this magnetron self-injection locking scheme the problem of efficient RF power coupling to an RF cavity with very close mode spacing and a stable accelerating field for stable X-ray dose for radiotherapy is achieved.

6.1 Summary

In this chapter, the operation and frequency control of the high-pulsed power magnetron are discussed in detail. The primary focus of the research lies in the automatic frequency control loop of the magnetron and the utilization of self-injection locking for efficient power coupling to the accelerator cavity. Due to the unavailability of a superconducting cavity, we experimentally demonstrated the efficient power coupling of a high pulsed power tunable S-band magnetron with side side-coupled normal conducting cavity, by self-injection locking. The cavity had unusually small mode spacing between the desired accelerating mode and the immediate neighboring mode, due to imperfections in cavity fabrication. The magnetron frequency twining is avoided and power is coupled in the desired accelerating mode.

In the following chapter, the conclusion of the research conducted in this dissertation will be presented, along with potential areas for future exploration

Chapter 7

Conclusion and Future Work

This chapter presents research contributions, summarizes the research presented in the dissertation and outlines potential areas for future exploration.

7.1 Research Contributions

The major contributions of the thesis have been divided into three parts.

1. We investigated disturbance observer-based control and learning-based disturbance observer controller for maintaining cavity field stability, in the presence of cavity detuning and beam loading. The subsequent article was published during this research endeavor.

   - **Waqas Ahmed Toor**, Muhammad Ashraf, "Performance Analysis of Learning-based Disturbance Observer for Pulsed Superconducting Cavity Field Control," *Electronics*, vol. 12, Issue 7, 1556, March 2023.

2. In our lab, we had a pulse-tunable magnetron and a side-coupled normal conducting cavity for a low-energy medical linear accelerator (linac). Due to the unavailability of a superconducting cavity, we investigated the frequency control problem of magnetron using the existing cavity, which had small mode spacing due to imperfections in cavity fabrication. By employing self injection locking

through an unconventional approach to power the cavity, we improved frequency stability. This enhancement prevented magnetron frequency twinning.

3. In this thesis cavity model simulator is developed for control algorithms performance analysis and cavity field internal dynamics are simulated for a better understanding of the field control problem. This work aims to support further academic research in settings where particle accelerator setups are unavailable.

7.2   Summary

In this dissertation we discussed the modeling and simulation of particle accelerator cavities, presented the internal field dynamics of multicell cavities and their relation to the cavity model, presented simulation results of the electromechanical model of the cavity, using modal analysis estimated the detuning with dominant mechanical resonance frequencies. presented disturbance observer-based control and learning-based disturbance observer performance analysis for cavity field control. We addressed the magnetron frequency control problem in detail, discussed frequency control of magnetron and frequency twining solution through self-injection locking of the magnetron. We discussed RF power transmission scheme to cavities having small mode spacing between accelerating and neighboring mode. We Simulated and presented the results of iterative learning feed forward control for cavity field stability.

7.3   Future Work

Moving forward, our focus will be on implementing the cavity simulator on FPGA and conducting a comprehensive performance analysis of control algorithms. The future research will delve into examining the impact of measurement noise alongside other disturbances like power supply fluctuations and microphonics. Moreover, it will explore the integration of higher-order adaptive disturbance observer filters to address these challenges. This future endeavor aims to enhance the efficiency and effectiveness of cavity simulations while refining control strategies for improved particle accelerator performance. Furthermore in learning based disturbance observer critical analysis of

recursive coefficient would be explored in detail for further improvement in disturbance estimation.

The conventional method for estimating Lorentz force-induced detuning in cavity simulators involves using the mechanical modal frequencies of the structure and the square of the accelerating voltage. This allows for the calculation of detuning for each mechanical mode individually, with the total detuning being the sum of all individual detunings. However, this approach overlooks the internal field dynamics of multicell cavities. Simulations of multicell cavity fields indicate that an alternative method, which accounts for the internal field dynamics, would provide more accurate detuning estimates. With advancements in computational technologies, a comprehensive database of detuning values for various deformed or reshaped cavity structures, computed from their on-axis accelerating voltages, can contribute to better estimation of cavity detuning compared to the conventional approach. Cavity internal field dynamics linked with the cavity electromechanical model for the cavity simulator will be explored in detail, which will depend on a set of electromagnetic simulations of many possible variations in structure dimensions and orientation.

For frequency and phase stabilization, injection locking of magnetron with external solid state amplifier having narrow band frequency spectrum, will be explored. This would improve the performance of accelerators powered by magnetrons.

Bibliography

[1] T. P. Wangler, *RF Linear Accelerators*, 2nd ed. New York, NY: John Wiley & Sons, pp.2-3, 2008.

[2] E. F. Haussecker and A. W. Chao, "The influence of accelerator science on physics research," *Physics in Perspective*, vol. 13, pp. 146–160, 2011.

[3] A. Grinberg, "History of the invention and development of accelerators (1922-1932)," *Soviet Physics Uspekhi*, vol. 18, no. 10, p. 815, 1975.

[4] P. G. Kruger and G. Green, "The construction and operation of a cyclotron to produce one million volt deuterons," *Physical Review*, vol. 51, no. 9, p. 699, 1937.

[5] E. D. Courant, M. S. Livingston, and H. S. Snyder, "The strong-focusing synchroton, a new high energy accelerator," *Physical Review*, vol. 88, no. 5, p. 1190, 1952.

[6] C. W. Miller, "An 8-mev linear accelerator for x-ray therapy," *Proceedings of the IEE-Part I: General*, vol. 101, no. 130, pp. 207–221, 1954.

[7] K. Orrman-Rossiter, "Observation and annihilation: The discovery of the antiproton," *Physics in Perspective*, vol. 23, no. 1, pp. 3–24, 2021.

[8] L. W. Jones, "High energy physics in cosmic rays," in *AIP Conference Proceedings*, vol. 1516, no. 1. American Institute of Physics, 2013, pp. 17–22.

[9] W. S. Gilbert, K. B. Shaw, and R. D. Fortune, "1966 cern–lrl–rhel shielding experiment at the cern proton synchrotron." California Univ., Berkeley. Lawrence Radiation Lab.);(Rutherford High Energy ... , Tech. Rep., 1968.

[10] G. Plass, "The cern proton synchrotron: 50 years of reliable operation and continued development," *The European Physical Journal H*, vol. 36, no. 4, pp. 439–454, 2012.

[11] C. Benvenuti, "A new pumping approach for the large electron positron collider (lep)," *Nuclear Instruments and Methods in Physics Research*, vol. 205, no. 3, pp. 391–401, 1983.

[12] L. M. Lederman, "The tevatron," *Scientific American*, vol. 264, no. 3, pp. 48–55, 1991.

[13] S. Myers, "The large hadron collider 2008–2013," *International Journal of Modern Physics A*, vol. 28, no. 25, p. 1330035, 2013.

[14] S. Möller, *Accelerator technology: applications in science, medicine, and industry*. Springer Nature, 2020.

[15] A. Lechner, "Cern: Particle interactions with matter," *CERN Yellow Rep. School Proc.*, vol. 5, p. 47, 2018.

[16] W. A. Reed, "Nondestructive testing and inspection using electron linacs," in *Industrial accelerators and their applications*. World Scientific, 2012, pp. 307–369.

[17] C. Tang, "Low energy accelerators for cargo inspection," *Reviews of Accelerator Science and Technology*, vol. 8, pp. 143–163, 2015.

[18] J. Knaster and Y. Okumura, "Accelerators for fusion materials testing," *Reviews of Accelerator Science and Technology*, vol. 8, pp. 115–142, 2015.

[19] I. Altmann, K. Rehlich, S. Simrock, and T. Schilcher, "Design of the digital rf control system for the tesla test facility," in *5th European Particle Accelerator Conference, Sitges, Barcelona, Spain*, 1996.

[20] Y.-M. Wang, A. Regan, S.-I. Kwon, and C. Ziomek, "Digital llrf control system design and implementation for apt superconducting cavities," in *Proceedings of the 1999 Particle Accelerator Conference (Cat. No. 99CH36366)*, vol. 2. IEEE, 1999, pp. 1070–1072.

[21] H. Padamsee, T. Hays, and J. Knobloch, *RF superconductivity for accelerators*, ser. Wiley series in beam physics and accelerator technology. New York, NY: Wiley, 1998. [Online]. Available: https://cds.cern.ch/record/366783

[22] F. Qiu, S. Michizono, T. Miura, T. Matsumoto, M. Omet, and B. W. Sigit, "Application of disturbance observer-based control in low-level radio-frequency system in a compact energy recovery linac at kek," *Physical Review Special Topics-Accelerators and Beams*, vol. 18, no. 9, p. 092801, 2015.

[23] T. Kandil, H. Khalil, J. Vincent, T. Grimm, W. Hartung, J. Popielarski, R. York, and S. Seshagiri, "Adaptive feedforward cancellation of sinusoidal disturbances in superconducting rf cavities," *Nuclear Instruments and Methods in Physics Research Section A: Accelerators, Spectrometers, Detectors and Associated Equipment*, vol. 550, no. 3, pp. 514–520, 2005.

[24] S. Pfeiffer, "Field control challenges for different linac types," in *Proceedings of 10th International Particle Accelerator Conference (IPAC2019), Melbourne, Australia*, 2019.

[25] F. Qiu, T. Miura, D. Arakawa, N. Higashi, Y. Honda, E. Kako, T. Matsumoto, S. Michizono, T. Miyajima, T. Obina *et al.*, "Application of disturbance observer-based control on pulsed superconducting radio frequency cavities," *Physical Review Accelerators and Beams*, vol. 24, no. 1, p. 012804, 2021.

[26] D. Li, Q. Wang, P. Zhang, Z. Mi, X. Zhang, and H. Lin, "Active microphonics noise suppression based on dob control in 166.6-mhz superconducting cavities for heps," *Radiation Detection Technology and Methods*, vol. 5, no. 1, pp. 153–160, 2021.

[27] Z. Geng, "Rf control optimization and automation for normal conducting linear accelerators," *IEEE Transactions on Nuclear Science*, vol. 64, no. 8, pp. 2361–2368, 2017.

[28] F. Qiu, S. Michizono, T. Matsumoto, and T. Miura, "Combined disturbance-observer-based control and iterative learning control design for pulsed superconducting radio frequency cavities," *Nuclear Science and Techniques*, vol. 32, no. 6, pp. 1–12, 2021.

[29] Z. Geng, "Superconducting cavity control and model identification based on active disturbance rejection control," *IEEE Transactions on Nuclear Science*, vol. 64, no. 3, pp. 951–958, 2017.

[30] B. Bielawski, P. Baudrenghien, and R. Borner, "Recent developments in llrf and its controls at cern linac4," *arXiv preprint arXiv:1909.12541*, 2019.

[31] P. Baudrenghien, J. Galindo, G. Hagmann, J. Noirjean, D. Stellfeld, D. Valuch *et al.*, "Commissioning of the linac4 low level rf and future plans," *Linac14, Geneva, Switzerland*, 2014.

[32] M. Laverty, K. Fong *et al.*, "An iterative learning feedforward controller for the triumf e-linac," in *28th Linear Accelerator Conf.(LINAC'16), East Lansing, MI, USA, 25-30 September 2016.* JACOW, Geneva, Switzerland, 2017, pp. 485–487.

[33] Z. Shahriari, G. A. Dumont, and K. Fong, "Iterative learning control for beam loading cancellation in electron linear accelerator," *IFAC-PapersOnLine*, vol. 54, no. 21, pp. 55–60, 2021.

[34] R. Leewe, Z. Shahriari, K. Fong, and M. Moallem, "Resonance frequency tuning of an rf cavity through sliding mode extremum seeking," *Nuclear Instruments and Methods in Physics Research Section A: Accelerators, Spectrometers, Detectors and Associated Equipment*, vol. 902, pp. 70–75, 2018.

[35] C. Xu, J. Ma, G. Huang, and Z. Wang, "Simulation analysis of llrf feedforward compensation to beam loading for ciads linac," in *Proceedings of the 10th International Particle accelerator Conference (IPAC2019), Melbourne, Australia*, 2019, pp. 19–24.

[36] Z. Lin, C. Tang, G. Huang, Y. Du, Y. Xu, J. Yang, C. Song, W. Huang, and H. Feng, "A high voltage feedforward subsystem of low level rf system for the high power rf system," in *9th International Particle Accelerator Conference IPAC2018*, 2018. [Online]. Available: https://api.semanticscholar.org/CorpusID:69363506

[37] H. Padamsee, "Rf superconductivity–2004," *Proceedings of SRF'04*, 2004.

[38] M. I. Tahir, "Frequency and phase locking of a cw magnetron: With a digital phase locked loop using pushing characteristics," Ph.D. dissertation, Lancaster University (United Kingdom), 2008.

[39] A. Dexter, G. Burt, R. Carter, I. Tahir, H. Wang, K. Davis, and R. Rimmer, "First demonstration and performance of an injection locked continuous wave magnetron to phase control a superconducting cavity," *Physical Review Special Topics—Accelerators and Beams*, vol. 14, no. 3, p. 032001, 2011.

[40] G. Kazakevich, V. Lebedev, V. Yakovlev, and V. Pavlov, "An efficient magnetron transmitter for superconducting accelerators," *Nuclear Instruments and Methods in Physics Research Section A: Accelerators, Spectrometers, Detectors and Associated Equipment*, vol. 839, pp. 43–51, 2016.

[41] Z. Zhang, Y. Zhou, S. Lai, G. Wang, H. Zhu, and Y. Yang, "Influence of power supply ripple on injection locking of magnetron with frequency pushing effect," *Processes*, vol. 10, no. 10, p. 2124, 2022.

[42] G. Kazakevich, R. Johnson, V. Lebedev, V. Yakovlev, and V. Pavlov, "Resonant interaction of the electron beam with a synchronous wave in controlled magnetrons for high-current superconducting accelerators," *Physical Review Accelerators and Beams*, vol. 21, no. 6, p. 062001, 2018.

[43] G. Kazakevich, R. Johnson, T. Khabiboulline, V. Lebedev, G. Romanov, and V. Yakovlev, "A novel technique for pulsed operation of magnetrons without modulation of cathode voltage," Fermi National Accelerator Lab.(FNAL), Batavia, IL (United States), Tech. Rep., 2020.

[44] G. M. Kazakevich, V. M. Pavlov, Y. U. Jeong, and B. C. Lee, "Intrapulse frequency stability of a magnetron frequency-locked through a wave reflected from an accelerating cavity," *Nuclear Instruments and Methods in Physics Research Section A: Accelerators, Spectrometers, Detectors and Associated Equipment*, vol. 647, no. 1, pp. 10–16, 2011.

[45] P. Pengvanich, V. Neculaes, Y. Lau, R. M. Gilgenbach, M. Jones, W. White, and R. Kowalczyk, "Modeling and experimental studies of magnetron injection locking," *Journal of applied physics*, vol. 98, no. 11, 2005.

[46] W.-J. Ye, Y. Zhang, P. Yuan, H.-C. Zhu, K.-M. Huang, and Y. Yang, "Modeling and experimental studies of a side band power re-injection locked magnetron," *Chinese Physics B*, vol. 25, no. 12, p. 128402, 2016.

[47] S. Yue, Z.-C. Zhang, and D.-P. Gao, "Analysis of the injection-locked magnetron with a mismatched circulator," *Chinese Physics B*, vol. 23, no. 8, p. 088402, 2014.

[48] T. Mitani, N. Shinohara, and H. Matsumoto, "Development of a pulse-driven phase-controlled magnetron," in *2007 IEEE International Vacuum Electronics Conference*. IEEE, 2007, pp. 1–2.

[49] J. J. Choi and G. W. Choi, "Experimental observation of frequency locking and noise reduction in a self-injection-locked magnetron," *IEEE transactions on electron devices*, vol. 54, no. 12, pp. 3430–3432, 2007.

[50] G. W. Choi, H. J. Kim, H. J. Kim, and J. J. Choi, "The self-injection-locked magnetron," in *2008 IEEE International Vacuum Electronics Conference*. IEEE, 2008, pp. 445–446.

[51] Y. Bliokh, Y. E. Krasik, and J. Felsteiner, "Self-injection-locked magnetron as an active ring resonator side coupled to a waveguide with a delayed feedback loop," *IEEE Transactions on Plasma Science*, vol. 40, no. 1, pp. 78–82, 2011.

[52] G. Kazakevich, R. Johnson, G. Flanagan, F. Marhauser, V. Yakovlev, B. Chase, V. Lebedev, S. Nagaitsev, R. Pasquinelli, N. Solyak *et al.*, "High-power magnetron transmitter as an rf source for superconducting linear accelerators," *Nuclear Instruments and Methods in Physics Research Section A: Accelerators, Spectrometers, Detectors and Associated Equipment*, vol. 760, pp. 19–27, 2014.

[53] M. Zheng, X. Lyu, X. Liang, and F. Zhang, "A generalized design method for learning-based disturbance observer," *IEEE/ASME Transactions on Mechatronics*, vol. 26, no. 1, pp. 45–54, 2020.

[54] S. Matsievskiy, R. Alekhanov, A. Bulanov, V. Kaminskiy, E. Savin, N. Sobenin *et al.*, "Hybrid electron linac with standing and travelling wave accelerating sections," in *7th Int. Particle Accelerator Conf.(IPAC'16), Busan, Korea, May 8-13, 2016*. JACOW, Geneva, Switzerland, 2016, pp. 1791–1793.

[55] R. Corsini, F. Tecker, D. Schulte, A. Ghigo, P. Skowronski, D. Alesini, and C. Biscari, "Fast vertical beam instability in the ctf3 combiner ring," CERN, Tech. Rep., 2008.

[56] Accessed on 29-11-2024. [Online]. Available: https://altairusa.com

[57] L. Arnaudon, C. Bertone, L. Hammouti, L. Lopez-Hernandez, M. Paoluzzi, J. Coupard, S. Mathot, K. Hanke, C. Rossi, C. Noels *et al.*, "The linac4 project at cern," CERN, Tech. Rep., 2011.

[58] F. Gerigk, N. Alharbi, M. Pasini, S. Ramberger, M. Vretenar, and R. Wegner, "Rf structures for linac4," in *2007 IEEE Particle Accelerator Conference (PAC)*, 2007, pp. 3821–3823.

[59] M. Awida, M. Foley, I. Gonin, A. Grassellino, C. Grimm, T. Khabiboulline, A. Lunin, A. Rowe, and V. Yakovlev, "Development of 5-cell beta= 0.9 650 mhz cavities for project x," *Proceedings of LINAC2014, Geneva, Switzerland.*

[60] S. Simrock and Z. Geng, *Low-Level Radio Frequency Systems.* Springer Nature, 2022.

[61] M. Rathore, V. K. Jain, A. Atulkar, K. K. Singh, and R. Porwal, "Study of lorentz force detuning and its compensation in superconducting radiofrequency cavity: A review," *Materials Today: Proceedings*, vol. 44, pp. 1369–1374, 2021.

[62] Z. Geng and S. Simrock, "Sources of field perturbations," *4th Linear Collider school,Huairou, Beijing, China*, 2009.

[63] S. Simrock and Z. Geng, "Cavity field control," *8th International school on Linear Collider*, 2013.

[64] A. Mandal, S. Som, S. Saha, S. Paul, S. Seth, R. Bhandari, P. Raj, B. Mandal, B. Das, U. Panda *et al.*, "Closed loop rf tuning for superconducitng cyclotron at vecc," in *being presented in this conference Cyclotrons-2010, IMP, China*, 2010.

[65] S. Andres, "Beam cavity interaction," *Proceedings of SRF'21*, June 2021.

[66] T. Schilcher, "Vector sum control of pulsed accelerating fields in lorentz force detuned superconducting cavities," DESY Hamburg, Germany, Tech. Rep., 1998.

[67] J. R. Delayen, *Phase and amplitude stabilization of superconducting resonators.* California Institute of Technology, 1978.

[68] J. Dai, J. Zhang, H. Huang, H. Lin, Y. Sun, P. Sha, Q. Wang, and H. Li, "Llrf and data acquisition systems for spoke012 cavity vertical test at ihep," *Proceedings of SRF2013, Paris, France*, 2013.

[69] A. Aksoy, Ö. Karslı, Ç. Kaya, E. Kazancı, Ö. Yavaş, S. Ozkorucuklu, and P. Arıkan, "Design parameters and current status of the tarla project," *TH-PRO026, IPAC*, vol. 14, 2014.

[70] R. Laxdal, K. Fong, A. Grassellino, A. Mitra, I. Sekachev, V. Zvyagintsev *et al.*, "The 1.3 ghz superconducting rf program at triumf," in *this conference*, 2008.

[71] M. Pekeler, "Test results on the 9-cell 1.3 ghz superconducting rf cavities for the tesla test facility linac," in *Proceedings of the 1997 Particle Accelerator Conference (Cat. No. 97CH36167)*, vol. 3. IEEE, 1997, pp. 2917–2919.

[72] J. Iversen, R. Bandelmann, G. Kreps, W. Moeller, D. Proch, J. Sekutowicz, W. Singer *et al.*, "A review of the 1.3 ghz superconducting 9-cell cavity fabrication for desy," in *Proceedings of LINAC Conference, Tsukuba*, 2010.

[73] F. Qiu, S. Michizono, T. Miura, T. Matsumoto, N. Liu, and S. B. Wibowo, "Real-time cavity simulator-based low-level radio-frequency test bench and applications for accelerators," *Physical Review Accelerators and Beams*, vol. 21, no. 3, p. 032003, 2018.

[74] N. Solyak, M. Awida, I. Gonin, T. Khabiboulline, Y. Pischalnikov, W. Schappert, V. Yakovlev *et al.*, "Simulations of mechanical resonances in srf cavities in low beam current cw operation," in *Proceedings of the 16th international conference on RF superconductivity, Paris, France*, 2013, pp. 23–27.

[75] T. Czarski, R. S. Romaniuk, K. T. Pozniak, and S. Simrock, "Cavity control system advanced modeling and simulations for tesla linear accelerator and free electron laser," in *Photonics Applications in Astronomy, Communications, Industry, and High-Energy Physics Experiments II*, vol. 5484. SPIE, 2004, pp. 69–87.

[76] A. Dexter, "Magnetrons for accelerators," *IEEE Trans. MTT*, vol. 13, 1965.

[77] "Radio-oncology service essentials, linac systems basic course," SIEMENSE AG Healthcare Sector, Erlangen, Germany, Tech. Rep., Feb 2014.

[78] Accessed on 29-11-2024. [Online]. Available: https://en.wikipedia.org/wiki/Klystron

[79] G. Schaffer, "Components for high-power rf systems in modern accelerators," in *New Techniques for Future Accelerators II: RF and Microwave Systems.* Springer, 1989, pp. 267–308.

[80] A. V. Haeff, "An ultra-high-frequency power amplifier of novel design," *Electronics*, vol. 12, no. 2, pp. 30–32, 1939.

[81] D. H. Preist and M. B. Shrader, "The klystrode—an unusual transmitting tube with potential for uhf-tv," *Proceedings of the IEEE*, vol. 70, no. 11, pp. 1318–1325, 1982.

[82] M. Kaushik and L. Joshi, "Inductive output tube (iot)–a review," *Journal of Electromagnetic Waves and Applications*, vol. 29, no. 15, pp. 2027–2037, 2015.

[83] D. McGinnis and M. Lindroos, "The european spallation source," in *2013 IEEE 14th International Vacuum Electronics Conference (IVEC).* IEEE, 2013, pp. 1–2.

[84] C. Beard, "Review of available power sources," *Nuclear Instruments and Methods in Physics Research Section A: Accelerators, Spectrometers, Detectors and Associated Equipment*, vol. 557, no. 1, pp. 276–279, 2006.

[85] A. Zolfghari, P. MacGibbon, and B. North, "Comparison of klystron and inductive output tubes (iot) vacuum-electron devices for rf amplifier service in free-electron laser," in *Proceedings of EPAC*, 2004, pp. 1093–1095.

[86] L. Hoang, "High power radio frequency solid-state amplifiers and combiners for particle accelerators: From module to system design approach," Ph.D. dissertation, Acta Universitatis Upsaliensis, 2019.

[87] S.-J. Park, S. Cha, J. Hwang, D. Kim, Y. J. Park, D. Yu *et al.*, "Beam loss suppression by beam matching in klystron," in *10th Int. Particle Accelerator Conf.(IPAC'19), Melbourne, Australia, 19-24 May 2019.* JACOW Publishing, Geneva, Switzerland, 2019, pp. 4218–4220.

[88] A. Smirnov, R. Agustsson, M. Ahmadi, P. Blanchard, S. Boucher, R. Branner, J. Hartzell, K. Hoyt, V. Khodos, and D. Mccann, "Progress on 1.5 ghz multi-kw cw amplifier," in *Proceedings of the 9th International Particle Accelerator Conference (IPAC'18), Vancouver, BC, Canada*, vol. 29, 2004.

[89] M. Boland *et al.*, *Updated baseline for a staged Compact Linear Collider.* CERN Publishing, 2016.

[90] A. Y. Baikov, C. Marrelli, and I. Syratchev, "Toward high-power klystrons with rf power conversion efficiency on the order of 90%," *IEEE Transactions on Electron devices*, vol. 62, no. 10, pp. 3406–3412, 2015.

[91] T. Habermann, A. Balkcum, R. Begum, H. Bohlen, M. Cattelino, E. Eisen, D. Gajaria, A. Staprans, B. Stockwell, and L. Zitelli, "High-power high-efficiency l-band multiple-beam klystron development at cpi," *IEEE transactions on plasma science*, vol. 38, no. 6, pp. 1264–1269, 2010.

[92] D. Sprehn, A. Haase, A. Jensen, E. N. Jongewaard, C. D. Nantista, and A. Vlieks, "A 12 ghz 50 MW klystron for support of accelerator research," *SLAC, Stanford, CA, USA, Rep. SLAC-PUB-14377*, 2010.

[93] E. Jensen and I. Syratchev, "CLIC 50 MW l-band multi-beam klystron," in *AIP Conference Proceedings*, vol. 807, no. 1. American Institute of Physics, 2006, pp. 90–99.

[94] P. Marchand, T. Ruan, F. Ribeiro, and R. Lopes, "High power 352 mhz solid state amplifiers developed at the synchrotron soleil," *Physical Review Special Topics-Accelerators and Beams*, vol. 10, no. 11, p. 112001, 2007.

[95] S. Li, J. Yang, W.-H. Chen, and X. Chen, *Disturbance observer-based control: methods and applications.* CRC press, 2014.

[96] E. Rogers, B. Chu, C. Freeman, and P. Lewin, *Iterative learning control algorithms and experimental benchmarking.* John Wiley & Sons, 2023.

[97] Z. Bien and J.-X. Xu, *Iterative learning control: analysis, design, integration and applications.* Springer Science & Business Media, 2012.

[98] Y. Chen and C. Wen, *Iterative learning control: convergence, robustness and applications.* Springer, 1999.

[99] F. Qiu, S. Michizono, T. Matsumoto, T. Miura, S. B. Wibowo, and N. Liu, "Development of iterative learning and disturbance observer-based llrf control system for international linear collider," in *Proceedings of the 14th Annual Meeting of Particle Accelerator Society of Japan*, 2017, pp. 490–2.

[100] G. B. Collins, "Microwave magnetrons," *(No Title)*, 1948.

[101] K. Fukumoto, M. Nakajima, and J.-l. Ikenoue, "Mathematical representation of microwave oscillator characteristics by use of the rieke diagram," *IEEE transactions on microwave theory and techniques*, vol. 31, no. 11, pp. 954–959, 1983.

[102] A. Gilmour Jr, *Microwave and millimeter-wave vacuum electron devices: inductive output tubes, klystrons, traveling-wave tubes, magnetrons, crossed-field amplifiers, and gyrotrons.* New York, NY: Artech House, 2020.

[103] C. Karzmark and N. C. Pering, "Electron linear accelerators for radiation therapy: history, principles and contemporary developments," *Physics in Medicine & Biology*, vol. 18, no. 3, p. 321, 1973.